8-2007

Nonlinear Control Strategies for Advanced Vehicle Thermal Management Systems

Mohammad Salah
Clemson University, msalah@clemson.edu

NONLINEAR CONTROL STRATEGIES FOR ADVANCED VEHICLE THERMAL
MANAGEMENT SYSTEMS

A Dissertation
Presented to
the Graduate School of
Clemson University

In Partial Fulfillment
of the Requirements for the Degree
Doctor of Philosophy
Electrical and Computer Engineering

---

by
Mohammad Hasan Salah
August 2007

Accepted by:
Dr. Darren Dawson, Committee Chair
John Wagner
Ian Walker
Timothy Burg

ABSTRACT

Advanced thermal management systems for internal combustion engines can improve coolant temperature regulation and servo–motor power consumption to positively impact the tailpipe emissions, fuel economy, and parasitic losses by better regulating the combustion process with multiple computer controlled components. The traditional thermostat valve, coolant pump, and clutch–driven radiator fan are upgraded with servo–motor actuators. When the system components function harmoniously, desired thermal conditions can be accomplished in a power efficient manner. Although the vehicle's mechanical loads can be driven by electric servo–motors, the power demands often require large actuator sizes and electrical currents. Integrating hydraulically–driven actuators in the cooling circuit offers higher torques in a smaller package space. Hydraulics are widely applied in transportation and manufacturing systems due to their high power density, design flexibility for power transmission, and ease of computer control.

In this dissertation, several comprehensive nonlinear control architectures are proposed for transient temperature tracking in automotive cooling circuits. First, a single loop experimental cooling system has been fabricated and assembled which features a variable position smart valve, variable speed electric coolant pump, variable speed electric radiator fan, engine block, radiator, steam–based heat exchanger, and various sensors. Second, a multiple loop experimental cooling system has been assembled which features a variable position smart thermostat valve, two variable speed electric pumps, variable speed electric radiator fan, engine block, transmission, radiator, steam–based

heat exchanger, and sensors. Third, a single loop experimental hydraulic–based thermal system has been assembled which features a variable speed hydraulic coolant pump and radiator fan, radiator, and immersion heaters. In the first and second configured systems, the steam–based heat exchanger emulates the engine's combustion process and transmission heat. For the third test platform, immersion heating coils emulate the combustion heat.

For the first configured system, representative numerical and experimental results are discussed to demonstrate the thermal management system operation in precisely tracking desired temperature profiles and minimizing electrical power consumption. The experimental results show that less than 0.2°K temperature tracking error can be achieved with a 14% improvement in the system component power consumption. In the second configured system, representative experimental results are discussed to investigate the functionality of the multi–loop thermal management system under normal and elevated ambient temperatures. The presented results clearly show that the proposed robust controller–based thermal management system can accurately track prescribed engine and transmission temperature profiles within 0.13°K and 0.65°K, respectively, and minimize electrical power consumption by 92% when compared to the traditional factory control method. Finally, representative numerical and experimental results are discussed to demonstrate the performance of the hydraulic actuators–based advance thermal management system in tracking prescribed temperature profiles (*e.g.*, 42% improvement in the temperature tracking error) and minimizing satisfactorily hydraulic power consumption when compared to other common control method.

DEDICATION

This Dissertation is dedicated to my wife, Fida, for her love and sacrifice.

ACKNOWLEDGMENTS

TABLE OF CONTENTS

LIST OF TABLES

LIST OF FIGURES

List of Figures (Continued)

a solenoid contact length [mm]

A_f frontal area of the fan [m^2]

A_p area of thermostat valve plate [m^2]

A_{sr} secondary radiator frontal area [m^2]

b coolant pump inlet impeller width [m]

b_f radiator fan motor damping coefficient [N.m.s/rad]

b_p coolant pump motor damping coefficient [N.m.s/rad]

b_v thermostat valve motor damping coefficient [N.m.s/rad]

b_{val} hydraulic valve damping coefficient [N.s/cm]

B_m hydraulic motor damping coefficient [N.m.s/rad]

B_{mf} hydraulic fan motor damping coefficient [N.m.s/rad]

B_{mp} hydraulic pump motor damping coefficient [N.m.s/rad]

c coulomb friction [N]

c_a real positive constant

c_c real positive constant

c_{pa} air specific heat [kJ/kg.ºK]

c_{pc} coolant specific heat [kJ/kg.ºK]

c_{po} oil specific heat [kJ/kg.ºK]

C_a charge–air–cooler air–side thermal capacity [kJ/°K]

C_c charge–air–cooler coolant–side thermal capacity [kJ/°K]

C_d hydraulic motor damping coefficient

C_{df} hydraulic fan motor damping coefficient

C_{dp} hydraulic pump motor damping coefficient

C_e engine block thermal capacity [kJ/°K]

C_{im} internal hydraulic motor leakage coefficient [cm^5/N.s]

C_{imf} internal hydraulic fan motor leakage coefficient [cm^5/N.s]

C_{imp} internal hydraulic pump motor leakage coefficient [cm^5/N.s]

C_r radiator thermal capacity [kJ/°K]

C_{sr} secondary radiator thermal capacity [kJ/°K]

C_t transmission thermal capacity [kJ/°K]

d gear pitch [mm]

D_m hydraulic motor displacement [m^3/rev]

D_{mf} hydraulic fan motor displacement [m^3/rev]

D_{mp} hydraulic pump motor displacement [m^3/rev]

e engine temperature tracking error [°K]

e_o initial engine temperature tracking error [°K]

e_{ss} engine temperature steady state error [°K]

F_s force generated by the solenoid coil [N]

F_{ss} steady state fluid force on the solenoid [N]

F_{ss1} steady state force due to fluid exiting the main valve chamber to port A [N]

F_{ss2} steady state force due to fluid exiting port B to tank [N]

F_{tr} transient fluid force on the solenoid [N]

F_{tr1} transient force due to fluid acceleration between loads A and B [N]

F_{tr2} transient force due to fluid acceleration to the right of land B [N]

h hydraulic valve piston translational displacement [m]

h_{sr} secondary radiator forced heat transfer coefficient [kW/m^2.°K]

H normalized valve position [%]

$\overline{H}$ normalized valve position for $\overline{m}$ [%]

H_o minimum normalized valve position [%]

i servo solenoid control valve coil current [A]

i_{af} radiator fan motor armature current [A]

i_{ap} coolant pump motor armature current [A]

i_{av} thermostat valve motor armature current [A]

J hydraulic motor and load inertia [kg.m^2]

J_f radiator fan motor inertia [kg.m^2]

J_p coolant pump motor inertia [kg.m^2]

J_v thermostat valve motor inertia [kg.m^2]

k_e	real positive control gain
k_f	real positive control gain
k_p	real positive control gain
k_r	real positive control gain
k_t	real positive control gain
k_{val}	hydraulic valve spring constant [N/m]
K_{bf}	radiator fan motor back EMF constant [V.s/rad]
K_{bp}	coolant pump motor back EMF constant [V.s/rad]
K_{bv}	thermostat valve motor back EMF constant [V.s/rad]
K_{mf}	radiator fan motor torque constant [N.m/A]
K_{mp}	coolant pump motor torque constant [N.m/A]
K_{mv}	thermostat valve motor torque constant [N.m/A]
l_g	solenoid valve reluctance gap [mm]
L	control valve coil internal inductance [H]
L_{af}	radiator fan inductance [H]
L_{ap}	coolant pump motor inductance [H]
L_{av}	thermostat valve motor inductance [H]
L_d	damping length [mm]
m_s	hydraulic valve spool mass [g]

$\bar{m}$ radiator coolant mass flow rate control input [kg/s]

$\dot{m}_a$ air mass flow rate through the charge–air–cooler air–side [kg/s]

$\dot{m}_{ar}$ air mass flow rate through the radiator fan [kg/s]

$\dot{m}_{asr}$ air mass flow rate through the secondary radiator [kg/s]

$\dot{m}_c$ pump coolant mass flow rate [kg/s]

$\dot{m}_{ce}$ coolant mass flow rate through the engine pump [kg/s]

$\dot{m}_{cr}$ coolant mass flow rate through the radiator [kg/s]

$\dot{m}_{csr}$ coolant mass flow rate through the secondary radiator [kg/s]

$\dot{m}_f$ air mass flow rate through the radiator fan [kg/s]

m_o minimum coolant mass flow rate through the radiator [kg/s]

$\dot{m}_{ot}$ oil mass flow rate through the transmission pump [kg/s]

$\dot{m}_r$ coolant mass flow rate through the radiator [kg/s]

N worm to thermostat valve motor gear ratio

N_t number of turns in solenoid coil

P_A hydraulic motor supply pressure [psi]

P_B hydraulic motor return pressure [psi]

P_L hydraulic motor load pressure [psi]

P_{Lp} hydraulic pump motor load pressure [psi]

P_{Lf} hydraulic fan motor load pressure [psi]

P_S supply pressure [psi]

P_{Sp} hydraulic pump motor supply pressure [psi]

P_{Sf} hydraulic fan motor supply pressure [psi]

P_{sys} cooling system average power consumption [W]

P_T tank pressure [psi]

ΔP pressure drop across the thermostat valve [Pa]

Q_a radiator heat lost due to uncontrollable air flow [kW]

Q_e combustion process heat energy [kW]

Q_{in} combustion process heat energy [kW]

Q_L hydraulic motor load flow [LPM]

Q_{Lf} hydraulic fan motor load flow [LPM]

Q_{Lp} hydraulic pump motor load flow [LPM]

Q_o radiator heat lost due to uncontrollable air flow [kW]

Q_{rf} secondary radiator heat loss due to primary radiator fan [kW]

Q_{sr} secondary radiator heat loss due to ram air flow and primary radiator fan [kW]

Q_t transmission heat energy [kW]

r coolant pump inlet to impeller blade length [m]

R control valve coil internal resistance [Ω]

R_{af} radiator fan motor resistor [Ω]

R_{ap} coolant pump motor resistor [Ω]

R_{av} thermostat valve motor resistor [Ω]

R_f nonlinear fluid/air resistance [Ω]

sgn   standard signum function

t current time [s]

t_o initial time [s]

T_{ai} air temperature at the charge–air–cooler intlet [ºK]

T_{ao} air temperature at the charge–air–cooler outlet [ºK]

T_{ci} coolant temperature at charge–air–cooler intlet [ºK]

T_{co} coolant temperature at the charge–air–cooler outlet [ºK]

T_e coolant temperature at the engine outlet [ºK]

T_{ed} desired engine coolant temperature trajectory [ºK]

T_g hydraulic motor generated torque [N.m]

T_H liquid wax temperature [ºK]

T_L wax softening temperature [ºK]

T_{Lf} hydraulic fan motor load torque [N.m]

T_{Load} hydraulic motor load torque [N.m]

T_{Lp} hydraulic pump motor load torque [N.m]

T_r coolant temperature at the radiator outlet [ºK]

T_{re} coolant temperature at the radiator outlet [ºK]

T_{rt} oil temperature at the radiator oil outlet [ºK]

T_t oil temperature at the transmission outlet [ºK]

T_{td} desired transmission oil temperature [ºK]

T_{vr} virtual reference for the radiator temperature [ºK]

T_{vro} minimum virtual reference for the radiator temperature [ºK]

$\overline{T}_{vr}$ virtual reference control input for the radiator temperature [ºK]

T_∞ surrounding ambient temperature [ºK]

ΔT desired engine temperature boundary layer [ºK]

v inlet radial coolant velocity [m/s]

V control valve coil voltage [V]

V_{af} air volume per fan rotation [m^3/rad]

V_{ep} engine coolant pump applied voltage [V]

V_f voltage applied on the radiator fan [V]

V_o fluid volume per radian of pump motor shaft rotation [m^3/rad]

V_p voltage applied on the pump [V]

V_{pt} transmission oil pump applied voltage [V]

V_{ram} ram air velocity [km/h]

V_{rf} radiator fan applied voltage [V]

V_t volum of compressed fluid [cm^3]

V_{tf} volum of compressed fluid in the hydraulic radiator fan [cm^3]

V_{tp} volum of compressed fluid in the hydraulic coolant pump [cm^3]

V_v voltage applied on the thermostat valve [V]

w orifice area gradient [cm^2/cm]

w_f hydraulic fan orifice area gradient [cm^2/cm]

w_p hydraulic pump orifice area gradient [cm^2/cm]

x control valve spool displacement [mm]

x_{mf} hydraulic fan valve maximum spool displacement [mm]

x_{mp} hydraulic pump valve maximum spool displacement [mm]

x_f hydraulic fan control valve spool displacement [mm]

x_p hydraulic fan control valve spool displacement [mm]

X_f hydraulic fan control valve spool displacement ratio [%]

X_p hydraulic pump control valve spool displacement ratio [%]

α_e real positive control gain

α_t real positive control gain

β bulk modulus of hydraulic fluid [MPa]

β_f bulk modulus of coolant pump hydraulic fluid [MPa]

β_{im} inlet impeller angel [rad]

β_p	bulk modulus of the radiator fan hydraulic fluid [MPa]
β_r	positive constant [rad/sec.m^2]
ε	radiator effectiveness [%]
ε_{cac}	charge–air–cooler effectiveness [%]
ε_r	radiator effectiveness [%]
η	radiator temperature tracking error [ºK]
η_e	engine coolant temperature error [ºK]
η_{eo}	initial engine coolant temperature error [ºK]
η_{ess}	engine coolant temperature steady–state error [ºK]
η_f	radiator fan speed tracking error [rad/s]
η_{fan}	radiator fan efficiency [%]
η_p	pump speed tracking error [rad/s]
η_r	radiator temperature tracking error [ºK]
η_t	transmission oil temperature error [ºK]
η_{to}	initial transmission oil temperature error [ºK]
η_{tss}	transmission oil temperature steady–state error [ºK]
θ	temperature [ºK]
θ_v	thermostat valve motor angular displacement [rad]
μ_o	solenoid armature permeability [H/mm]

ρ	fluid density [kg/m^3]
ρ_a	air density [kg/m^3]
ρ_c	coolant density [kg/m^3]
ρ_e	real positive control gain
ρ_f	hydraulic fan fluid density [kg/m^3]
ρ_p	hydraulic pump fluid density [kg/m^3]
ρ_t	real positive control gain
ω	hydraulic motor angular velocity [rad/s]
ω_f	radiator fan motor angular velocity [rad/s]
ω_{fd}	designed desired fan velocity [rad/s]
ω_p	coolant pump motor angular velocity [rad/s]
ω_{pd}	designed desired pump velocity [rad/s]
ω_{po}	minimum coolant pump velocity [rad/s]
$\bar{\omega}_p$	control input [rad/s]

CHAPTER 1
ROBUST CONTROL STRATEGY FOR ADVANCED VEHICLE THERMAL
MANAGEMTN SYSTEMS

Introduction

Internal combustion engine active thermal management systems offer enhanced coolant temperature tracking during transient and steady–state operation. Although the conventional automotive cooling system has proven satisfactory for many decades, servomotor controlled cooling components have the potential to reduce the fuel consumption, parasitic losses, and tailpipe emissions (Brace *et al.*, 2001). Advanced automotive cooling systems replace the conventional wax thermostat valve with a variable position smart valve, and replace the mechanical coolant pump and radiator fan with electric and/or hydraulic driven actuators (Choukroun and Chanfreau, 2001). This later action decouples the coolant pump and radiator fan from the engine crankshaft. Hence, the problem of having over/under cooling, due to the mechanical coupling, is solved as well as parasitic losses reduced which arose from operating mechanical components at high rotational speeds (Chalgren and Barron, 2003).

An assessment of thermal management strategies for large on–highway trucks and high–efficiency vehicles has been reported by Wambsganss (1999). Chanfreau *et al.* (2001) studied the benefits of engine cooling with fuel economy and emissions over the FTP drive cycle on a dual voltage 42V–12V minivan. Cho *et al.* (2004) investigated a controllable electric coolant pump in a class–3 medium duty diesel engine truck. It was shown that the radiator size can be reduced by replacing the mechanical pump with an electrical one. Chalgren and Allen (2005) and Chalgren and Traczyk (2005) improved the

1

temperature control, while decreasing parasitic losses, by replacing the conventional cooling system of a light duty diesel truck with an electric cooling system.

To create an efficient automotive thermal management system, the vehicle's cooling system behavior and transient response must be analyzed. Wagner *et al.* (2001, 2002, 2003) pursued a lumped parameter modeling approach and presented multi–node thermal models which estimated internal engine temperature. Eberth *et al.* (2004) created a mathematical model to analytically predict the dynamic behavior of a 4.6L spark ignition engine. To accompany the mathematical model, analytical/empirical descriptions were developed to describe the smart cooling system components. Henry *et al.* (2001) presented a simulation model of powertrain cooling systems for ground vehicles. The model was validated against test results which featured basic system components (*e.g.*, radiator, coolant pump, surge (return) tank, hoses and pipes, and engine thermal load).

A multiple node lumped parameter–based thermal network with a suite of mathematical models, describing controllable electromechanical actuators, was introduced by Setlur *et al.* (2005) to support controller studies. The proposed simplified cooling system used electrical immersion heaters to emulate the engine's combustion process and servomotor actuators, with nonlinear control algorithms, to regulate the temperature. In their experiments, the coolant pump and radiator fan were set to run at constant speeds, while the smart thermostat valve was controlled to track coolant temperature set points. Cipollone and Villante (2004) tested three cooling control schemes (*e.g.*, closed–loop, model–based, and mixed) and compared them against a traditional "thermostat–based" controller. Page *et al.* (2005) conducted experimental tests

on a medium–sized tactical vehicle that was equipped with an intelligent thermal management system. The authors investigated improvements in the engine's peak fuel consumption and thermal operating conditions. Finally, Redfield *et al.* (2006) operated a class 8 tractor at highway speeds to study potential energy saving and demonstrated engine cooling to with ±3ºC of a set point value.

In this chapter, nonlinear control strategies are presented to actively regulate the coolant temperature in internal combustion engines. An advanced thermal management system has been implemented on a laboratory test bench that featured a smart thermostat valve, variable speed electric coolant pump and fan, radiator, engine block, and a steam–based heat exchanger to emulate the combustion heating process. The proposed backstepping robust control strategy, selected to accommodate disturbances and uncertainties, has been verified by simulation techniques and validated by experimental testing. In Section 1.2, a set of mathematical models are presented to describe the automotive cooling components and thermal system dynamics. Nonlinear tracking control strategies are introduced in Section 1.3. The experimental test bench is presented in Section 1.4 and Section 1.5 introduces numerical and experimental results, while the concluded remarks are contained in Section 1.6.

Automotive Thermal Management Models

A suite of mathematical models will be presented to describe the dynamic behavior of the advanced cooling system. The system components include a 6.0L diesel engine with a steam–based heat exchanger to emulate the combustion heat, a three–way

smart valve, a variable speed electric coolant pump, and a radiator with a variable speed electric fan.

<center>Cooling System Thermal Descriptions</center>

A reduced order two–node lumped parameter thermal model (refer to Figure 1.1) describes the cooling system's transient response and minimizes the computational burden for in–vehicle implementation. The engine block and radiator behavior can be described by

$$C_e \dot{T}_e = Q_{in} - c_{pc} \dot{m}_r \left(T_e - T_r \right) \tag{1.1}$$

$$C_r \dot{T}_r = -Q_o + c_{pc} \dot{m}_r \left(T_e - T_r \right) - \varepsilon c_{pa} \dot{m}_f \left(T_e - T_\infty \right). \tag{1.2}$$

The variables $Q_{in}(t)$ and $Q_o(t)$ represent the input heat generated by the combustion process and the radiator heat loss due to uncontrollable air flow, respectively. An adjustable double pass steam–based heat exchanger delivers the emulated heat of combustion at a maximum of 55kW in a controllable and repeatable manner. In an actual vehicle, the combustion process will generate this heat which is transferred to the coolant through the block's coolant jacket.

For a three–way servo–driven thermostat valve, the radiator coolant mass flow rate, $\dot{m}_r(t)$, is based on the pump flow rate and normalized valve position as $\dot{m}_r = H\dot{m}_c$ where the variable $H(t)$ satisfies the condition $0 \le H \le 1$. Note that $H = 1(0)$ corresponds to a fully closed (open) valve position and coolant flow through the radiator (bypass) loop.

<center>4</center>
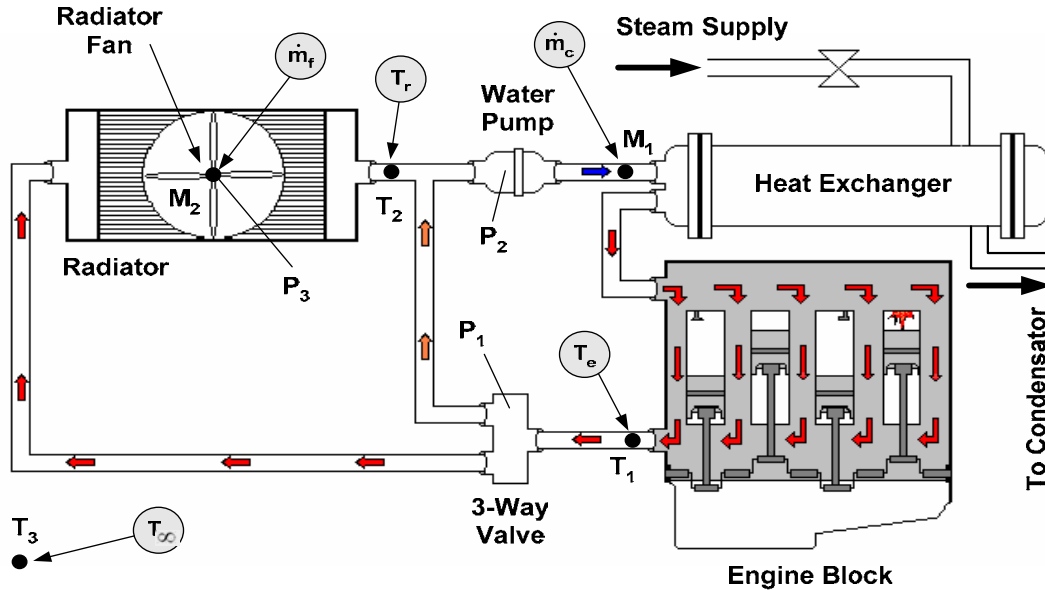
Figure 1.1 Advanced cooling system which features a smart valve, variable speed pump, variable speed fan, engine block, radiator, and sensors (temperature, mass flow rate, and power)

To facilitate the controller design process, three assumptions are imposed:

Assumption 1.1: *The signals $Q_{in}(t)$ and $Q_o(t)$ always remain positive in (1.1) and (1.2) (i.e., $Q_{in}(t), Q_o(t) \geq 0$). Further, the signals $Q_{in}(t), \dot{Q}_{in}(t), \ddot{Q}_{in}(t)$ and $Q_o(t)$ remain bounded at all time, such that $Q_{in}(t), \dot{Q}_{in}(t), \ddot{Q}_{in}(t), Q_o(t) \in L_\infty$.*

Assumption 1.2: *The surrounding ambient temperature $T_\infty(t)$ is uniform and satisfies $T_e(t) - T_\infty(t) \geq \varepsilon_1, \forall t \geq 0$ where $\varepsilon_1 \in \mathbb{R}^+$ is a constant.*

Assumption 1.3: *The engine block and radiator temperatures satisfy the condition $T_e(t) - T_r(t) \geq \varepsilon_2, \forall t \geq 0$ where $\varepsilon_2 \in \mathbb{R}^+$ is a constant. Further, $T_e(0) \geq T_r(0)$ to facilitate the boundedness of signal argument.*

This final assumption allows the engine and radiator to initially be the same temperature

(*e.g.*, cold start). The unlikely case of $T_e(0) < T_r(0)$ is not considered.

<center>Variable Position Smart Valve</center>

A dc servo–motor has been actuated in both directions to operate the multi–position smart thermostat valve. The compact motor, with integrated external potentiometer for position feedback, is attached to a worm gear assembly that is connected to the valve's piston. The governing equation for the motor's armature current, $i_{av}(t)$, can be written as

$$\frac{di_{av}}{dt} = \frac{1}{L_{av}}\left(V_v - R_{av}i_{av} - K_{bv}\frac{d\theta_v}{dt}\right). \tag{1.3}$$

The thermostat valve motor's angular acceleration, $d^2\theta_v(t)/dt^2$, may be computed as

$$\frac{d^2\theta_v}{dt^2} = \frac{1}{J_v}\left(-b_v\frac{d\theta_v}{dt} + K_{mv}i_{av} + 0.5dN.\left(A_p\Delta P + c\,\mathrm{sgn}\left(\frac{dh}{dt}\right)\right)\right). \tag{1.4}$$

Note that the motor is operated by a high gain proportional control to reduce the position error and speed up the overall piston response.

<center>Variable Speed Coolant Pump</center>

A computer controlled electric motor operates the high capacity centrifugal coolant pump. The motor's armature current, $i_{ap}(t)$, can be described as

$$\frac{di_{ap}}{dt} = \frac{1}{L_{ap}}\left(V_p - R_{ap}i_{ap} - K_{bp}\omega_p\right) \tag{1.5}$$

where the motor's angular velocity, $\omega_p(t)$, can be computed as

$$\frac{d\omega_p}{dt} = \frac{1}{J_p}\left(-\left(b_p + R_f V_o^2\right)\omega_p + K_{mp}i_{ap}\right). \tag{1.6}$$

<center>6</center>

The coolant mass flow rate for a centrifugal coolant pump depends on the coolant density, shaft speed, system geometry, and pump configuration. The mass flow rate may be computed as $\dot{m}_c = \rho_c \left(2\pi r b v \right)$ where $v = \left(r \omega_p \right) \tan \beta_{im}$. It is assumed that the coolant flow enters normal to the impeller.

<p style="text-align:center">Variable Speed Radiator Fan</p>

A cross flow heat exchanger and a dc servo–motor driven fan form the radiator assembly. The electric motor directly drives a multi–blade fan that pulls the surrounding air through the radiator assembly. The air mass flow rate going through the radiator is affected directly by the fan's rotational speed, $\omega_f(t)$, so that

$$\frac{d\omega_f}{dt} = \frac{1}{J_f} \left(-b_f \omega_f + K_{mf} i_{af} - \rho_a A_f R_f V_{af}^2 \right) \tag{1.7}$$

where $V_{af} = \left[\left(K_{mf} / \eta_{fan} \rho_a A_f \right) i_{af} \omega_f \right]^{0.3}$. The corresponding air mass flow rate is written as $\dot{m}_f = \beta_r \rho_a A_f V_{af}$. The fan motor's armature current, $i_{af}(t)$, can be described as

$$\frac{di_{af}}{dt} = \frac{1}{L_{af}} \left(V_f - R_{af} i_{af} - K_{bf} \omega_f \right). \tag{1.8}$$

Note that a voltage divider circuit has been inserted into the experimental system to measure the current drawn by the fan and estimate the power consumed.

<p style="text-align:center">Thermal System Control Design</p>

A Lyapunov–based nonlinear control algorithm will be presented to maintain a desired engine block temperature, $T_{ed}(t)$. The controller's main objective is to precisely

track engine temperature set points while compensating for system uncertainties (*i.e.*, combustion process input heat, $Q_{in}(t)$, radiator heat loss, $Q_o(t)$) by harmoniously controlling the system actuators. Although other linear and nonlinear control algorithms may be formulated, this particular control strategy demonstrated outstanding disturbance rejection qualities. Referring to Figure 1.1, the system servo–actuators are a three–way smart valve, a coolant pump, and a radiator fan. Another important objective is to reduce the electric power consumed by these actuators, $P_{sys}(t)$. The main concern is pointed towards the fact that the radiator fan consumes the most power of all cooling system components followed by the pump. It is also important to point out that in (1.1) and (1.2), the signals $T_e(t)$, $T_r(t)$ and $T_\infty(t)$ can be measured by either thermocouples or thermistors, and the system parameters c_{pc}, c_{pa}, C_e, C_r, and ε are assumed to be constant and fully known.

<u>Backstepping Robust Control Objective</u>

The control objective is to ensure that the actual temperatures of the engine, $T_e(t)$, and the radiator, $T_r(t)$, track the desired trajectories $T_{ed}(t)$ and $T_{vr}(t)$,

$$\left|T_{ed}(t) - T_e(t)\right| \le \varepsilon_e, \ \left|T_r(t) - T_{vr}(t)\right| \le \varepsilon_r \text{ as } t \to \infty \tag{1.9}$$

while compensating for the system variable uncertainties $Q_{in}(t)$ and $Q_o(t)$ where ε_e and ε_r are real positive constants.

Assumption 1.4: *The engine temperature profiles are always bounded and chosen such that their first three time derivatives remain bounded at all times (i.e., $T_{ed}(t), \dot{T}_{ed}(t), \ddot{T}_{ed}(t)$ and $\dddot{T}_{ed}(t) \in L_\infty$). Further, $T_{ed}(t) \gg T_\infty(t)$ at all times.*

Remark 1.1: *Although it is unlikely that the desired radiator temperature setpoint, $T_{vr}(t)$, is required (or known) by the automotive engineer, it will be shown that the radiator setpoint can be indirectly designed based on the engine's thermal conditions and commutation strategy (refer to Remark 1.2).*

To facilitate the controller's development and quantify the temperature tracking control objective, the tracking error signals $e(t)$ and $\eta(t)$ are defined as

$$e \triangleq T_{ed} - T_e, \quad \eta \triangleq T_r - T_{vr}. \tag{1.10}$$

By adding and subtracting $MT_{vr}(t)$ to (1.1), and expanding the variables $M = c_{pc}m_o$ and

$\dot{m}_r = m_o + \bar{m} = H_o\dot{m}_c + \bar{H}\dot{m}_c$, the engine and radiator dynamics can be rewritten as

$$C_e\dot{T}_e = Q_{in} - M\left(T_e - T_{vr}\right) - c_{pc}\bar{m}\left(T_e - T_r\right) + M\eta \tag{1.11}$$

$$C_r\dot{T}_r = -Q_o + c_{pc}\left(m_o + \bar{m}\right)\left(T_e - T_r\right) - \varepsilon\, c_{pa}\dot{m}_f\left(T_e - T_\infty\right) \tag{1.12}$$

where $\eta(t)$ was introduced in (1.10), and m_o and H_o are real positive design constants.

Closed–Loop Error System Development and Controller Formulation

The open–loop error system can be analyzed by taking the first time derivative of both expressions in (1.10) and then multiplying both sides of the resulting equations by C_e and C_r for the engine and radiator dynamics, respectively. Thus, the system dynamics described in (1.11) and (1.12) can be substituted and then reformatted to realize

$$C_e\dot{e} = C_e\dot{T}_{ed} - Q_{in} + M\left(T_e - T_{vro}\right) - u_e - M\eta \tag{1.13}$$

$$C_r\dot{\eta} = M\left(T_e - T_r\right) - Q_o + u_r - C_r\dot{T}_{vr}. \tag{1.14}$$

In these expressions, (1.10) was utilized as well as $T_{vr} \triangleq T_{vro} + \bar{T}_{vr}$,

$u_e = M\bar{T}_{vr} - c_{pc}\bar{m}(T_e - T_r)$, and $u_r = c_{pc}\bar{m}(T_e - T_r) - \varepsilon c_{pa}\dot{m}_f(T_e - T_\infty)$. The parameter

T_{vro} is a real positive design constant.

Remark 1.2: *The control inputs $\bar{m}(t)$, $\bar{T}_{vr}(t)$ and $\dot{m}_f(t)$ are uni–polar. Hence, commutation strategies are designed to implement the bi–polar inputs $u_e(t)$ and $u_r(t)$ as*

$$\bar{m} \triangleq \frac{u_e\left[\operatorname{sgn}(u_e) - 1\right]}{2c_{pc}(T_e - T_r)}, \qquad \bar{T}_{vr} \triangleq \frac{u_e\left[1 + \operatorname{sgn}(u_e)\right]}{2M}, \qquad \dot{m}_f \triangleq \frac{F\left[1 + \operatorname{sgn}(F)\right]}{2\varepsilon c_{pa}(T_e - T_\infty)} \qquad (1.15)$$

where $F \triangleq c_{pc}\bar{m}(T_e - T_r) - u_r$. The control input, $\dot{m}_f(t)$ is obtained from (1.15) after $\bar{m}(t)$ is computed. From these definitions, it is clear that if $u_e(t), u_r(t) \in L_\infty \forall t \geq 0$, then $\bar{m}(t), \bar{T}_{vr}(t), \dot{m}_f(t) \in L_\infty \forall t \geq 0$.

To facilitate the subsequent analysis, the expressions in (1.13) and (1.14) are

rewritten as

$$C_e\dot{e} = \tilde{N}_e + N_{ed} - u_e - M\eta, \qquad C_r\dot{\eta} = \tilde{N}_r + N_{rd} + u_r - C_r\dot{T}_{vr} \qquad (1.16)$$

where the auxiliary signals $\tilde{N}_e(T_e, t)$ and $\tilde{N}_r(T_e, T_r, t)$ are defined as

$$\tilde{N}_e \triangleq N_e - N_{ed}, \qquad \tilde{N}_r \triangleq N_r - N_{rd}. \qquad (1.17)$$

Further, the signals $N_e(T_e, t)$ and $N_r(T_e, T_r, t)$ are defined as

$$N_e \triangleq C_e\dot{T}_{ed} - Q_{in} + M(T_e - T_{vro}), \qquad N_r \triangleq M(T_e - T_r) - Q_o \qquad (1.18)$$

with both $N_{ed}(t)$ and $N_{rd}(t)$ represented as

$$N_{ed} \triangleq N_e\big|_{T_e = T_{ed}} = C_e\dot{T}_{ed} - Q_{in} + M(T_{ed} - T_{vro}),$$

$$N_{rd} \triangleq N_r\big|_{T_e = T_{ed}, T_r = T_{vr}} = M(T_{ed} - T_{vr}) - Q_o. \qquad (1.19)$$

Based on (1.17) through (1.19), the control laws $u_e(t)$ and $u_r(t)$ introduced in (1.16) are designed as

$$u_e = k_e e, \qquad u_r = -k_r \eta + \bar{u}_r \tag{1.20}$$

where $\bar{u}_r(t)$ is selected as

$$\bar{u}_r = \left\{ \begin{array}{ll} 2Me, & \forall u_e \in (-\infty, 0) \\ \left(2M - k_e \dfrac{C_r}{C_e} - \dfrac{C_r k_e^2}{C_e M} \right) e - \dfrac{C_r k_e}{C_e} \eta, & \forall u_e \in [0, \infty) \end{array} \right\}. \tag{1.21}$$

Knowledge of $u_e(t)$ and $u_r(t)$, based on (1.20) and (1.21), allows the commutation relationships of (1.15) to be calculated which provides $\dot{m}_r(t)$ and $\dot{m}_f(t)$. Finally, the voltage signals for the pump and fan are prescribed using $\dot{m}_r(t)$ and $\dot{m}_f(t)$ with *a priori* empirical relationships.

Stability Analysis

A Lyapunov–based stability analysis guarantees that the advanced thermal management system will be stable when applying the control laws introduced in (1.20) and (1.21).

Theorem 1.1: *The controller given in (1.20) and (1.21) ensures that: (i) all closed–loop signals stay bounded for all time; and (ii) tracking is uniformly ultimately bounded (UUB) in the sense that $|e(t)| \leq \varepsilon_e$ and $|\eta(t)| \leq \varepsilon_r$ as $t \to \infty$ where $\varepsilon_e, \varepsilon_r \in \mathbb{R}^+$ are small constants.*

Proof: *See Appendix A for the complete Lyapunov–based stability analysis.*

Normal Radiator Operation Strategy

The electric radiator fan must be controlled harmoniously with the other thermal management system actuators to ensure proper power consumption. From the

backstepping robust control strategy, a virtual reference for the radiator temperature, $T_{vr}(t)$, is designed to facilitate the radiator fan control law (refer to Remark 1.1). A tracking error signal, $\eta(t)$, is introduced for the radiator temperature. Based on the radiator's mathematical description in (1.2), the radiator may operate normally, as a heat exchanger, if the effort of the radiator fan $\varepsilon c_{pa} \dot{m}_f \left(T_e - T_\infty \right)$, denoted by $u_r(t)$ in (1.23), is set to equal the effort produced by the coolant pump $c_{pc} \dot{m}_r \left(T_e - T_r \right)$, denoted by $u_e(t)$ in (1.22) and (1.23). Therefore, the control input $u_e(t)$ provides the signals $\dot{m}_r(t)$ and $\dot{m}_f(t)$.

To derive the operating strategy, the system dynamics (1.1) and (1.2) can be written as

$$C_e \dot{T}_e = Q_{in} - u_e \tag{1.22}$$

$$C_r \dot{T}_r = -Q_o + u_e - u_r . \tag{1.23}$$

If $u_r(t)$ is selected so that it equals $u_e(t)$, then the radiator operates normally. The control input $u_e(t)$ can be designed, utilizing a Lyapunov–based analysis, to robustly regulate the temperature of the engine block as

$$u_e = -\left(k_e + \alpha_e \right)\left[e - e_o \right] - \int_{t_o}^{t} \left[\alpha_e \left(k_e + \alpha_e \right) e(\tau) + \rho_e \operatorname{sgn}(e(\tau)) \right] d\tau \tag{1.24}$$

where the last term in (1.24) compensates for the variable unmeasurable input heat, $Q_{in}(t)$. Refer to Setlur *et al.* (2005) for more details on this robust control design method.

Remark 1.3: *The control input* $\dot{m}_r(t)$ *is uni–polar. Again, a commutation strategy may be designed to implement the bi–polar input* $u_e(t)$ *as*

$$\dot{m}_r \triangleq \frac{u_e\left[1+\operatorname{sgn}\left(u_e\right)\right]}{2c_{pc}\left(T_e-T_r\right)}. \qquad (1.25)$$

From this definition, if $u_e(t) \in L_\infty \forall t \geq 0$, *then* $\dot{m}_r(t) \in L_\infty \forall t \geq 0$. *The choice of the valve position and coolant pump's speed to produce the required control input* $\dot{m}_r(t)$, *defined in (1.25), can be determined based on energy optimization issues. Further, this allows* $\dot{m}_r(t)$ *to approach zero without stagnation of the coolant since* $\dot{m}_r = H\dot{m}_c$ *and* $0 \leq H \leq 1$. *Another commutation strategy is needed to compute the uni–polar control input* $\dot{m}_f(t)$ *so that*

$$\dot{m}_f \triangleq \frac{u_r\left[1+\operatorname{sgn}\left(u_r\right)\right]}{2\varepsilon c_{pa}\left(T_e-T_\infty\right)} \qquad (1.26)$$

where $u_r = u_e$. *From this definition, if* $u_r(t) \in L_\infty \forall t \geq 0$, *then* $\dot{m}_f(t) \in L_\infty \forall t \geq 0$.

Thermal Test Bench

An experimental test bench (refer to Figure 1.2) has been fabricated to demonstrate the proposed advanced thermal management system controller design. The assembled test bench offers a flexible, rapid, repeatable, and safe testing environment. Clemson University facilities generated steam is utilized to rapidly heat the coolant circulating within the cooling system via a two–pass shell and tube heat exchanger. The heated coolant is then routed through a 6.0L diesel engine block to emulate the combustion process heat. From the engine block, the coolant flows to a three–way smart valve and then either through the bypass or radiator to the coolant pump to close the loop. The thermal response of the engine block to the adjustable, externally applied heat source emulates the heat transfer process between the combustion gases, cylinder wall, and coolant jacket in an actual operating engine. As shown in Figure 1, the system sensors

include three J–type thermocouples (*e.g.*, T_1 = engine temperature, T_2 = radiator temperature, and T_3 = ambient temperature), two mass flow meters (*e.g.*, M_1 = coolant mass flow meter, and M_2 = air mass flow meter), and electric voltage and current measurements (*e.g.*, P_1 = valve power consumed, P_2 = pump power consumed, and P_3 = fan power consumed).
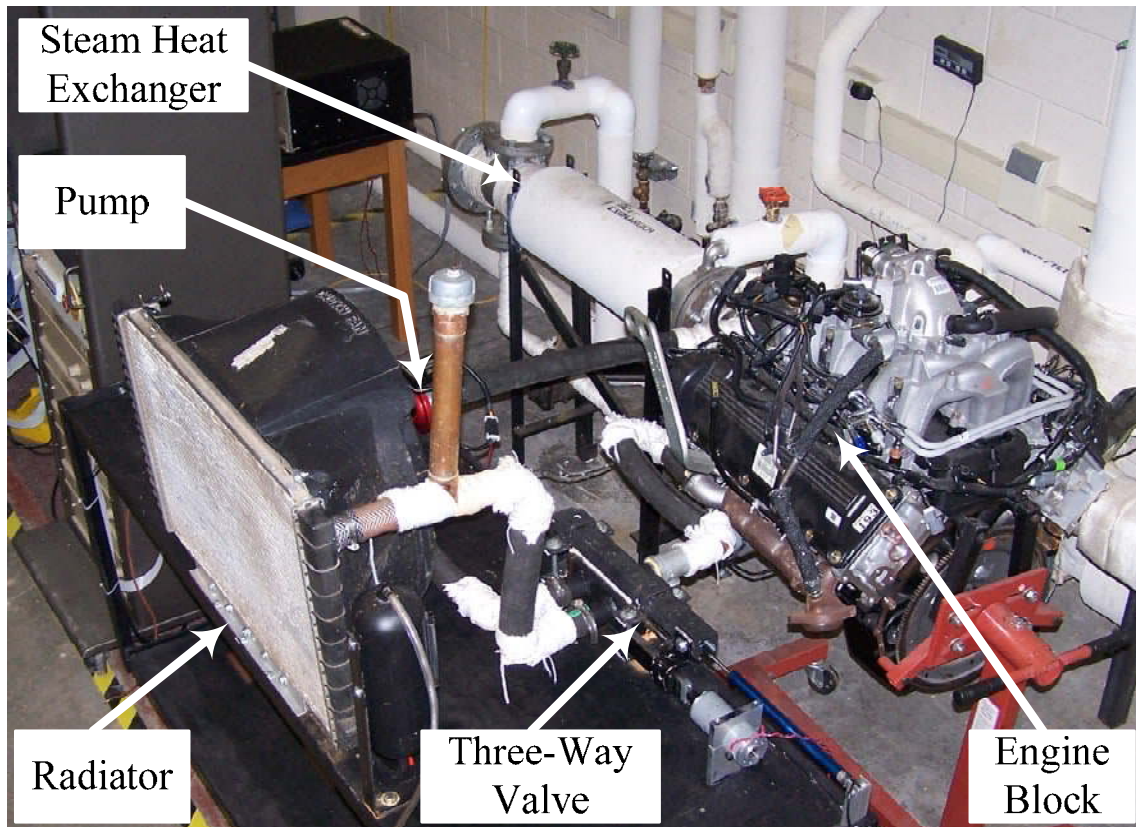
Figure 1.2 Experimental thermal test bench that features a 6.0L diesel engine block, three–way smart valve, electric coolant pump, electric radiator fan, radiator, and steam–based heat exchanger

The steam bench can provide up to 55kW of energy. High pressure saturated steam (412kPa) is routed from the campus facilities plant to the steam test bench, where a pressure regulator reduces the steam pressure to 172kPa before it enters the low pressure filter. The low pressure saturated steam is then routed to the double pass steam heat

exchanger to heat the system's coolant. The amount of energy transferred to the system is controlled by the main valve mounted on the heat exchanger. The mass flow rate of condensate is proportional to the energy transfer to the circulating coolant. Condensed steam may be collected and measured to calculate the rate of energy transfer. From steam tables, the enthalpy of condensation can be acquired. To facilitate the analysis, pure saturated steam and condensate at approximately T=100ºC determines the enthalpy of condensation. Baseline testing was performed to determine the average energy transferred to the coolant at various steam control valve positions. The coolant temperatures were initialized at T_e =67ºC before measuring the condensate. Each test was executed for different time periods.

Numerical and Experimental Results

In this section, the numerical and experimental results are presented to verify and validate the mathematical models and control design. First, a set of Matlab/Simulink™ simulations have been created and executed to evaluate the backstepping robust control design and the normal radiator operation strategy. The proposed thermal model parameters used in the simulations are C_e=17.14kJ/ºK, C_r=8.36kJ/ºK, c_{pc}=4.18kJ/kg.ºK, c_{pa}=1kJ/kg.ºK, ε =0.6, and T_∞ =293ºK. Second, a set of experimental tests have been conducted on the steam–based thermal test bench to investigate the control design and operation strategies.

Backstepping Robust Control

A numerical simulation of the backstepping robust control strategy, introduced in Section 1.3, has been performed on the system dynamics (1.1) and (1.2) to demonstrate the performance of the proposed controller in (1.20) and (1.21). For added reality, band–limited white noise was added to the plant using a MATLAB block (noise power =0.1). To simplify the subsequent analysis, a fixed smart valve position of $H = 1$ (*e.g.*, fully closed for 100% radiator flow) has been applied to investigate the coolant pump's ability to regulate the engine temperature. An external ram air disturbance was introduced to emulate a vehicle traveling at 20km/h with varying input heat of Q_{in}=[50kW, 40kW, 20kW, 35kW] as shown in Figure 1.3. The initial simulation conditions were $T_e(0)$=350ºK and $T_r(0)$=340ºK. The control design constants are T_{vro}=356ºK and m_o=0.4. Similarly, the controller gains were selected as k_e=40 and k_r=0.005. The desired engine temperature varied as T_{ed}=363+sin(0.05t)ºK. This time varying setpoint allows the controller's tracking performance to be studied.

In Figure 1.3a, the backstepping robust controller readily handles the heat fluctuations in the system at t=[200sec, 500sec, 800sec]. For instance, when Q_{in}=50kW (heavy thermal load) is applied from $0 \le t \le 200$ sec, as well as when Q_{in}=20kW (light thermal load) is applied at $500 \le t \le 800$ sec, the controller is able to maintain a maximum absolute value tracking error of 1.5ºK. Under the presented operating condition, the error in Figure 1.3b fluctuates between –0.4ºK and –1.5ºK. In Figures 1.3c and 1.3d, the

coolant pump (maximum flow limit of 2.6kg/sec) works harder than the radiator fan which is ideal for power minimization.

Remark 1.4: *The error fluctuation in Figure 1.3b is quite good when compared to the overall amount of heat handled by the cooling system components.*

Figure 1.3 Numerical response of the backstepping robust controller for variable engine thermal loads. (a) Simulated engine temperature response for desired engine temperature profile $T_{ed} = 363 + \sin(0.05t)$ °K; (b) Simulated engine commanded temperature tracking error; (c) Simulated mass flow rate through the pump; and (d) Simulated air mass flow rate through the radiator fan

Two scenarios have been implemented to investigate the controller's performance on the experimental test bench. The first case applies a fixed input heat of Q_{in} =35kW and a ram air disturbance which emulates a vehicle traveling at 20km/h as shown in Figure 1.4. From Figure 1.4b, the controller can achieve a steady state absolute value

17

temperature tracking error of 0.7ºK. In Figures 1.4c and 1.4d, the coolant pump works harder than the radiator fan which again is ideal for power minimization. Note that the coolant pump reaches its maximum mass flow rate of 2.6kg/sec, and that the fan runs at 73% of its maximum speed (*e.g.*, maximum air mass flow rate is 1.16kg/sec). The fluctuation in the coolant and air mass flow rates during $0 \le t \le 400$ sec (refer to Figures 1.4c and 1.4d) is due to the fluctuation in the actual radiator temperature about the radiator temperature virtual reference T_{vro} =356ºK as shown in Figure 1.4a.
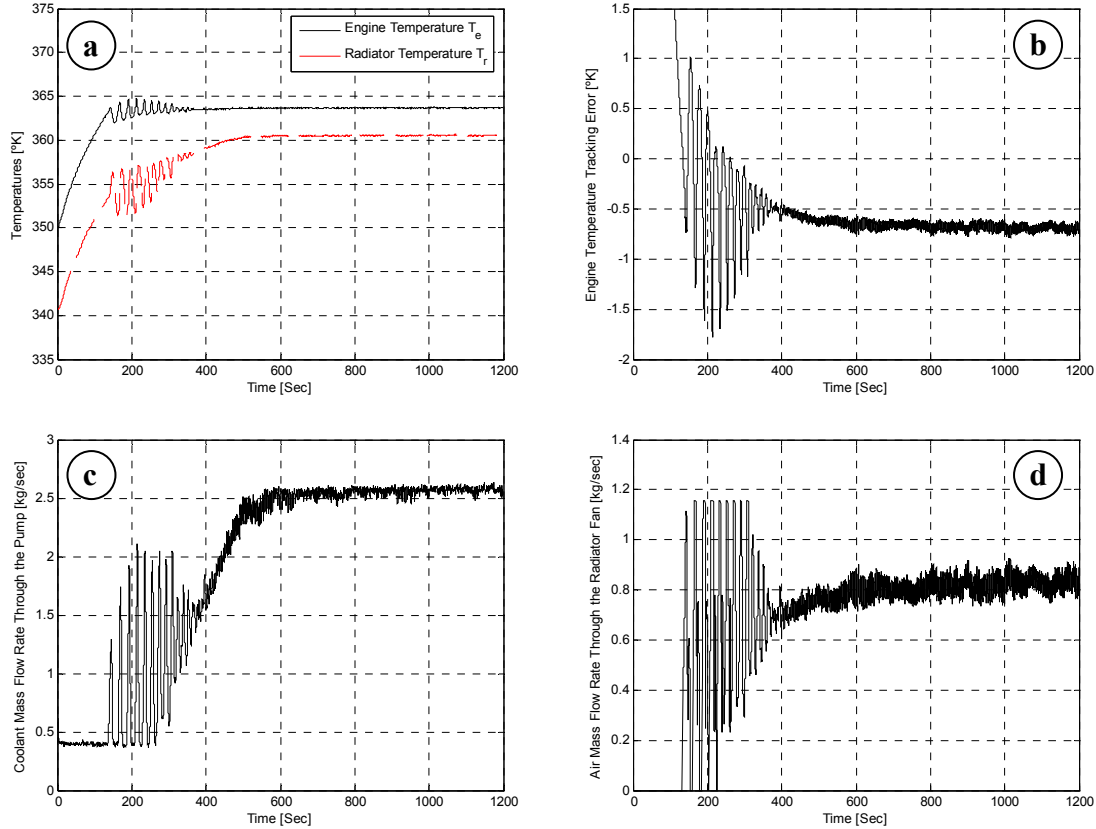
Figure 1.4 First experimental test scenario for the backstepping robust controller with emulated vehicle speed of 20km/h and Q_{in} =35kW. (a) Experimental engine and radiator temperatures with a desired engine temperature T_{ed} =363ºK; (b) Experimental engine temperature tracking error; (c) Experimental coolant mass flow rate through the pump; and (d) Experimental air mass flow rate through the radiator fan

The second scenario varies both the input heat and disturbance. Specifically $Q_{in}(t)$ changes from 50kW to 35kW at $t=200$sec while $Q_o(t)$ varies from 20km/h to 40km/h to 20km/h at $t=400$sec and 700sec (refer to Figure 1.5). From Figure 1.5b, it is clear that the proposed control strategy handles the input heat and ram air variations nicely. During the ram air variation between 550sec and 750sec, the temperature error fluctuates within 1ºK due to the oscillations in the coolant pump and radiator fan flow rates per Figures 1.5c and 1.5d. This behavior may be attributed to the supplied ram air that causes the actual radiator temperature, $T_r(t)$, to fluctuate about the radiator temperature virtual reference $T_{vro}=356$ºK in Figure 1.5a.

Normal Radiator Operation Strategy

The normal radiator operation strategy, introduced in Section 1.3, has been numerically simulated using system dynamics (1.1) and (1.2) to investigate the robust tracking controller performance given in (1.24). The simulated thermal system's parameters, initial simulation conditions, and desired engine temperature were equivalent to Section 1.5.1. Again, a band–limited white noise was added to the plant using a MATLAB block with noise power =0.1. A fixed 100% radiator flow smart valve position allows the coolant pump's ability to regulate the engine temperature to be studied. The external ram air emulated a vehicle traveling at 20km/h; the input heat was varied as shown in Figure 1.6 (*e.g.*, Q_{in}=[50kW, 40kW, 20kW, 35kW]). The control gains were set as $k_e=10$, $\alpha_e=0.005$, and $\rho_e=0.01$. Although the normal radiator operation accommodated the heat variations in Figure 1.6a, its performance was inferior to the

backstepping robust control. However, the normal radiator operation achieved less tracking error under the same operating condition when Figure 1.3b and 1.6b are compared. In this case, the maximum temperature tracking error fluctuation was 1ºK. In Figures 1.6c and 1.6d, the pump works harder than the fan which is preferred for power minimization. Note that the power consumption is larger than that achieved by the backstepping robust controller (refer to Figures 1.3c, 1.3d, 1.6c, and 1.6d).
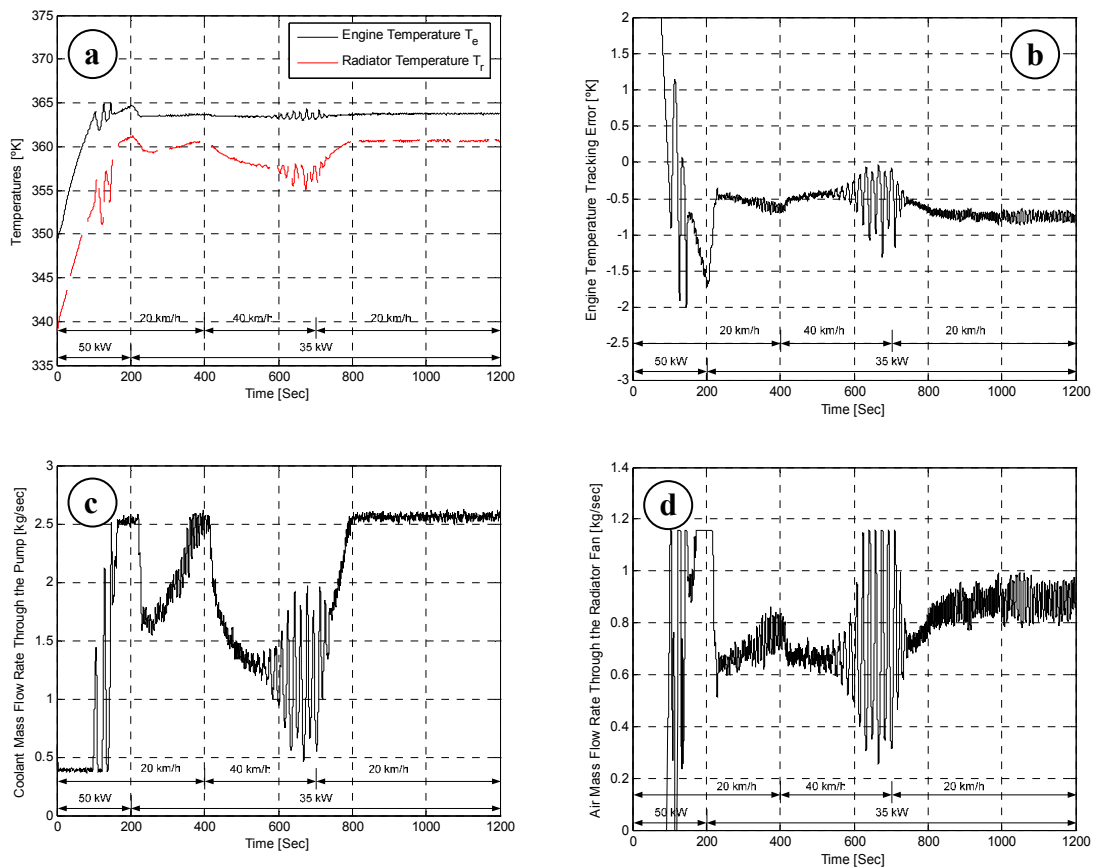
Figure 1.5 Second experimental test scenario for the backstepping robust controller where the input heat and ram air disturbance vary with time. (a) Experimental engine and radiator temperatures with a desired engine temperature T_{ed}=363ºK; (b) Experimental engine temperature tracking error; (c) Experimental coolant mass flow rate through the pump; and (d) Experimental air mass flow rate through the radiator fan

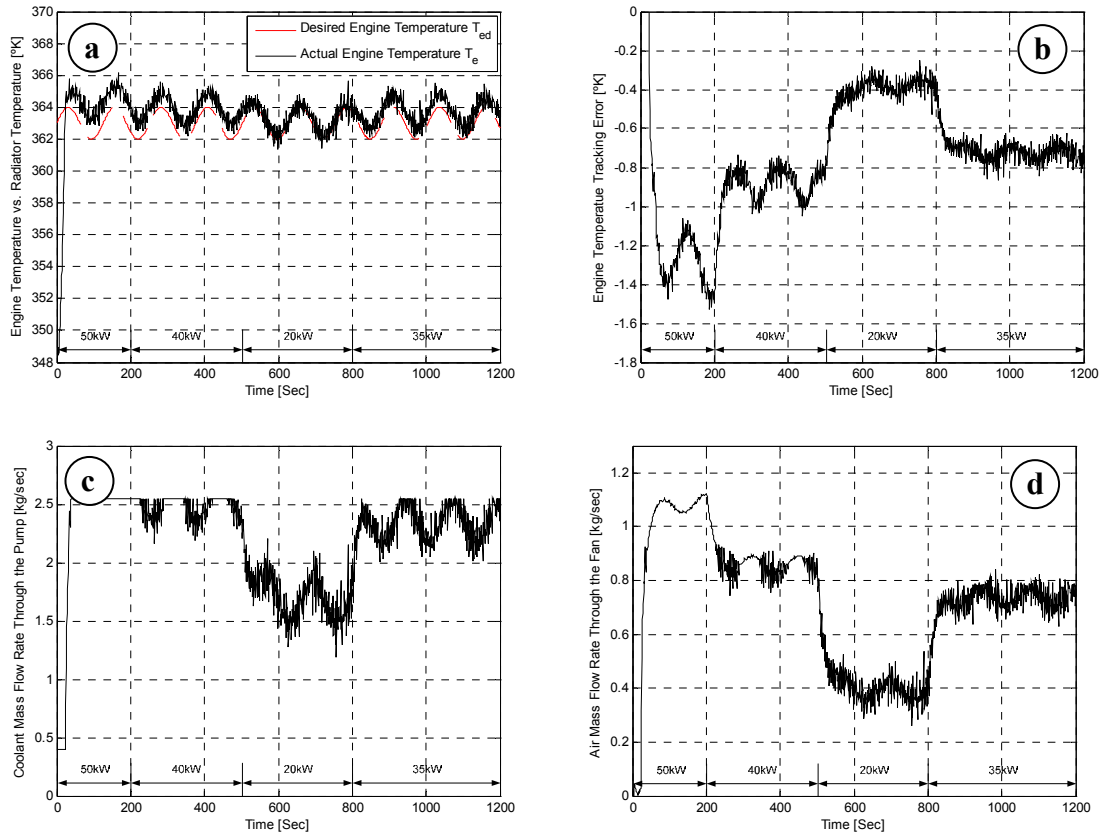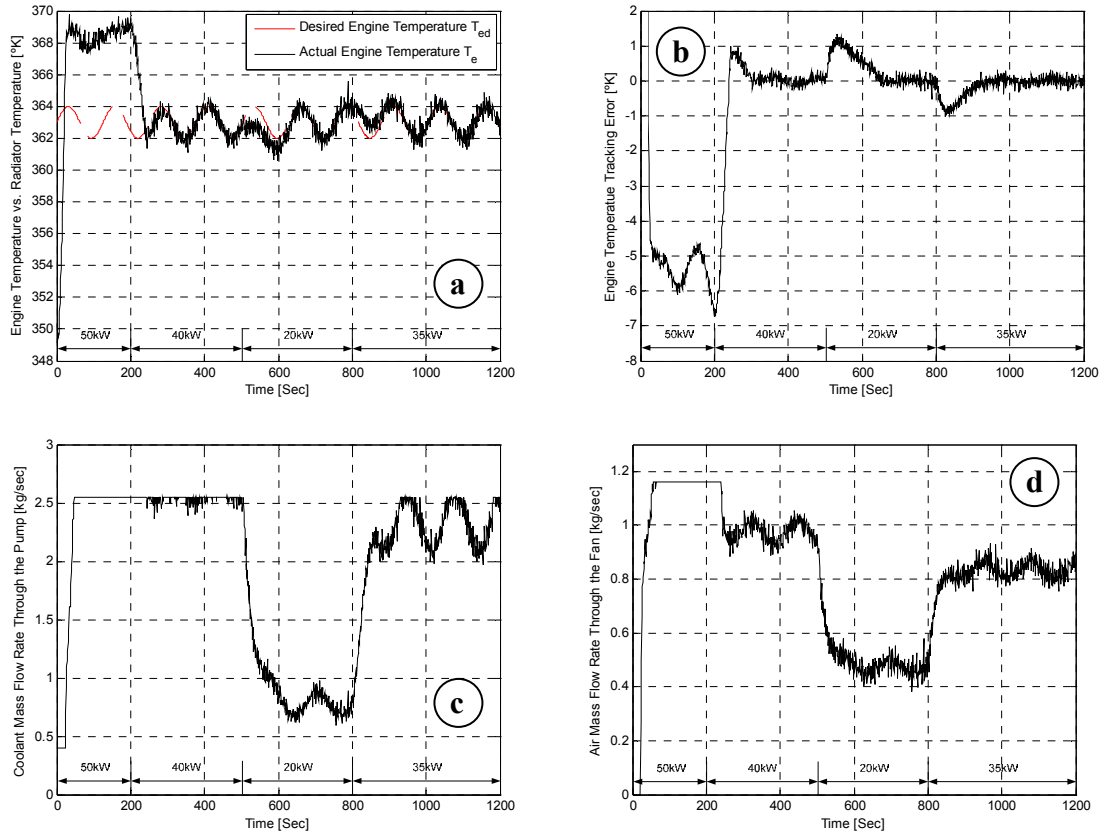Figure 1.6 Numerical response of the normal radiator operation for variable engine thermal loads. (a) Simulated engine temperature response for desired engine temperature profile T_{ed}=363+sin(0.05t)ºK; (b) Simulated engine commanded temperature tracking error; (c) Simulated mass flow rate through the pump; and (d) Simulated air mass flow rate through the radiator fan

The same two experimental scenarios presented for the backstepping robust controller are now implemented for the normal radiator operation strategy on the thermal test bench. In the first scenario, a fixed input heat and ram air disturbance, Q_{in}=35kW and 20km/h vehicle speed, were applied. In Figure 1.7a, the normal radiator operation overshoot and settling time are larger than the backstepping robust control (refer to Figure 1.4a). As shown in Figure 1.7b, an improved engine temperature tracking error was demonstrated but with greater power consumption in comparison to the backstepping

robust control (refer to Figure 1.4b). Finally, the coolant pump operated continuously at its maximum per Figure 1.7c.
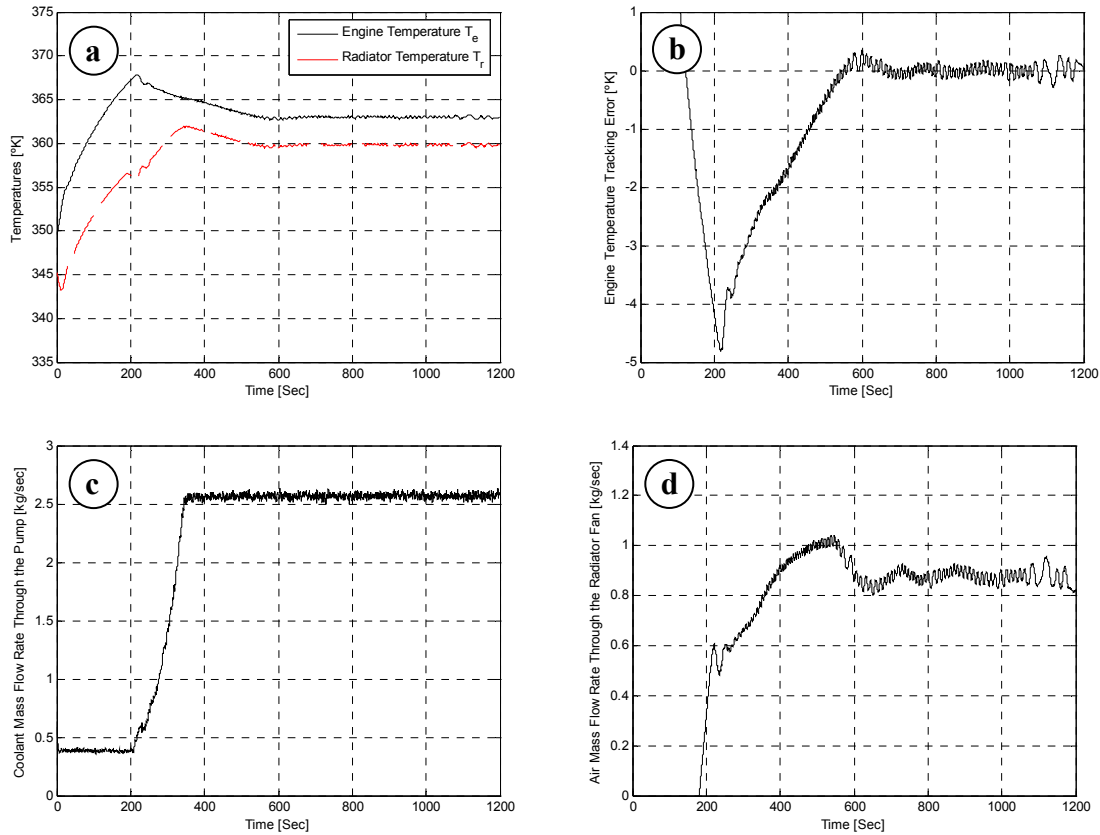
Figure 1.7 First experimental test scenario for the normal radiator operation controller with emulated speed of 20km/h and Q_{in}=35kW. (a) Experimental engine and radiator temperatures with a desired engine temperature T_{ed}=363ºK; (b) Experimental engine temperature tracking error; (c) Experimental coolant mass flow rate through the pump; and (d) Experimental air mass flow rate through the radiator fan

For the second test scenario, the input heat and disturbance are both varied as previously described for the backstepping robust control. The normal radiator operation maintained the established control gains. In Figure 1.8b, the temperature error remains within a ±0.4ºK neighborhood of zero despite variations in the input heat and ram air.

Although the temperature tracking error is quite good, this strategy does not minimize power consumption in comparison to the backstepping robust control strategy.
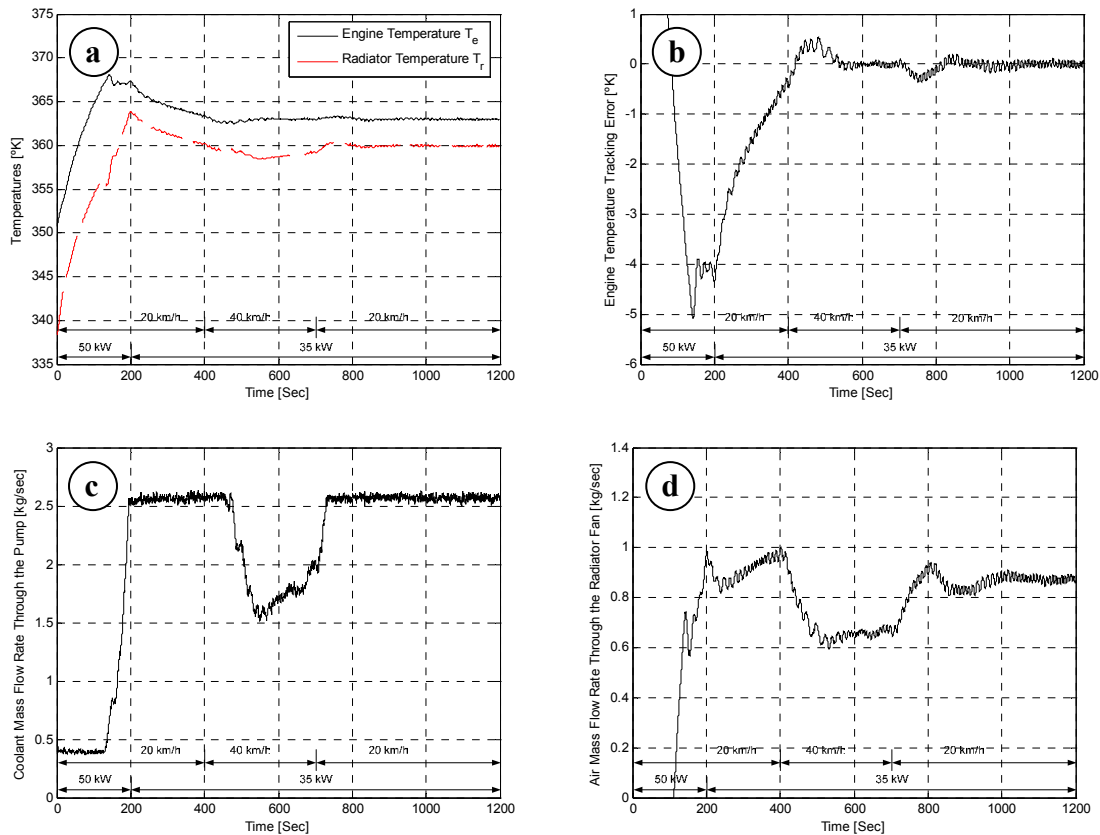
Figure 1.8 Second experimental test scenario for the normal radiator operation controller where the input heat and ram air disturbance vary with time. (a) Experimental engine and radiator temperatures with a desired engine temperature T_{ed}=363ºK; (b) Experimental engine temperature tracking error; (c) Experimental coolant mass flow rate through the pump; and (d) Experimental air mass flow rate through the radiator fan

The simulation and experimental results are summarized in Table 1.1 to compare the controller strategies. To ensure uniform operating conditions, all reported data corresponds to the first scenario thermal conditions. Further, the controller gains, initial conditions, and temperature set points were maintained for both the simulation and experimental tests. Note that adaptive and robust controllers were also designed and

implemented (Salah *et al.*, 2006) for comparison purposes. However, the designs are not reported in this paper. For these two controllers, the radiator temperature set point was required which may be considered a weakness.

Overall, the normal radiator operation strategy was better than the adaptive and robust control strategies. However, it is not as good as the backstepping control when compared in terms of power consumption despite achieving less temperature tracking error. Therefore, the backstepping robust control strategy is considered to be the best among all controllers and operation strategies. The power measure is the minimum, the heat change handling is more satisfactory, and a set point for the radiator temperature is not required. From Table 1.1, it is clear that the variations in the actual coolant temperature about the set point, quantified by the steady state tracking error, are relatively minor given that the maximum absolute tracking error is 0.3% (*e.g.*, adaptive control).

Remark 1.5: The cooling system power consumption $P_{sys}\left(\dot{m}_c, \dot{m}_f\right)$ measures/calculates the average power consumed by the system actuators over the time *T=20min*. Power measure is performed for the duration of the experimental test (*T*) using the trapezoidal method of integration. The power consumed by the smart valve is considered to be quite small so it is neglected.

Description	$\lvert e_{ss} \rvert$ [°K]		P_{sys} [W]	
	Simulation	Experiment	Simulation	Experiment
Backstepping robust control	0.616	0.695	31.625	33.231
Normal radiator operation strategy	0.105	0.175	38.052	38.699
Adaptive control	1.003	1.075	37.497	37.968
Robust control	0.905	0.935	34.346	35.786

Table 1.1 Simulation and experimental results summary for four control strategies

Concluded Remarks

Advanced automotive thermal management system can have a positive impact on gasoline and diesel engine cooling systems. In this paper, a suit of servo–motor based– cooling system components have been assembled and controlled using a Lyapunov–based nonlinear control technique. The control algorithm has been investigated using both simulation and experimental tests. Two detailed and two supplemental controllers were applied to regulate the engine temperature. In each instance, the controllers successfully maintained the engine block to setpoint temperatures with small error percentages. It has also been shown that the power consumed by the system actuators can be reduced. Overall, the findings demonstrated that setpoint temperatures can be maintained satisfactory while minimizing power consumption which ultimately impacts fuel economy.

CHAPTER 2
MULTIPLE COOLING LOOPS IN ADVANCED VEHICLE THERMAL
MANAGEMENT SYSETMS

Introduction

Advance automotive thermal management systems can effectively maintain the desired temperature in internal combustion engines for enhanced performance (Melzer *et al.*, 1999). Automotive cooling systems can be upgraded to computer controlled servo–motor actuated components rather than the conventional wax–based thermostat valve, mechanical coolant pump, and viscous clutch radiator fan (Chalgren and Barron, 2003). The adjustment of thermal system operation per driving condition can reduce the fuel consumption, parasitic losses, and tailpipe emissions during transient and steady–state operation (Wambsganss, 1999). Geels *et al.* (2003) reported that reductions of 5%, 20%, and 10% in engine fuel consumption and tail pipe emissions for CO and HC can be achieved when transforming from mechanical to electrical cooling system components within the vehicle. The underhood powertrain components and cabin environment must be maintained within desired temperature ranges. The main cooling loop ensures that the engine block does not overheat leading to coolant boiling. Similarly, the transmission oil is cooled by pumping the fluid through an auxiliary heat exchanger typically located inside the radiator. Further, the compressed air exiting a turbocharger's compressor may be cooled before entering the engine's cylinders using a charge–air–cooler. Finally, the heater core conditions the passenger compartment air temperature for occupant specified comfort levels.

A short literature review will be presented. Cho *et al.* (2004) investigated a controllable electric coolant pump in a class–three medium duty diesel engine truck in terms of cooling circuit thermal performance. Page *et al.* (2005) implemented an intelligent thermal management system on a medium–sized tactical vehicle to study improvements in the engine's peak fuel consumption and thermal operating conditions. Redfield *et al.* (2006) examined potential energy savings for engine cooling in class–eight tractors. They demonstrated ±3ºC temperature tracking for prescribed set point values. Although advanced automotive thermal management systems offer significant benefits, few researches have focused on secondary cooling loops (Chalgren and Traczyk, 2005). Chalgren and Allen (2005) applied advanced thermal management systems concepts to the transmission, EGR cooler, and charge–air–cooler for a light duty diesel truck. They reported that temperature controllability was remarkably improved for the intake manifold air, engine block, engine coolant, and engine oil as well as a greater heat rejection capability while decreasing the cooling system parasitic losses. Note that the charge–air–cooler loop can improve the fuel economy and combustion by decreasing the compressed inlet air temperature (Taitt *et al.*, 2006).

A wide range of controller designs have been implemented to control the smart components in advanced cooling systems. Wagner *et al.* (2002 and 2003) introduced real–time thermal control algorithms for the synchronous regulation of the servo–motor driven thermostat valve and coolant pump. Choukroun and Chanfreau (2001) modified the classic cooling loop by using electro–mechanical components and a proportional integral (PI) control technique. Cipollone and Villante (2004) proposed different cooling

control schemes for a proportional valve as a replacement to the traditional thermostat valve. Setlur *et al.* (2005) presented a suite of mathematical models to describe the engine cooling loop thermal behavior and controllable electro–mechanical multiple actuators. They developed nonlinear control algorithms for the servo–motor cooling system actuators for temperature regulation. Salah *et al.* (2008) developed a backstepping robust controller and a normal radiator operation using a lumped parameter model to operate harmoniously the system actuators.

In this chapter, a multiple (*i.e.*, engine and transmission) loop advanced thermal management system will be investigated and analyzed. Section 2.2 presents mathematical models to describe the cooling system dynamics. Nonlinear tracking control strategies are introduced in Section 2.3 to accommodate disturbances and uncertainties. Section 2.4 presents the experimental test bench that features a smart thermostat valve, variable speed electric coolant and transmission pumps, variable speed electric radiator fan, radiator, 6.0L engine block, automatic transmission, and a multiple output steam–based heat exchanger to emulate the combustion and transmission heating processes. In Section 2.5, representative experimental results are introduced for five test cases (*e.g.*, steady input heat for normal and elevated ambient temperature, variable set point temperature, variable input heat with ram air disturbance, and controller design comparisons). The summary is contained in Section 2.6.

28

Automotive Multi–Loop Cooling System Behavior

The thermal response of a multi–loop advanced cooling system can be represented by a suite of lumped parameter mathematical descriptions. The automotive powertrain elements included a 6.0L diesel engine, automatic transmission, and radiator as shown in Figure 2.1. The engine's thermal management system features a three–way smart valve, variable speed electric coolant pump, and a variable speed electric radiator fan. The transmission loop features a variable speed electric pump with a secondary radiator. Finally, the charge–air–cooler (air–to–coolant heat exchanger) was a simple loop to reduce air temperature after compression with an integrated coolant pump. A multiple output steam–based heat exchanger emulated the engine combustion and transmission heat processes.
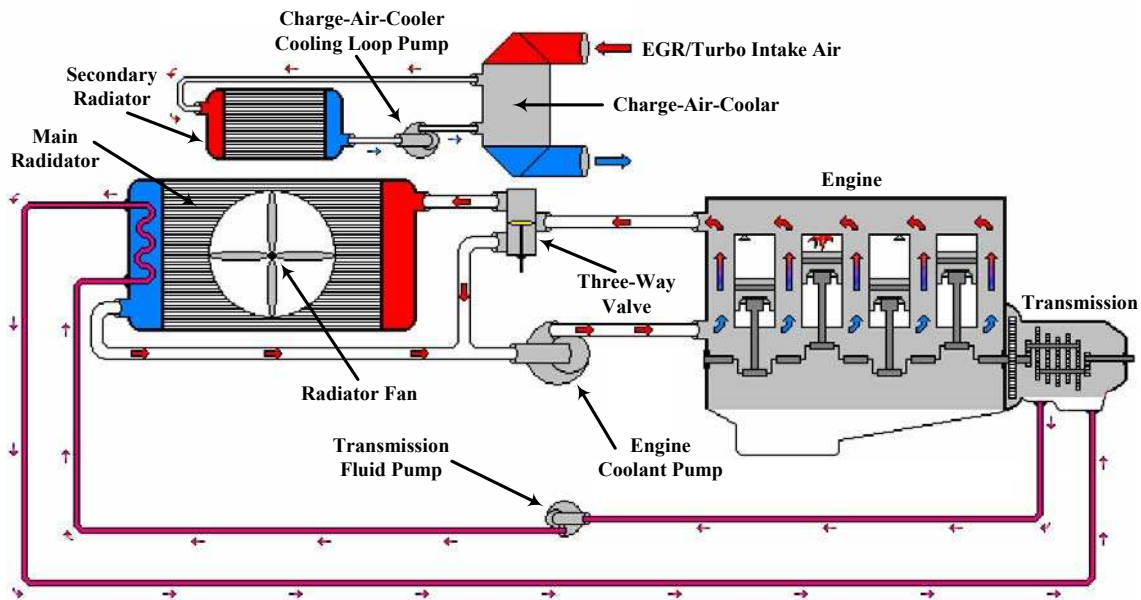
Figure 2.1 Multi–loop advanced cooling system which features a three–way smart valve, two variable speed electric pumps, constant speed electric pump, a variable speed electric radiator fan, an engine block, a transmission, a radiator, a charge–air–cooler, and various sensors (temperature, mass flow rate, and power)

29

A series of reduced–order thermal models describe the multi–loop cooling system's transient response to minimize the computational burden for in–vehicle implementation. The thermal behavior of the engine, transmission, and radiator can be described as

$$C_e \dot{T}_e = Q_e - c_{pc} \dot{m}_{cr} \left(T_e - T_{re} \right) \tag{2.1}$$

$$C_t \dot{T}_t = Q_t - c_{po} \dot{m}_{ot} \left(T_t - T_{rt} \right) \tag{2.2}$$

$$C_r \dot{T}_{re} = -Q_a + c_{pc} \dot{m}_{cr} \left(T_e - T_{re} \right) + c_{po} \dot{m}_{ot} \left(T_t - T_{rt} \right) - \varepsilon_r \, c_{pa} \dot{m}_{ar} \left(T_e - T_\infty \right). \tag{2.3}$$

The variables $Q_e(t)$, $Q_t(t)$, and $Q_a(t)$ represent the heat produced by the combustion process, the transmission heat generated, and the radiator heat loss due to uncontrollable ram air flow. An adjustable multiple output double pass steam–based heat exchanger delivered the virtual combustion and transmission heat at a maximum of 56kW and 4kW, respectively. In an actual vehicle, the heat generated by the engine combustion process is transferred to the coolant through the block's coolant jacket, while the heat generated by the transmission is transferred to the oil by the transmission gears.

For a three way servo–driven thermostat valve, the radiator coolant mass flow rate (in the engine loop), $\dot{m}_{cr}(t)$, is based on the coolant pump flow rate and normalized valve position so that $\dot{m}_{cr} = H \dot{m}_{ce}$ where $0 \le H \le 1$. Note that $H(t) = 1(0)$ corresponds to a fully closed (open) valve position and coolant flow through the radiator (bypass) loop. The two–node lumped parameter thermal model that describes the charge–air–cooler dynamic behavior may be expressed as

$$C_a \dot{T}_{ao} = c_{pa} \dot{m}_a \left(T_{ai} - T_{ao} \right) - \varepsilon_{cac} c_{pc} \dot{m}_{csr} \left(T_{co} - T_{ci} \right) \tag{2.4}$$

$$C_c \dot{T}_{co} = \varepsilon_{cac} c_{pa} \dot{m}_a \left(T_{ai} - T_{ao} \right) - c_{pc} \dot{m}_{csr} \left(T_{co} - T_{ci} \right) \tag{2.5}$$

$$C_{sr} \dot{T}_{ci} = c_{pc} \dot{m}_{csr} \left(T_{co} - T_{ci} \right) - Q_{sr}. \tag{2.6}$$

The variable $Q_{sr} = Q_a + Q_{rf}$ represents the heat loss in the secondary radiator due to the ram air flow, $Q_a(t)$, and the air blown by the primary radiator fan, $Q_{rf}(t)$. Since the heat generated in the charge–air–cooler air–side, $c_{pa} \dot{m}_a \left(T_{ao} - T_{ai} \right)$, is not totally transferred to the charge–air–cooler coolant–side loop, it is multiplied by the effectiveness of the charge–air–cooler heat exchanger, ε_{cac}, as shown in equation (2.5). The heat loss in the secondary radiator, $Q_{sr}(t)$, can be computed from $Q_{sr} = A_{sr} h_{sr} \left(T_{co} - T_{\infty} \right)$ where $h_{sr}(\cdot)$ is a function of the air mass flow rate, $\dot{m}_{asr}(t)$, through the secondary radiator.

<u>Control System Design for Multiple Thermal Loops</u>

A Lyapunov–based nonlinear control algorithm will be developed to maintain a desired engine block temperature, $T_{ed}(t)$, and a desired transmission temperature, $T_{td}(t)$, subject to variable uncertainties in the described multi–loop cooling system model. The controller's main objective is to track the engine and transmission temperature prescribed set points while compensating for the variable system uncertainties (*i.e.*, combustion process input heat, $Q_e(t)$, heat generated in the transmission, $Q_t(t)$, and radiator heat loss, $Q_a(t)$) by harmoniously controlling the system's electro–mechanical actuators. Although other linear and nonlinear control algorithms may be formulated (Ap and Tarquis, 2005), Lyapunov–based nonlinear control strategies demonstrate outstanding

disturbance rejection qualities (Salah *et al.*, 2008). The system servo–actuators are a three–way smart valve, two coolant pumps, an oil pump, and a radiator fan as shown in Figure 2.1. An important objective is to reduce the electric power consumed by these actuators, $P_{sys}(t)$.

To facilitate the controller design process, three assumptions are imposed.

Assumption 2.1: *The signals $Q_e(t), Q_t(t)$, and $Q_a(t)$ always remain positive in equations (2.1–2.3) (i.e., $Q_e(t), Q_t(t), Q_a(t) \geq 0$). Further, the signals $Q_e(t)$ and $Q_t(t)$ with their first two time derivatives remain bounded at all time, such that $Q_e(t), Q_t(t), \dot{Q}_e(t), \dot{Q}_t(t), \ddot{Q}_e(t), \ddot{Q}_t(t) \in L_\infty$, as well as $Q_a(t)$ to be bounded, such that $Q_a(t) \in L_\infty$.*

Assumption 2.2: *The surrounding ambient temperature $T_\infty(t)$ is uniform and satisfies the condition $T_e(t) - T_\infty(t) \geq \varepsilon_1$ at all time where $\varepsilon_1 \in \mathbb{R}^+$ is a constants.*

Assumption 2.3: *The coolant temperatures at the engine block and radiator outlets satisfy the condition $T_e(t) - T_{re}(t) \geq \varepsilon_2$ at all time where $\varepsilon_2 \in \mathbb{R}^+$ is a constant. Further, $T_e(0) \geq T_{re}(0)$ to facilitate the boundedness of signal argument.*

Assumption 2.3 allows the engine and radiator outlets' coolant to have the same initial temperature (*e.g.*, cold start). The unlikely case of $T_e(0) < T_{re}(0)$ is not considered. It is important to point out that in equations (2.1–2.3), the signals $T_e(t), T_{re}(t), T_t(t), T_{rt}(t)$, and $T_\infty(t)$ can be measured by either thermocouples or thermistors, and the system parameters C_e, C_t, C_r, c_{pc}, c_{po}, c_{pa}, and ε_r are assumed to be constant and fully known.

<u>Control Objective for Multi–Loop Thermal System</u>

The control objective is to ensure that the actual temperatures of the engine, $T_e(t)$, and transmission, $T_t(t)$, track the desired trajectories $T_{ed}(t)$ and $T_{td}(t)$, respectively, such that

$$T_e(t) \to T_{ed}(t), \quad T_t(t) \to T_{td}(t) \quad \text{as} \quad t \to \infty \tag{2.7}$$

while compensating for the system variable uncertainties $Q_e(t)$, $Q_t(t)$, and $Q_a(t)$. Another assumption has been imposed to facilitate the boundedness of signal arguments.

Assumption 2.4: *The engine, and transmission temperature profiles are always bounded and chosen such that their first three time derivatives remain bounded at all times (i.e., $T_{ed}(t)$, $T_{td}(t)$, $\dot{T}_{ed}(t)$, $\dot{T}_{td}(t)$, $\ddot{T}_{ed}(t)$, $\ddot{T}_{td}(t)$, $\dddot{T}_{ed}(t)$, $\dddot{T}_{td}(t) \in L_\infty$). Further, $T_{ed}(t) \gg T_\infty(t)$ and $T_{td}(t) \gg T_\infty(t)$ at all times.*

To facilitate the controller's development and quantify the temperature tracking control objective, the auxiliary signals $s_e(t)$, and $s_t(t)$ are defined as

$$s_e \triangleq \dot{\eta}_e + \alpha_e \eta_e, \quad s_t \triangleq \dot{\eta}_t + \alpha_t \eta_t \tag{2.8}$$

where α_e and α_t are real positive constants, and the tracking error signals $\eta_e(t)$, and $\eta_t(t)$ are defined as $\eta_e \triangleq T_{ed} - T_e$ and $\eta_t \triangleq T_{td} - T_t$.

Remark 2.1: *Standard arguments (Dawson et al., 1998) can be applied to show that (i) if $s_e(t), s_t(t) \in L_\infty$, then $\eta_e(t), \eta_t(t), \dot{\eta}_e(t), \dot{\eta}_t(t) \in L_\infty$, and (ii) if the signals $s_e(t)$ and $s_t(t)$ are asymptotically regulated, then the signals $\eta_e(t), \eta_t(t), \dot{\eta}_e(t), \dot{\eta}_t(t)$ are asymptotically regulated.*

<u>Controller Formulation and Development</u>

The multi–loop system, described by equations (2.1–2.3), can be written as

$$C_e \dot{T}_e = Q_e - u_e, \quad C_t \dot{T}_t = Q_t - u_t, \quad C_r \dot{T}_{rt} = -Q_a + u_r \tag{2.9}$$

33

where the control laws $u_e(t), u_t(t)$, and $u_r(t)$ are defined as $u_e \triangleq c_{pc} \dot{m}_{cr}(T_e - T_{re})$, $u_t \triangleq c_{po} \dot{m}_{ot}(T_t - T_{rt})$, and $u_r \triangleq u_e + u_t - \varepsilon_r c_{pa} \dot{m}_{ar}(T_e - T_\infty)$. To analyze the error system dynamics, the time derivatives of the first two expressions in equation (2.9) are computed and then both sides of the resulting equations are multiplied by C_e and C_t for the engine and transmission dynamics, respectively. Thus, the first two thermal dynamics in equation (2.9) can be substituted and then reformatted to realize

$$C_e \dot{s}_e = N_e + \dot{u}_e - \eta_e, \quad C_t \dot{s}_t = N_t + \dot{u}_t - \eta_t \tag{2.10}$$

where the auxiliary functions $N_e(T_e, \dot{T}_e, t)$ and $N_t(T_t, \dot{T}_t, t)$ are defined as

$$N_e \triangleq C_e \ddot{T}_{ed} - \dot{Q}_e + C_e \alpha_e \dot{\eta}_e + \eta_e, \quad N_t \triangleq C_t \ddot{T}_{td} - \dot{Q}_t + C_t \alpha_t \dot{\eta}_t + \eta_t . \tag{2.11}$$

The radiator may operate normally as a heat exchanger if the control law $u_r(t)$ is set to zero (Salah *et al.*, 2008). The expression $u_e + u_t = \varepsilon_r c_{pa} \dot{m}_{ar}(T_e - T_\infty)$ can be obtained by setting the control law $u_r(t)$ to zero.

Remark 2.2: *The control inputs $\dot{m}_{cr}(t), \dot{m}_o(t)$, and $\dot{m}_{ar}(t)$ are uni–polar. Hence, commutation strategies are designed to implement the bi–polar control laws $u_e(t)$ and $u_t(t)$ as*

$$\dot{m}_{cr} \triangleq \frac{[1 + \text{sgn}(u_e)] u_e}{2 c_{pc}(T_e - T_{re})}, \quad \dot{m}_{ot} \triangleq \frac{[1 + \text{sgn}(u_t)] u_t}{2(c_{po}|T_t - T_{rt}| + \varepsilon)} + \dot{m}_{ot\,\text{min}},$$

$$m_{ar} \triangleq \frac{[1 + \text{sgn}(F)] F}{2 \varepsilon_r c_{pa}(T_e - T_\infty)} \tag{2.12}$$

where $F \triangleq u_e + u_t$, and $\varepsilon \in \mathbb{R}^+$ is a constant that is selected arbitrary small to prevent any singularity condition. During the system warm–up, some heat is transferred to the transmission via the radiator since the engine heats up faster than the transmission. Thus, the condition $T_t(t) < T_{rt}(t)$ may occur. The control input, $\dot{m}_{ar}(t)$ is obtained from the control laws $u_e(t)$ and $u_t(t)$. It is clear from

the expressions in equation (2.12) that by setting the control law $u_r = 0$, the fan effort, denoted by $\varepsilon_r c_{pa} \dot{m}_{ar} (T_e - T_\infty)$, is set to equal the summation of the coolant pump effort in the engine loop, denoted by $c_{pc} \dot{m}_{cr} (T_e - T_{re})$, and the oil pump effort in the transmission loop, denoted by $c_{po} \dot{m}_{ot} (T_t - T_{rt})$. Further, if $u_e(t), u_t(t) \in L_\infty$ at all time, then $\dot{m}_{cr}(t), \dot{m}_{ot}(t), \dot{m}_{ar}(t) \in L_\infty$ at all time.

Remark 2.3: *The commutation strategy of the uni–polar control input $\dot{m}_{cr}(t)$, introduced in equation (2.12), is implemented utilizing the smart thermostat valve such that*

$$\dot{m}_{cr} \triangleq H \dot{m}_{ce}, \quad H \triangleq \begin{cases} 0, & T_e < T_{ed} - \Delta T \\ 1, & T_e \geq T_{ed} - \Delta T \end{cases}, \quad \dot{m}_{ce} \triangleq \dot{m}_{ce\,min} \ (if \ H = 0) \quad (2.13)$$

where ΔT is the boundary layer about the desired engine temperature, $T_{ed}(t)$. The boundary layer was introduced to reduce valve dithering. The proposed three–way valve operation ensures minimizing the warm–up and heating time during any operating condition (Mitchell et al., 2007).

Based on equations (2.10) and (2.11), the control objective described in equation (2.7) can be accomplished by designing the control laws $u_e(t)$ and $u_t(t)$ introduced in equation (2.9) as

$$u_e = -(k_e + \alpha_e)[\eta_e - \eta_{eo}] - \int_{t_o}^{t} \left[\alpha_e (k_e + \alpha_e) \eta_e(\tau) + \rho_e \, \text{sgn}(\eta_e(\tau))\right] d\tau \quad (2.14)$$

$$u_t = -(k_t + \alpha_t)[\eta_t - \eta_{to}] - \int_{t_o}^{t} \left[\alpha_t (k_t + \alpha_t) \eta_t(\tau) + \rho_t \, \text{sgn}(\eta_t(\tau))\right] d\tau \quad (2.15)$$

where k_e and k_t are real positive control gains, and the signals η_{eo} and η_{to} are the signals $\eta_e(t)$ and $\eta_t(t)$ evaluated at the initial time t_o. The last terms, $\rho_e \, \text{sgn}(\eta_e)$ and $\rho_t \, \text{sgn}(\eta_t)$, in equations (2.14) and (2.15) compensate for the variable unmeasurable quantities, $Q_e(t)$, and $Q_t(t)$. Refer to Setlur *et al.* (2005) for more details on this robust control design method and Lyapunov–based stability analysis. Knowledge of $u_e(t)$ and

$u_t(t)$, based on equations (2.14) and (2.15), allows the commutation relationships of equation (2.12) to be calculated which provides $\dot{m}_{cr}(t), \dot{m}_o(t)$, and $\dot{m}_{ar}(t)$. Finally, the voltage signals for the pumps and fan are prescribed using $\dot{m}_{cr}(t), \dot{m}_o(t)$, $\dot{m}_a(t)$ and *a priori* empirical relationships.

<u>Multi–Loop Thermal Test Bench and Test Profiles</u>

An experimental test bench was created to investigate advanced vehicle thermal management systems for multiple cooling loops. The test environment offers a safe and repeatable method to study the engine and transmission cooling loops. To rapidly heat fluids in the engine and transmission, a two–pass shell multiple output steam–based heat exchanger was utilized as shown in Figure 2.2. High pressure steam from Clemson University facilities has been integrated into the bench. For the engine loop, heated coolant is routed through a 6.0L International V–8 diesel engine block to emulate combustion. The engine block acts as a thermal capacitance similar to actual operation. From the engine block, the coolant flows to a three–way smart valve and then through the bypass and/or radiator before closing the loop with the coolant pump. In the transmission loop, steam is routed directly to the automatic transmission pan. The transmission fluid in the pan is rapidly heated and then circulated via an electric pump through the radiator's transmission cooling tank.
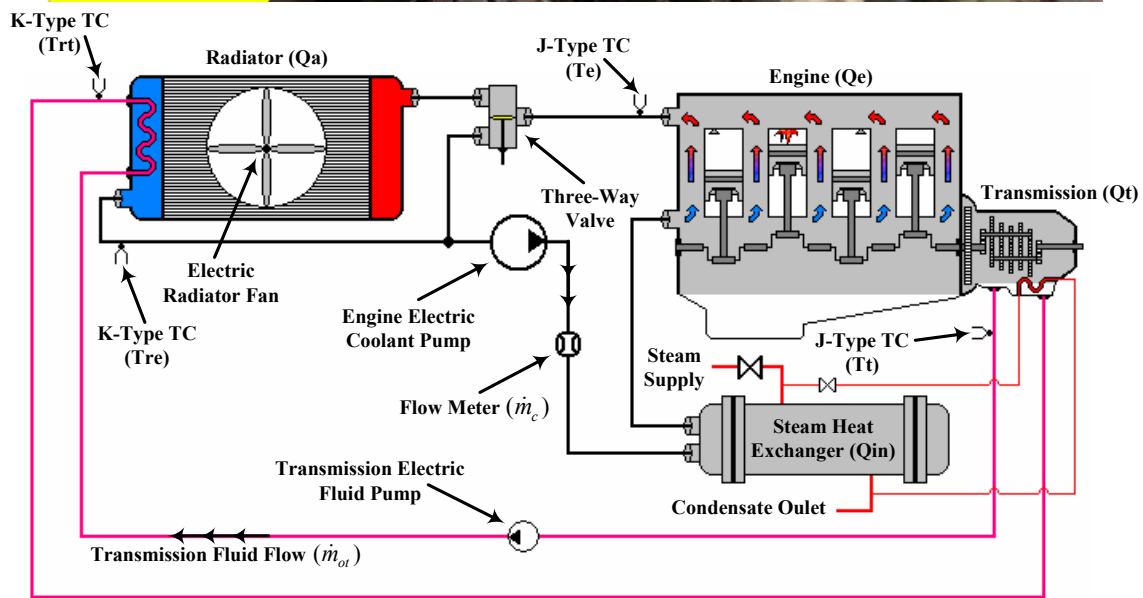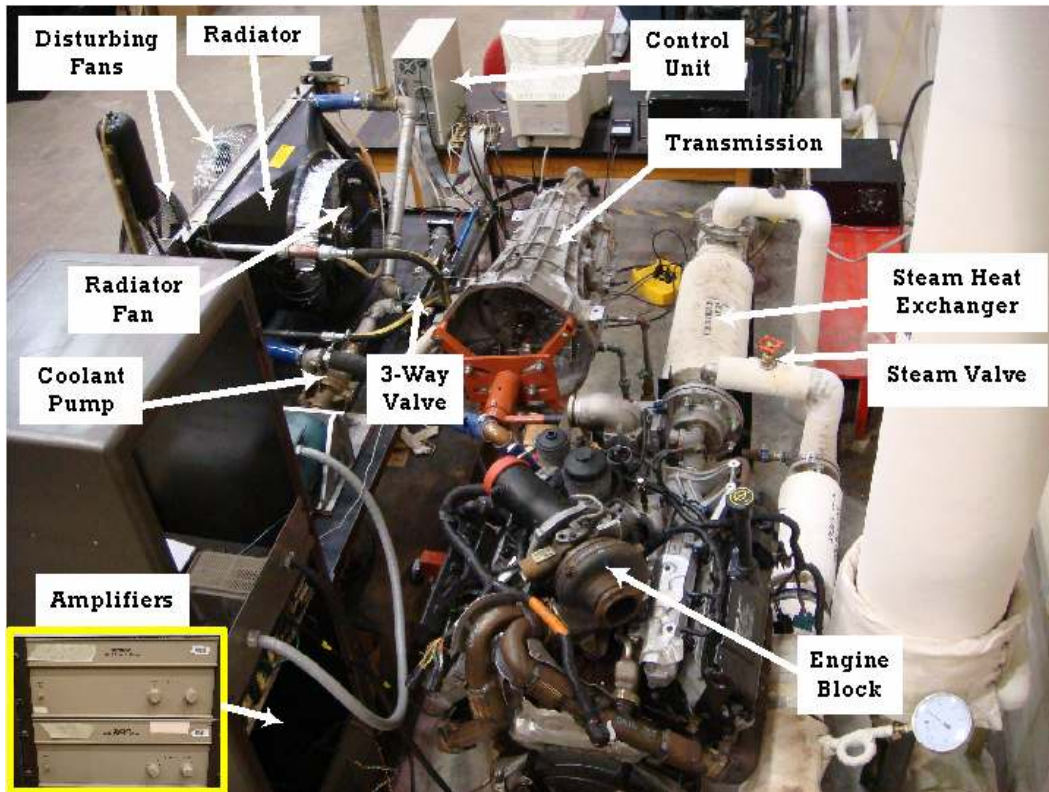
Figure 2.2 Experimental thermal test bench (schematic and actual) that features a 6.0L diesel engine block, transmission, three–way smart valve, electric coolant pump, electric fluid pump, electric radiator fan, radiator, and multiple output steam–based heat exchanger

The heat applied to the engine block and transmission housing may be independently adjusted by two steam control valves. Due to steam routing, a direct correlation exists between the heat introduced in the main engine loop and secondary heat transferred to the transmission (*i.e.*, the transmission connects to the heat exchanger). To calculate the rate of system heat transfer, $Q_{in} = Q_e + Q_t$, condensed steam was collected and weighed from both the transmission and main steam line. It has been assumed that the amount of condenser condensate is proportional to the amount of heat transferred to the circulating coolant (Incropera and DeWitt, 2002). Overall, heat transfer rates exceeding 60kW can be achieved with the current steam heat exchanger and transmission circuit.

The system sensors include three J–type thermocouples (T_e = engine coolant outlet, T_t = transmission fluid outlet, T_∞ = ambient air), two K–type thermocouples (T_{re} = radiator coolant outlet, T_{rt} = radiator fluid inlet), and main coolant mass flow meter, $\dot{m}_c$. The transmission fluid and radiator air mass flow rates are determined using empirical models. Data acquisition was performed by a Servo–to–Go board which utilizes eight analog–to–digital inputs and eight digital–to–analog outputs. This board provides control signals for the smart valve, engine and transmission variable speed electric pumps, and variable speed radiator fan. Due to equipment limitation, the charged–air–cooler has not been experimentally studied.

Five tests have been implemented to investigate the multi–loop system dynamics and controller's performance on the experimental test bench as shown in Table 2.1. The

first test applies a constant input heat, Q_{in}=35kW, and ram air disturbance, to emulate a vehicle traveling at V_{ram}=75km/h, with an ambient temperature of 294ºK (69.5ºF or 20.9ºC). The desired engine and transmission temperatures were T_{ed}=362ºK and T_{td}=358ºK. For the second test, an elevated temperature of 325ºK (125.3ºF or 51.9ºC) was applied while maintaining the same input heat and ram air disturbance as test one. The elevated temperature testing allowed significant thermal loading which may be found in desert climates around the world. In the third test, the desired engine and transmission temperatures were $T_{ed} = 363 + \text{sgn}\left[\sin\left(0.002\pi t - \pi\right)\right]$ and T_{td}=356ºK. A constant input heat, Q_{in}=39kW, and ram air disturbance, to emulate a vehicle traveling again at 75km/h, were applied with an ambient temperature of 292ºK. The fourth test varies both the total input heat, $Q_{in} = Q_e + Q_t$, and the ram air disturbance, V_{ram}, as shown in Figure 2.3 with an ambient temperature of 300ºK. The desired engine and transmission temperatures were set as T_{ed}=364ºK and T_{td}=362ºK. Finally, a fifth test was conducted to evaluate two alternative controllers that were designed for their overall performance when compared to the nonlinear robust controller.
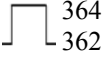
Test No.	Test Description	T_∞ [ºK]	T_{ed} [ºK]	T_{td} [ºK]	Q_{in} [kW]	V_{ram} [km/h]
1	Steady heat and ram air disturbance	294	362	358	35	75
2		325				
3	Square wave set point temperature	292	364 362	356	39	75
4	Variable heat and ram air disturbance	300	364	362	20–50	0–100
5	Comparison of controllers design	294	362	356	45	75

Table 2.1 Test profiles for the multi–loop thermal system

Experimental Results

In this section, representative experimental results will be presented to investigate the proficiency of the real–time control algorithm and servo–motor driven actuators in regulating set point temperatures and minimizing power consumption in multi–loop automotive cooling systems. A set of five experimental tests (refer to Table 2.1) have been conducted on the steam–based multi–loop thermal test bench which features the engine and transmission cooling loops. The thermal model parameter values are ε_r=0.6, c_{pa}=1.012kJ/kg.°K, c_{pc}=4.181kJ/kg.°K, and $c_{po} = c_{pc}$. Note that coolant has been substituted for the transmission oil. The thermostat valve operated ΔT=3°K below the set point temperature, $T_{ed}(t)$, (Mitchell $et\ al.$, 2007). The controller gains and parameters were k_e=15, α_e=0.001, ρ_e=5, k_t=3, α_t=0.0001, ρ_t=0.001, ε=0.01, $\dot{m}_{ce\,min}$=0.6kg/sec (through the radiator branch only), and $\dot{m}_{ot\,min}$=0.05kg/sec for all the test profiles presented in Table 2.1.
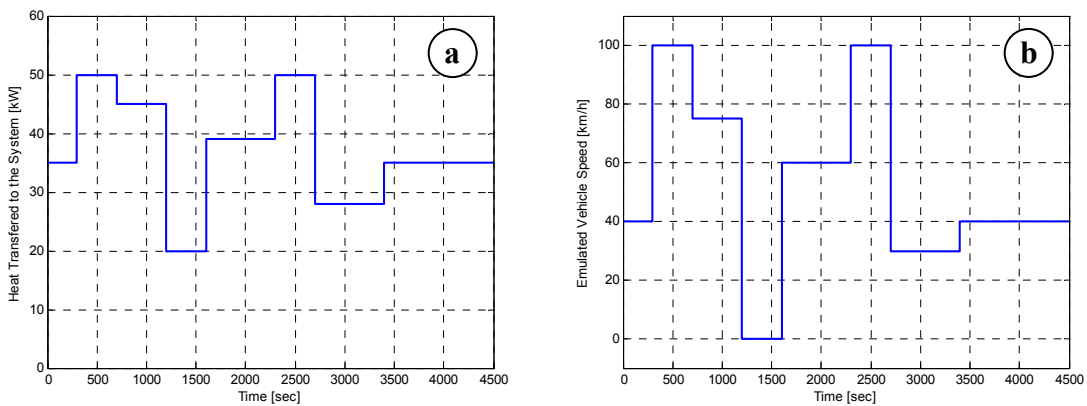
Figure 2.3 Experimental (a) input heat profile, $Q_{in}(t)$, and (b) ram air disturbance, $V_{ram}(t)$, to emulate different vehicle speeds for the fourth test

Robust Controller Applied to Four Operating Scenarios

In the first test, vehicle highway operation was emulated using a constant heat of Q_{in} =35kW, ram air of V_{ram} =75km/h, and a normal ambient temperature of 294ºK. As shown in Figures 2.4a and 2.4b, the engine and transmission are somewhat overcooled since their two fluid temperatures slowly approach their set point values. The fluid flow through the engine and transmission remain a minimum per Figures 2.4c and 2.4d. The radiator fan was shut off for the entire test period (refer to Figure 2.4e) while the thermostat valve effort (refer to Figure 2.4f) was initially oscillatory and then settled to full radiator flow (remember that thermostat valve operation per Remark 2.3 is either fully open or fully closed).

In the second test, an elevated temperature of 325ºK (125.3ºF or 51.9ºC) was achieved using a 165kBtu/h portable kerosene forced–air heater as shown in Figure 2.5. The temperature tracking errors for the engine and transmission were 3ºK and 5ºK, respectively, as shown in Figures 2.6a and 2.6b. The system actuators (*i.e.*, pumps and fan) were saturated (refer to Figures 2.6c, 2.6d, and 2.6e) and not able to readily reject the system heat. The fan effort increases with the elevated temperature. This is clear from the fan commutation strategy introduced in equation (2.12) where $\dot{m}_{ar}(t)$ is affected by the difference $T_e(t) - T_\infty(t)$. The thermostat valve in Figure 6f was wide open after t =185sec. The elevated temperature demonstrated the need for a larger radiator size based on the thermal loads. This test clearly illustrates the requirement for cooling system sizing to meet environmental demands.

Figure 2.4 First experimental test scenario for the robust controller with emulated vehicle speed of 75km/h, Q_{in}=35kW, and normal ambient temperature of T_∞=294ºK; (a) Engine and radiator temperatures with a desired engine temperature of T_{ed}=362ºK; (b) Transmission and radiator side tank temperatures with a desired transmission temperature of T_{td}=358ºK; (c) Coolant mass flow rate through the engine pump; (d) Coolant mass flow rate through the transmission pump; (e) Air mass flow rate through the radiator fan; and (f) Normalized thermostat valve position
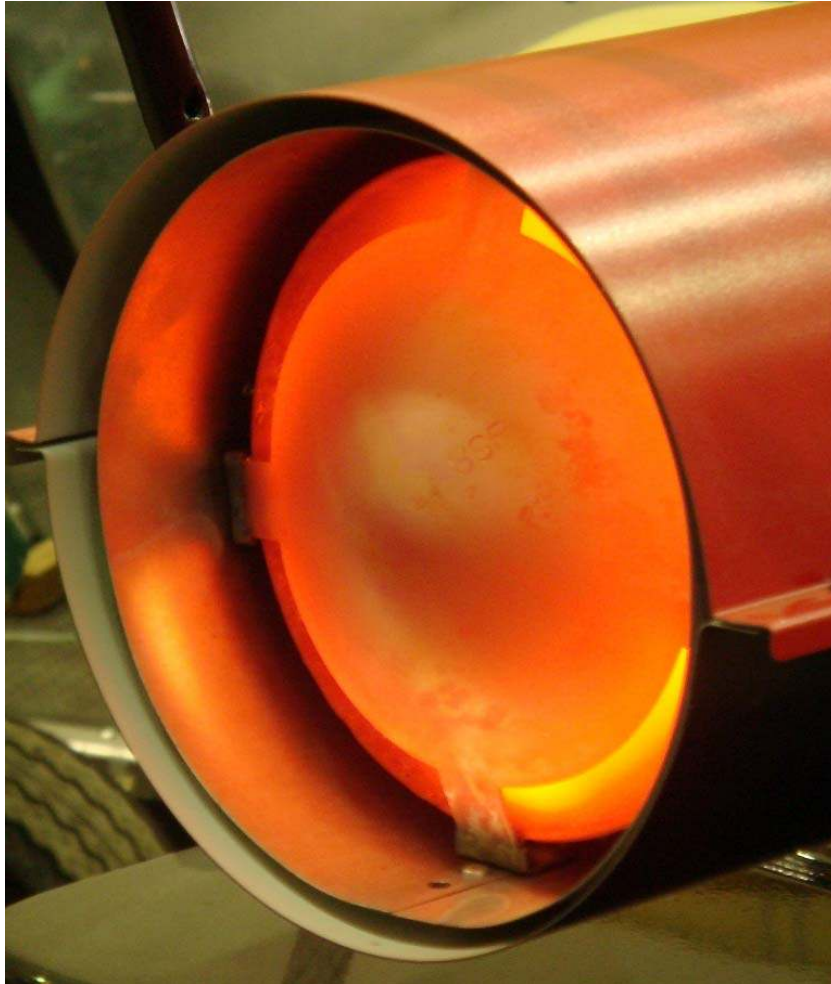
Figure 2.5 Portable kerosene forced–air heater exhaust stream used to elevate the ambient air temperature entering the cooling system for test two which challenged the cooling system's heat rejection capabilities

Remark 2.4: *It was observed that allowing the coolant flow in the engine loop to exceed selected thresholds would violate Assumption 2.3 since the radiator temperature would be greater than the engine temperature. This condition arises due to the lack of heat rejection at the radiator. The violated assumption (and based on the commutation strategy described in equation (2.12)) required the pump speed to oscillate continuously. To improve the thermal response under this condition, the maximum engine pump coolant mass flow rate was limited to 1.25kg/sec so the coolant through the radiate is given more time to cool down.*

The third test emulated a vehicle operating at a variable engine set point

temperature to illustrate different combustion temperature cooling demands (*e.g.*, perhaps

due to different fuel types). The engine and transmission temperatures response is shown in Figures 2.7a and 2.7b. The engine's coolant pump behavior (refer to Figure 2.7c) is affected by the radiator temperature since it depends on the difference between the engine and radiator temperatures as stated in Remark 2.2. The transmission pump operates at its maximum capacity in Figure 2.7c since the transmission temperature remains above the set point, T_{td}=356ºK. In Figure 2.7e, the fan's response is impacted by the engine temperature tracking error. Finally, temperature tracking errors of 0.1ºK and 0.8ºK were realized for the engine and transmission as shown in Figure 2.7f. The spikes in the engine temperature tracking error are due to the instant change in the desired engine temperature set point. Each time the engine temperature set point changes its magnitude, a spike occurs which is also evident in the fan response of Figure 2.7e.

Finally, a "driving" cycle was introduced in test four (refer to Figure 2.3) which features variable heat and ram air inputs. Although this test does not correspond to an established drive cycle, it attempts to demonstrate the cooling system's response to variable heat and ram air loads for mixed–mode vehicle operation. In Figure 2.8, the complete experimental results are displayed for a normal ambient temperature of T_∞=300ºK. The proposed controller and operation strategies satisfactorily regulate the temperatures per Figures 2.8a and 2.8b as evident by the maximum engine and transmission temperature tracking errors of 1.8ºK and 2.0ºK for a 50kW load and 100km/h vehicle speed (refer to Figure 8c). Finally, Figures 8d–f show the transient response of the transmission pump, engine coolant pump, and radiator fan which are well behaved.
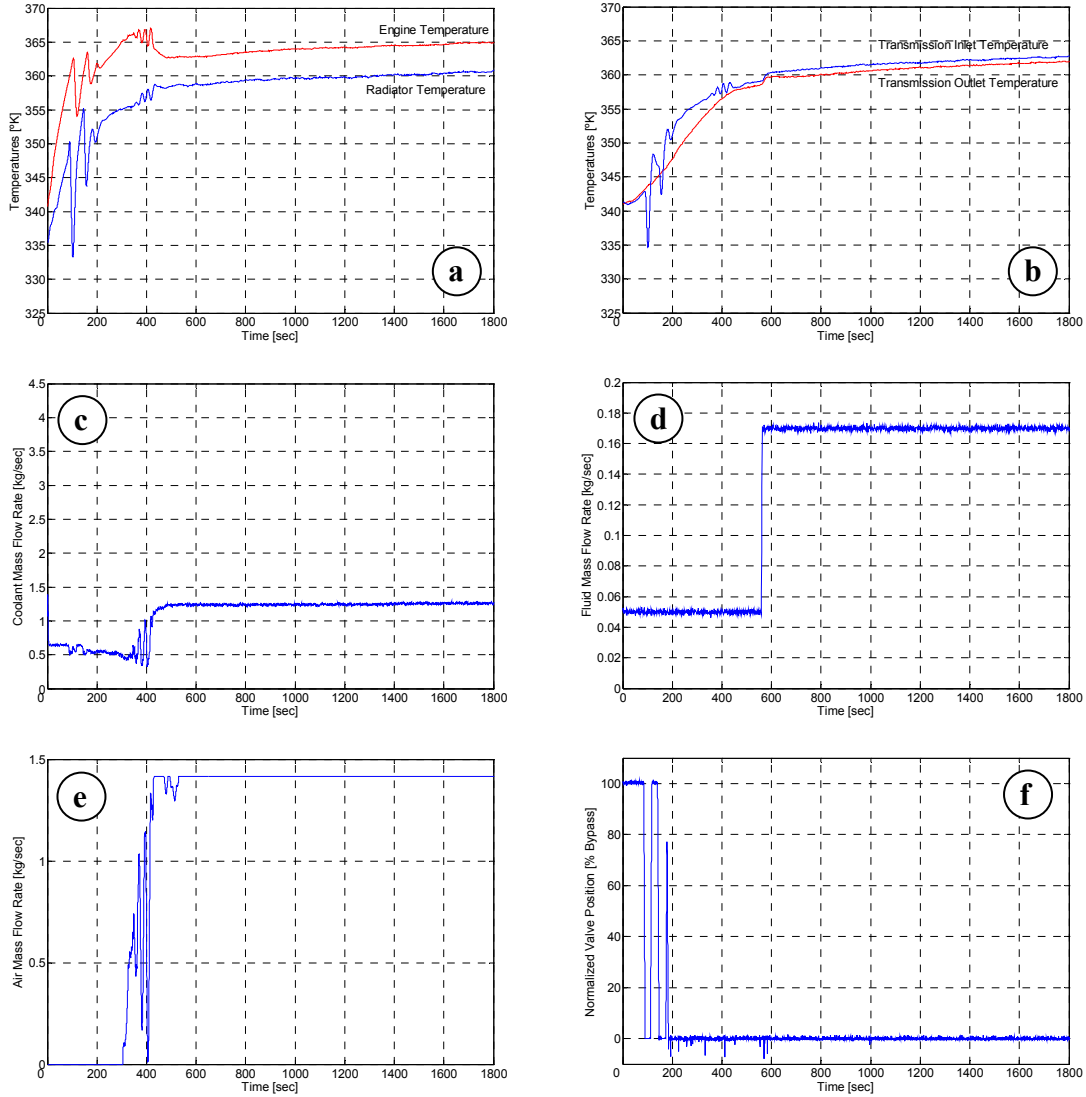
Figure 2.6 Second experimental test scenario for the robust controller with emulated vehicle speed of 75km/h, Q_{in}=35kW, and elevated ambient temperature of T_∞=325ºK; (a) Engine and radiator temperatures with a desired engine temperature of T_{ed}=362ºK; (b) Transmission and radiator side tank temperatures with a desired transmission temperature of T_{td}=358ºK; (c) Coolant mass flow rate through the engine pump; (d) Coolant mass flow rate through the transmission pump; (e) Air mass flow rate through the radiator fan; and (f) Normalized thermostat valve position
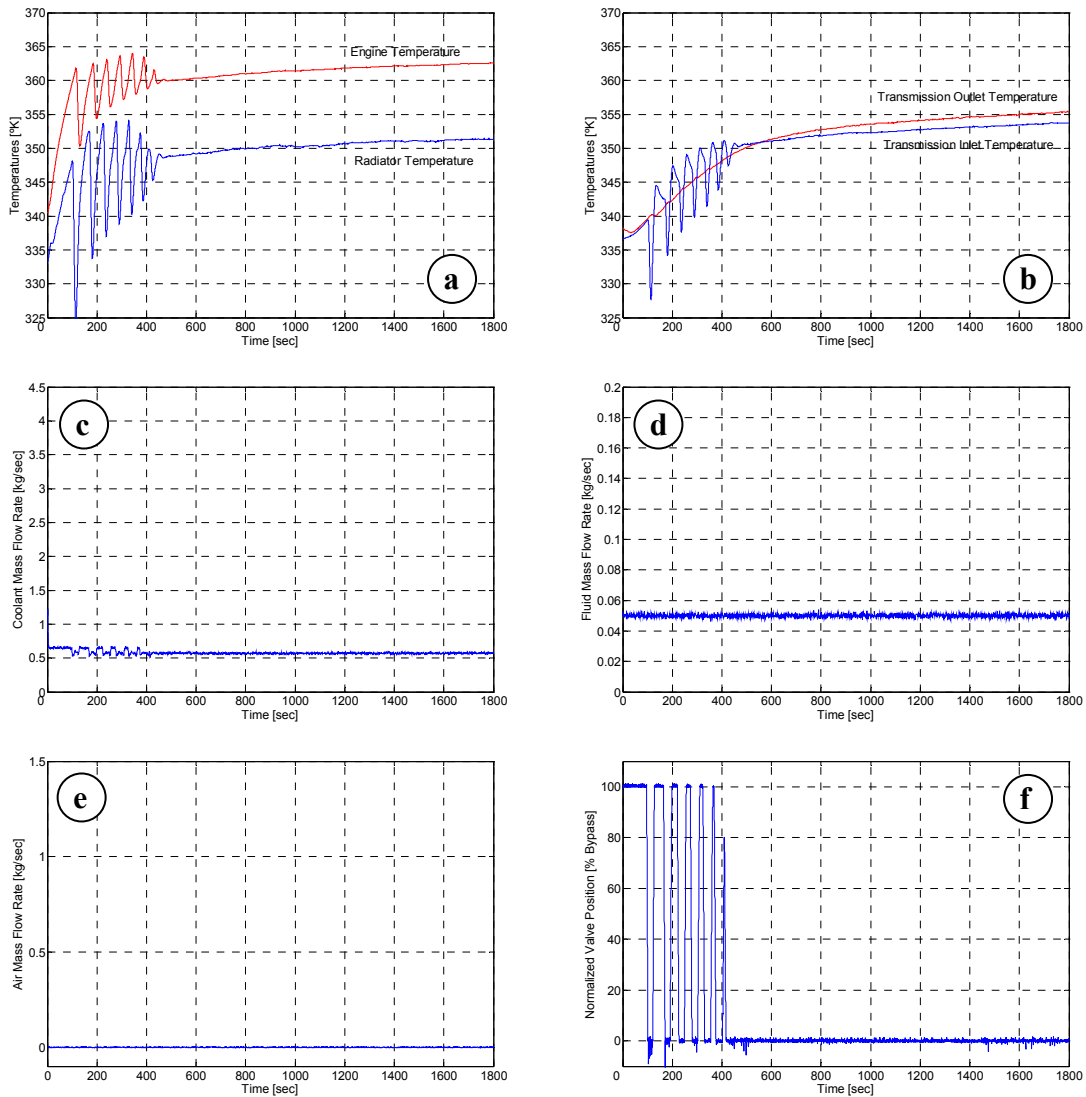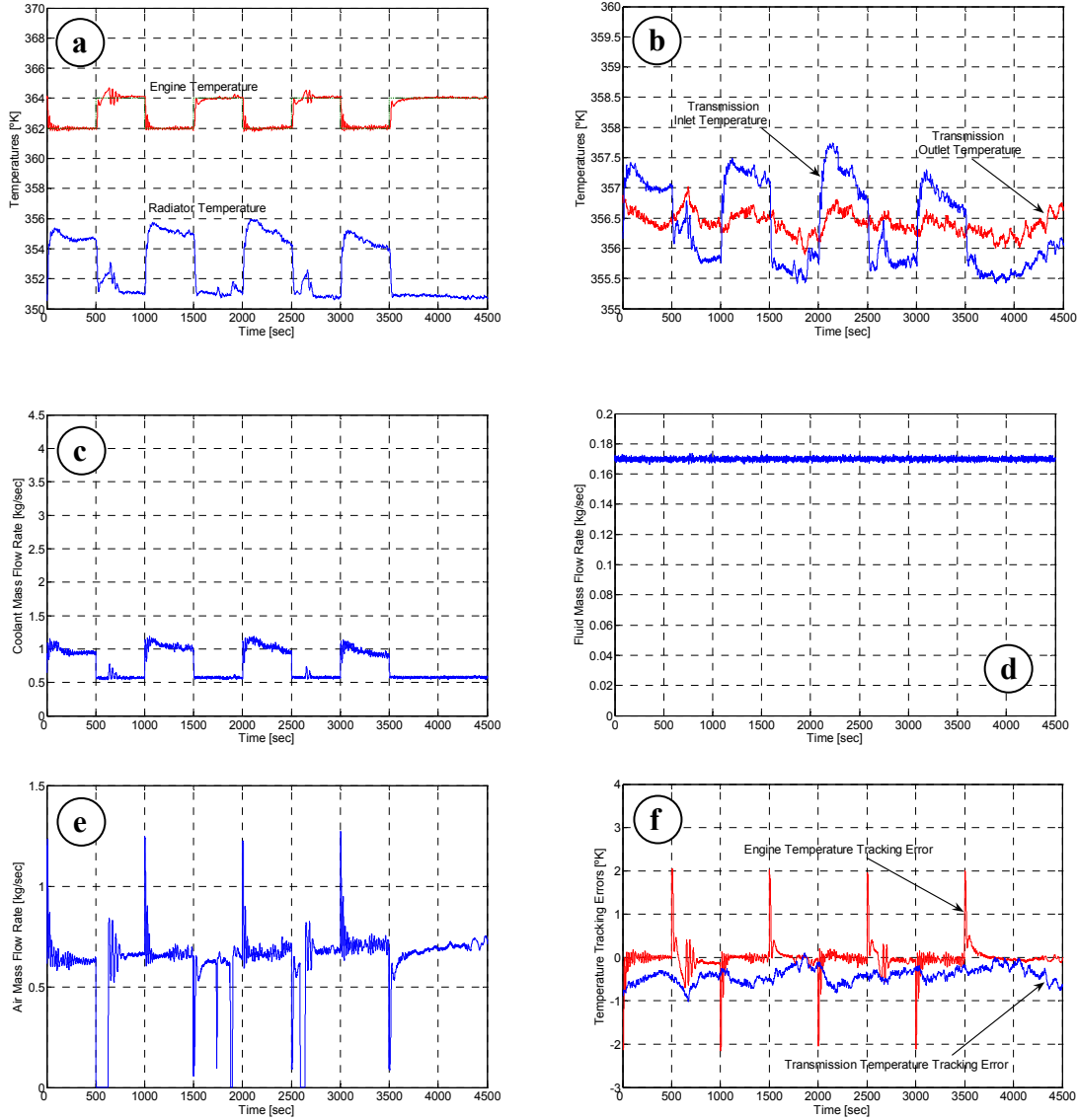
Figure 2.7 Third experimental test scenario for the robust controller with emulated vehicle speed of 75km/h, Q_{in} =39kW, and normal ambient temperature of T_∞ =292ºK; (a) Engine and radiator temperatures with a square wave desired engine temperature; (b) Transmission and radiator side tank temperatures with a desired transmission temperature of T_{td} =356ºK; (c) Coolant mass flow rate through the engine pump; (d) Coolant mass flow rate through the transmission pump; (e) Air mass flow rate through the radiator fan; and (f) Engine and transmission temperature error
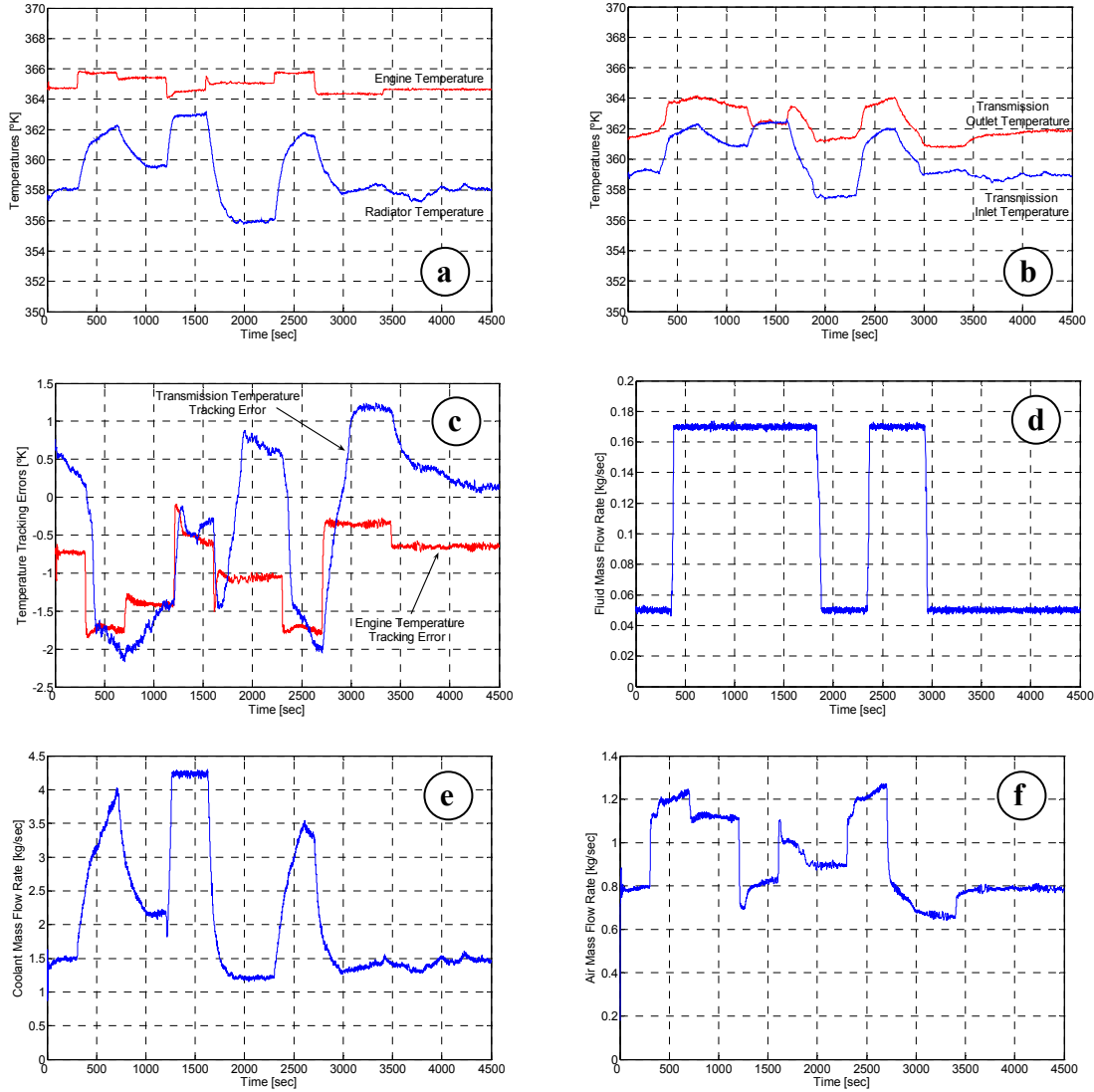
Figure 2.8 Fourth experimental test scenario for the robust controller where the input heat and ram air disturbance vary with time and the ambient temperature $T_\infty = 295\text{°K}$; (a) Engine and radiator temperatures with a desired engine temperature of $T_{ed} = 364\text{°K}$; (b) Transmission outlet and inlet temperatures with a desired transmission temperature of $T_{td} = 362\text{°K}$; (c) Engine and transmission temperature tracking errors; (d) Fluid mass flow rate through the transmission pump; (e) Coolant mass flow rate through the engine pump; and (f) Air mass flow rate through the radiator fan

<u>Comparison of Three Controllers for Steady Heating and Ram Air Disturbance</u>

For completeness, a comparison of three different control strategies was investigated for test five. The ambient temperature, T_∞=294ºK, and system initial conditions were maintained for each controller study. A constant input heat, Q_{in}=45kW, and a ram air disturbance, V_{ram}=75km/h, were uniformly applied. The desired engine and transmission temperatures were T_{ed}=362ºK and T_{td}=356ºK. In Table 2.2, the proposed robust controller is compared with a traditional factory thermostat valve operation and proportional integral (PI) control strategy. The traditional factory operation strategy (Mitchell *et al.*, 2007) describes the wax–based thermostat valve dynamics (with mixing opportunities) as

$$H = \begin{cases} 0, & T_e < T_L & (\textit{bypass only}) \\ \dfrac{T_e - T_L}{T_H - T_L}, & T_L \le T_e \le T_H & (\textit{mixing}) \\ 1, & T_e > T_H & (\textit{radiator only}) \end{cases} \qquad (2.16)$$

For the second operation strategy, two PI controllers were implemented (*i.e.*, engine loop and transmission loop) such that the control efforts (voltages) for the coolant pump, radiator fan, and fluid pump becomes $V_{ep} = 0.7\left(K_{Pe}\eta_e + K_{Ie}\int \eta_e(\tau)d\tau\right)$, $V_{rf} = 0.3\left(K_{Pe}\eta_e + K_{Ie}\int \eta_e(\tau)d\tau\right)$, and $V_{pt} = K_{Pt}\eta_t + K_{It}\int \eta_t(\tau)d\tau$.

The performance of the three control methods has been evaluated in terms of temperature tracking error and power consumption. The system power, $p_{sys}\left(\dot{m}_{ce}, \dot{m}_{ot}, \dot{m}_{ar}\right)$, measures the average power consumed by the system actuators over the time period T=25min. The power measure was performed for the duration of the

48

experimental test using empirical relationships for the flow rate measurements and electrical input power. The power consumed by the smart valve is considered to be quite small so it is neglected in the calculation. Overall, the proposed robust control strategy was ranked first among the controllers (and operation strategies). The robust controller achieved a steady–state absolute value engine and transmission temperature tracking error of η_{ess}=0.13ºK and η_{tss}=0.65ºK, respectively, with a system power consumption of P_{sys}=19.82W per Table 2.2. In this operation strategy, the controller was designed for the coupled engine and transmission loops to harmoniously operate the cooling system actuators in an efficient manner to obtain desired thermal condition.

On the contrary, the PI controller regulated the engine coolant and transmission fluid temperatures separately. The radiator fan was operated to only dissipate and reject the heat generated by the engine coolant regardless of the heat generated in the transmission housing. This approach offers steady–state absolute temperature tracking errors of η_{ess}=0.12ºK and η_{tss}=2.35ºK with a system power consumption of P_{sys}=48.14W. The traditional factory operation strategy relies on the wax–based thermostat valve to regulate only the engine coolant temperature, $T_e(t)$, regardless of the transmission temperature, $T_t(t)$. During the test, large oscillations were observed in the coolant temperature magnitude due to the repeatable opening and closing of the wax–based thermostat valve. As shown in Table 2, the reported steady–state absolute engine temperature tracking error was η_{ess}=2.00ºK. The transmission temperature is not actively controlled in most factory configurations. Further, the system power consumption was

the maximum compared to the other control methods due to the operating speeds of the engine coolant pump and radiator fan.

Operation Strategies Description	$|\eta_{ess}|$ [ºK]	$|\eta_{tss}|$ [ºK]	P_{sys} [W]	Rank
Robust Controller	0.13	0.65	19.82	1
PI Controller	0.12	2.35	48.14	2
Traditional Factory Control Method	2.00	N/A	257.28	3

Table 2.2 Experimental summary of three cooling system control strategies for an engine and a transmission configuration with steady heat and ram air disturbance (Test 5). For the traditional factory operation strategy, the temperature bounds are T_L =359ºK and T_H =365ºK. For the second operation strategy, two PI controllers were implemented (*i.e.*, one for the engine loop and the other for the transmission loop). The controller's gains for the engine loop were set as K_{Pe} =0.5 and K_{Ie} =0.01 with 70% and 30% control effort for the engine pump and radiator fan, respectively. The controller's gains for the transmission loop were set as K_{Pt} =3 and K_{It} =0.001

Concluded Remarks

An advanced automotive thermal management systems can positively influence the coolant temperature regulation and associated power consumption. In this paper, a multiple loop servo–motor based smart cooling system has been experimentally assembled and controlled utilizing a Lyapunov–based nonlinear controller. The proposed control strategy successfully maintained the engine coolant and transmission fluid temperatures to user–defined setpoint values with small error percentages. Further, the power consumed by the cooling system actuators was reduced through the synchronous control of the pumps and fan motors. The occurrence of elevated ambient temperatures required the cooling components to operate at maximum speeds for heat dissipation which increased power consumption. Overall, the research findings demonstrated that setpoint temperatures can often be maintained while minimizing power consumption which should assist in the quest for greater vehicle fuel economy.

CHAPTER 3
HYDRAULIC ACTUATED AUTOMOTIVE COOLING SYSTEMS – NONLINEAR CONTROL AND TEST

Introduction

Traditionally, automotive cooling systems have relied on a mechanically–driven coolant pump and radiator fan (*i.e.*, the coolant pump is a simple centrifugal pump driven by a belt connected to the crankshaft of the engine, and the fan is attached either directly to the engines crankshaft or is coupled to the crankshaft through a belt and pulley). However, having the coolant pump and radiator fan dependent on the engine speed causes the engine system to overheat and/or overcooled, thus, wasting power, decreasing fuel efficiency, and increasing pollution (Wambsganss, 1999).

Recently, the attention has been oriented towards using computer controlled electric servo–motors to drive the cooling system components to overcome the existing problems in the traditional cooling systems, and they have proven their capability to improve the internal combustion engines thermal conditions (Allen and Lasecki, 2001). Nowadays, researchers have been investigating the possibilities of utilizing hydraulic–driven motors to power the variable speed cooling components (*e.g.*, coolant pump and radiator fan) due to their additional advantages over the electric counterparts. For larger engine sizes (*e.g.*, buses and heavy duty trucks), the power requirements for the coolant pump and radiator fan increase. For the electric motors to meet these requirements, they are required to be quite large and heavy. In addition, the electric–driven components produce more heat in comparison with the hydraulic motors, which produce large

51

amounts of power in a small and compact package. Thus, hydraulic–driven pumps and fans are more practical and efficient for increased cooling demands (Dostal, 1994).

For an efficient automotive hydraulic–based thermal management system, the thermal cooling loop along with the hydraulic–driven components have to be modeled in order to develop an effective control algorithm. Henry *et al.* (2001) developed and validated an automotive powertrain cooling system simulation model against test results, which featured basic system components, for a pick up truck applications. Vaughan and Gamble (1996) developed a nonlinear dynamic simulation model for a high speed direct acting solenoid valve. The model accurately predicted both the dynamic and steady–state response of the valve to voltage inputs. Finally, Frick *et al.* (2006) presented a series of mathematical models to describe the dynamic behavior of a hydraulic system. They showed in simulation that these models are capable of predicting transient responses of a hydraulic valve and motor.

Different control architectures and operating strategies have been developed to control the thermal management system components (such as Setler *et al.*, 2005), and to operate hydraulic–driven actuators (such as Chiang *et al.*, 2005). Hamamoto *et al.* (1990) developed electronically controlled hydraulic cooling fan system to generate high airflow and get the optimum fan speed at all engine running conditions. Chen *et al.* (2002) developed a nonlinear backstepping exponential tracking controller for a hydraulic cylinder and proportional directional control valve to precisely positioning a mechanical load and accommodate inherent system nonlinearities. Kaddissi *et al.* (2007) proposed a nonlinear backstepping approach for the position control of an electrohydraulic servo

system. They compared the experimental results to those obtained with a real time proportional–integral–derivative (PID) controller and proved the effectiveness of the developed control algorithm in position tracking.

In this chapter, a nonlinear backstepping robust controller is developed and formulated to control and regulate the temperature of a thermal system that features hydraulic–driven actuators. The proposed control strategy was selected due to the nonlinear mathematical formulation of the hydraulic thermal system and to accommodate disturbances and uncertainties. Further, this robust controller has been verified by simulation techniques and validated by experimental testing. In Section 3.2, mathematical models are presented to describe the dynamic behavior of the automotive hydraulic–based thermal management system and hydraulic cooling components. A nonlinear backstepping robust tracking control strategy is introduced in Section 3.3. Section 3.4 presents the experimental hydraulic–based thermal test bench, while Sections 3.5 and 3.6 introduce numerical and experimental results, respectively. The concluded remarks are contained in Section 3.7.

<u>Mathematical Models</u>

A suite of mathematical models describes the transient response of the hydraulic–based advance thermal management system and the hydraulic–driven actuators. The system components include six immersion electrical heaters to heat the coolant, a variable speed hydraulically–driven coolant pump, a radiator with a variable speed hydraulically–driven fan, and two servo–solenoid hydraulic control valves to operate the pump and fan motors.

53

<u>Automotive Engine and Radiator Thermal Dynamics</u>

The cooling system's dynamic behavior may be represented by a reduced order two–node lumped parameter thermal model (refer to Figure 3.1) to minimize the computational burden for in–vehicle implementation. The engine and radiator temperature dynamic behaviors (Salah *et al.*, 2008) may be expressed as

$$C_e \dot{T}_e = Q_{in} - c_{pc} \dot{m}_c \left(T_e - T_r \right) \tag{3.1}$$

$$C_r \dot{T}_r = -Q_o + c_{pc} \dot{m}_c \left(T_e - T_r \right) - \varepsilon \, c_{pa} \dot{m}_a \left(T_e - T_\infty \right). \tag{3.2}$$

The variables $Q_{in}(t)$ and $Q_o(t)$ represent the input heat generated during the combustion process and the radiator heat loss due to uncontrollable air flow, respectively.
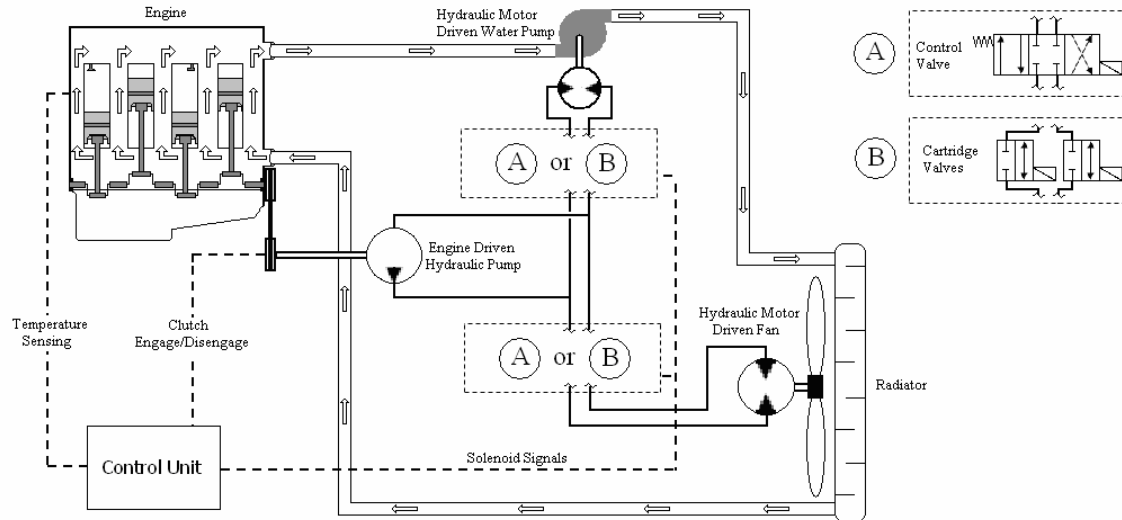
Figure 3.1 An automotive hydraulic actuated advanced cooling system featuring a variable speed hydraulic–driven coolant pump, radiator with a variable speed hydraulic–driven radiator fan, control valves, and sensors (temperature, flow rate, and pressure)

<u>Hydraulic–Driven Coolant Pump and Radiator Fan Dynamics</u>

Two servo–solenoid hydraulic valves (refer to Figure 3.2) operate the coolant pump and radiator fan gear motors. The control voltage, $V(t)$, applied to the solenoid

coil generates a mechanical force which displaces the internal spool to allow fluid flow. For this study, the solenoid current, $i(t)$, and force, $F_s(t)$, are governed by (Vaughan and Gamble, 1996)

$$\frac{di}{dt} = \frac{1}{L}(V - iR), \quad F_s = \left(\frac{N_t^2 a \mu_o}{4 l_g}\right) i^2 .$$

(3.3)

The magnitude of the transient and steady state forces on the valve spool can be described as

$$F_{tr}^{1,2} = \left[L_d C_d w \sqrt{2\rho(P_{SB} - P_{AT})}\right] \dot{x}, \quad F_{ss}^{1,2} = \left[2 C_d w \cos(\theta)(P_{SB} - P_{AT})\right] x$$

(3.4)

where P_{SB} is either the supply pressure, P_S, or the hydraulic motor return pressure, P_B, and P_{AT} is either the hydraulic motor supply pressure, P_A, or the tank pressure, P_T, as shown in Figure 3.2. Newton's law may be applied to the spool valve to determine the spool displacement so that

$$\ddot{x} = \frac{1}{m_s}\left[F_s + (F_{ss2} - F_{ss1}) + (F_{tr2} - F_{tr1}) - k_{val}x - b_{val}\dot{x}\right].$$

(3.5)
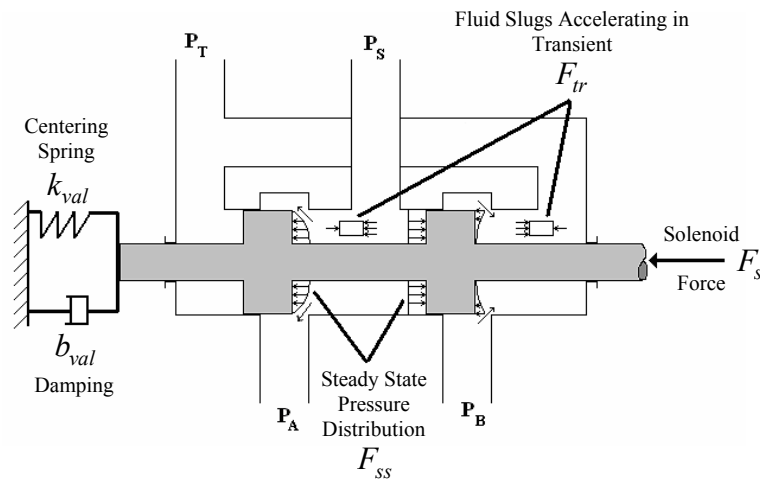
Figure 3.2 A servo–solenoid hydraulic control valve schematic showing two inlets and two outlets with corresponding acting forces

The valve's position, $x(t)$, determines the load flow, $Q_L(t)$, applied to the hydraulic motor and the corresponding load pressure, $P_L(t)$, (Merritt, 1967) such that

$$Q_L = D_m\omega + C_{im}P_L + \frac{V_t}{2\beta}\dot{P}_L = \left(C_dw\sqrt{\frac{(P_S - P_L)}{\rho}}\right)x \qquad (3.6)$$

$$\dot{P}_L = \left(\frac{2\beta C_dw}{V_t}\sqrt{\frac{(P_S - P_L)}{\rho}}\right)x - \frac{2\beta C_{im}}{V_t}P_L - \frac{2\beta D_m}{V_t}\omega. \qquad (3.7)$$

Applying Newton's second law with the assumption of ideal hydraulic motor power transformation, the hydraulic motor shaft acceleration, $\dot{\omega}(t)$, is computed as

$$\dot{\omega} = \frac{1}{J}\left(T_g - B_m\omega - T_{Load}\right) \qquad (3.8)$$

where $T_g \triangleq D_mP_L$, $T_{Load} \triangleq f_L(\dot{m})$, and $\dot{m}(t)$ is the mass flow rate of liquid or air. To facilitate the control design for the internal spool displacement, $x(t)$, an expression for $\omega(t)$ can be obtained from equation (3.7) and then substituted into equation (3.8) to realize

$$\dot{\omega} = \left(\frac{D_m^2 + B_mC_{im}}{JD_m}\right)P_L + \left(\frac{B_mV_t}{2JD_m\beta}\right)\dot{P}_L - \left(\frac{B_m}{JD_m}C_dw\sqrt{\frac{P_S - P_L}{\rho}}\right)x - \frac{T_{Load}}{J}. \qquad (3.9)$$

Hydraulic Controller Design

A Lyapunov–based nonlinear control algorithm is developed to regulate the coolant temperature and maintain the system in a desirable thermal condition. The controller's main objective is to precisely track the temperature set point, $T_{ed}(t)$, while compensating for system uncertainties (*i.e.*, combustion process input heat, $Q_{in}(t)$,

radiator heat loss, $Q_o(t)$, pump hydraulic motor load, $T_{Lp}(t)$, fan hydraulic motor load, $T_{Lf}(t)$, hydraulic pump load pressure variations, $\dot{P}_{Lp}(t)$, and hydraulic fan load pressure variations, $\dot{P}_{Lf}(t)$) by harmoniously controlling the system hydraulic–driven actuators. Referring to Figure 1, the system servo–actuators are two servo–solenoid control valves, a hydraulic–driven coolant pump, and radiator fan. For equations (3.1), (3.2), and (3.9), the signals $T_e(t)$, $T_r(t)$ and $T_\infty(t)$ can be measured by either thermocouples or thermistors, the signal $\omega(t)$ can be measured by optical encoders, and the system parameters C_e, C_r, c_{pc}, c_{pa}, ε, J, B_m, D_m, C_{im}, V_t, C_d, w, β and ρ are assumed to be constant and fully known.

To facilitate the controller design process, four assumptions are imposed:

Assumption 3.1: *The signals $Q_{in}(t)$ and $Q_o(t)$ always remain positive in equations (3.1) and (3.2) (i.e., $Q_{in}(t), Q_o(t) \geq 0$). Further, the signals $Q_{in}(t)$ and $Q_o(t)$ remain bounded at all time, such that $Q_{in}(t), Q_o(t) \in L_\infty$.*

Assumption 3.2: *The surrounding ambient temperature $T_\infty(t)$ is uniform and satisfies $T_e(t) - T_\infty(t) \geq \varepsilon_1, \forall t \geq 0$ where $\varepsilon_1 \in \mathbb{R}^+$ is a constant.*

Assumption 3.3: *The heated coolant and radiator temperatures satisfy the condition $T_e(t) - T_r(t) \geq \varepsilon_2, \forall t \geq 0$ where $\varepsilon_2 \in \mathbb{R}^+$ is a constant. Further, $T_e(0) \geq T_r(0)$ to facilitate the boundedness of signal argument.*

Assumption 3.4: *The signals $T_L(t)$, $P_L(t)$, and $P_S(t)$ always remain positive in equation (9) (i.e., $T_L(t), P_L(t), P_S(t) \geq 0$ at all time) and $P_S(t) > P_L(t)$. Further, the signals $T_L(t)$, $P_L(t)$, and its first time derivative, $\dot{P}_L(t)$, remain bounded at all time, such that $T_L(t), P_L(t), \dot{P}_L(t) \in L_\infty$.*

Assumption 3.3 allows the heated coolant and radiator to initially be the same temperature (*e.g.*, cold start). The unlikely case of $T_e(0) < T_r(0)$ is not considered.

<u>Backstepping Robust Control Objective</u>

The control objective is to ensure that the actual temperatures of the engine coolant, $T_e(t)$, and the radiator, $T_r(t)$, track the desired trajectories $T_{ed}(t)$ and $T_{vr}(t)$, respectively, as well as the actual pump speed, $\omega_p(t)$, and fan speed, $\omega_f(t)$, to track the desired trajectories $\omega_{pd}(t)$ and $\omega_{fd}(t)$, respectively, in the following sense

$$\left|T_{ed}(t) - T_e(t)\right| \le \varepsilon_e, \ \left|T_r(t) - T_{vr}(t)\right| \le \varepsilon_r, \ \left|\omega_{pd}(t) - \omega_p(t)\right| \le \varepsilon_p, \ \left|\omega_{fd}(t) - \omega_f(t)\right| \le \varepsilon_f$$

$$\text{as } t \to \infty \tag{3.10}$$

while compensating for the system variable uncertainties $Q_{in}(t)$, $Q_o(t)$, $\dot{P}_{Lp}(t)$, $\dot{P}_{Lf}(t)$, $T_{Lp}(t)$, and $T_{Lf}(t)$ where ε_e, ε_r, ε_p, $\varepsilon_f \in \mathbb{R}^+$ are small constants. Again, to facilitate the controller design process, two more assumptions are imposed:

Assumption 3.5: *The engine temperature profiles are always bounded and chosen such that its first time derivative remains bounded at all times (i.e., $T_{ed}(t)$, $\dot{T}_{ed}(t) \in L_\infty$). Further, $T_{ed}(t) \gg T_\infty(t)$ at all times.*

Assumption 3.6: *The engine temperature profiles and radiator temperature satisfy the condition $T_{ed}(t) - T_r(t) \ge \varepsilon_3, \forall t \ge 0$ where $\varepsilon_3 \in \mathbb{R}^+$ is a constant. This assumption is needed to facilitate the boundedness argument in the control development.*

Remark 3.1: *Although it is unlikely that the desired radiator temperature setpoint, $T_{vr}(t)$, hydraulic coolant pump speed, $\omega_{pd}(t)$, and hydraulic radiator fan speed, $\omega_{fd}(t)$, are required (or known) by the automotive engineer, it will be shown that the radiator setpoint, pump speed, and fan speed can be indirectly designed based on the engine's thermal conditions and commutation strategy (refer to Remark 3.2).*

58

To facilitate the controller's development and quantify the temperature tracking control objective, the tracking error signals $\eta_e(t)$, $\eta_r(t)$, $\eta_p(t)$, and $\eta_f(t)$ are defined as

$$\eta_e \triangleq T_{ed} - T_e, \quad \eta_r \triangleq T_r - T_{vr}, \quad \eta_p \triangleq \omega_{pd} - \omega_p, \quad \eta_f \triangleq \omega_{fd} - \omega_f. \tag{3.11}$$

By adding and subtracting $MT_{vr}(t)$ to equation (3.1), and expanding the variables

$$\dot{m}_c \triangleq \rho_c c_c \omega_p, \quad \dot{m}_a \triangleq \rho_a c_a \omega_f, \quad M \triangleq M_1 \omega_{po}, \quad M_1 \triangleq c_{pc} \rho_c c_c, \quad M_2 \triangleq \varepsilon c_{pa} \rho_a c_a, \quad \text{and}$$

$\omega_{pd} \triangleq \bar{\omega}_{pd} + \omega_{po}$, the engine and radiator dynamics can be rewritten as

$$C_e \dot{T}_e = Q_{in} - M_1 \left(\bar{\omega}_{pd} - \eta_p \right) \left(T_e - T_r \right) - M \left(T_e - T_{vr} \right) + M\eta_r \tag{3.12}$$

$$C_r \dot{T}_r = -Q_o + M_1 \left(\omega_{pd} - \eta_p \right) \left(T_e - T_r \right) - M_2 \left(\omega_{fd} - \eta_f \right) \left(T_e - T_\infty \right) \tag{3.13}$$

where $\eta_r(t)$, $\eta_p(t)$, and $\eta_f(t)$ were introduced in equation (3.11), ω_{po} is a positive design constant that represent the minimum coolant pump speed, and c_c, c_a, ρ_c and ρ_a are real positive constants and fully known. The dynamics of the coolant pump and radiator fan hydraulic motors can be rewritten using equation (3.9) as

$$\frac{J_p}{x_{mp}} \dot{\omega}_p = f_p - M_p X_p, \quad \frac{J_f}{x_{mf}} \dot{\omega}_f = f_f - M_f X_f \tag{3.14}$$

where $f_p \triangleq \left(\dfrac{D_{mp}^2 + B_{mp} C_{imp}}{D_{mp} x_{mp}} \right) P_{Lp} + \left(\dfrac{B_{mp} V_{tp}}{2 D_{mp} \beta_p x_{mp}} \right) \dot{P}_{Lp} - \dfrac{T_{Lp}}{x_{mp}}, M_p \triangleq \dfrac{B_{mp}}{D_{mp}} C_{dp} w_p \sqrt{\dfrac{P_{Sp} - P_{Lp}}{\rho_p}}$

$, \quad X_p \triangleq \dfrac{x_p}{x_{mp}}, \quad f_f \triangleq \left(\dfrac{D_{mf}^2 + B_{mf} C_{imf}}{D_{mf} x_{mf}} \right) P_{Lf} + \left(\dfrac{B_{mf} V_{tf}}{2 D_{mf} \beta_f x_{mf}} \right) \dot{P}_{Lf} - \dfrac{T_{Lf}}{x_{mf}}, \quad X_f \triangleq \dfrac{x_f}{x_{mf}}, \quad \text{and}$

$M_f \triangleq \dfrac{B_{mf}}{D_{mf}} C_{df} w_f \sqrt{\dfrac{P_{Sf} - P_{Lf}}{\rho_f}}$.

<u>Closed–Loop Error System Development and Controller Formulation</u>

The open–loop error system can be analyzed by taking the first time derivative of all the expressions in equation (3.11) and then multiplying both sides of the resulting equations by C_e, C_r, $\dfrac{J_p}{x_{mp}}$, and $\dfrac{J_f}{x_{mf}}$ for the engine, radiator, hydraulic coolant pump, and hydraulic radiator fan dynamics, respectively. The system dynamics in equations (3.12–3.14) can be substituted and then reformatted to realize

$$C_e \dot{\eta}_e = C_e \dot{T}_{ed} - Q_{in} + M\left(T_e - T_{vro}\right) - M\eta_r - M_1\left(T_e - T_r\right)\eta_p - u_e \qquad (3.15)$$

$$C_r \dot{\eta}_r = -Q_o + M\left(T_e - T_r\right) - M_1\left(T_e - T_r\right)\eta_p + M_2\left(T_e - T_\infty\right)\eta_f - C_r \dot{T}_{vr} + u_r \qquad (3.16)$$

$$\frac{J_p}{x_{mp}}\dot{\eta}_p = \frac{J_p}{x_{mp}}\dot{\omega}_{pd} - f_p + u_p, \quad \frac{J_f}{x_{mf}}\dot{\eta}_f = \frac{J_f}{x_{mf}}\dot{\omega}_{fd} - f_f + u_f. \qquad (3.17)$$

In these expressions, equation (3.9) was utilized plus $T_{vr} \triangleq \bar{T}_{vr} + T_{vro}$, $u_e \triangleq M\bar{T}_{vr} - M_1\left(T_e - T_r\right)\bar{\omega}_{pd}$, $u_r \triangleq M_1\left(T_e - T_r\right)\bar{\omega}_{pd} - M_2\left(T_e - T_\infty\right)\omega_{fd}$, $u_p \triangleq M_p X_p$, and $u_f \triangleq M_f X_f$. The parameter T_{vro} is a positive design constant.

Remark 3.2: *The control inputs $\bar{T}_{vr}(t)$, $\bar{\omega}_{pd}(t)$, $\omega_{fd}(t)$, $X_p(t)$, and $X_f(t)$ are uni–polar. Hence, commutation strategies are designed utilizing the bi–polar control laws $u_e(t)$, $u_r(t)$, $u_p(t)$ and $u_f(t)$ as*

$$\bar{\omega}_{pd} \triangleq \frac{\left[\operatorname{sgn}\left(u_e\right) - 1\right]u_e}{2M_1\left(T_e - T_r\right)}, \quad \bar{T}_{vr} \triangleq \frac{\left[1 + \operatorname{sgn}\left(u_e\right)\right]u_e}{2M}, \quad \omega_{fd} \triangleq \frac{\left[1 + \operatorname{sgn}\left(F\right)\right]F}{2M_2\left(T_e - T_\infty\right)} \qquad (3.18)$$

$$X_p \triangleq \frac{\left[1 + \operatorname{sgn}\left(u_p\right)\right]u_p}{2M_p}, \qquad X_f \triangleq \frac{\left[1 + \operatorname{sgn}\left(u_f\right)\right]u_f}{2M_f} \qquad (3.19)$$

where M_1, M_2, M_p and M_f were introduced in equations (3.12–3.14), and $F \triangleq M_1\left(T_e - T_r\right)\bar{\omega}_{pd} - u_r$. The control input, $\omega_{fd}(t)$ is obtained from equation (18) after $\bar{\omega}_{pd}(t)$ is computed. From these definitions, it is clear that if $u_e(t)$,

$u_r(t)$, $u_p(t)$, $u_f(t) \in L_\infty$ at all time, then $\bar{\omega}_{pd}(t), \bar{T}_{vr}(t), \omega_f(t), X_p(t), X_f(t) \in L_\infty$ at all time.

To facilitate the subsequent analysis, the expressions in equations (3.12–3.15) are rewritten as

$$C_e \dot{\eta}_e = N_e - M\eta_r - M_1(T_e - T_r)\eta_p - u_e \tag{3.20}$$

$$C_r \dot{\eta}_r = N_r - M_1(T_e - T_r)\eta_p + M_2(T_e - T_\infty)\eta_f - C_r \dot{T}_{vr} + u_r \tag{3.21}$$

$$\frac{J_p}{x_{mp}}\dot{\eta}_p = N_p + \frac{J_p}{x_{mp}}\dot{\omega}_{pd} + u_p, \quad \frac{J_f}{x_{mf}}\dot{\eta}_f = N_f + \frac{J_f}{x_{mf}}\dot{\omega}_{fd} + u_f \tag{3.22}$$

where the functions $N_e(T_e,t)$, $N_r(T_e,T_r,t)$, $N_p(P_{Lp},\dot{P}_{Lp},T_{Lp},t)$, and $N_f(P_{Lf},\dot{P}_{Lf},T_{Lf},t)$ are defined as

$$N_e \triangleq C_e \dot{T}_{ed} - Q_{in} + M(T_e - T_{vro}), \quad N_r \triangleq M(T_e - T_r) - Q_o, \quad N_p \triangleq -f_p, \quad N_f \triangleq -f_f \tag{3.23}$$

and can be upper bounded as $N_e \le \varepsilon_{ee}$, $N_r \le \varepsilon_{rr}$, $N_p \le \varepsilon_{pp}$, and $N_f \le \varepsilon_{ff}$, respectively, based on Assumptions 3.1, 3.3–3.5, and 3.7, where ε_{ee}, ε_{rr}, ε_{pp}, $\varepsilon_{ff} \in \mathbb{R}^+$ are constants. By utilizing a Lyapunov stability analysis, the control laws $u_e(t)$, $u_r(t)$, $u_p(t)$ and $u_f(t)$, introduced in equations (3.15–3.17), are designed as shown in Table 3.1 where $F(t)$ was introduced in equation (3.18), k_e is a positive control gain, and the variables $B_1(\bullet)$ through $B_{49}(\bullet)$ are defined in Appendix C. Knowledge of $u_e(t)$, $u_r(t)$, $u_p(t)$ and $u_f(t)$, based on Table 1, allows the commutation relationships of equations (3.18) and (3.19) to be calculated which provides $\bar{T}_{vr}(t)$, $\bar{\omega}_{pd}(t)$, $\omega_{fd}(t)$, $X_p(t)$, and

$X_f(t)$. Finally, the voltage signals for the pump and fan servo–solenoid valve are prescribed using $X_p(t)$ and $X_f(t)$ with *a priori* linear empirical relationships.

Case	Condition	u_e	u_r	u_p	u_f
I	$u_e > 0, F \leq 0$		$B_1\eta_e + B_2\eta_r$	$B_9\eta_e + B_{10}\eta_r + B_{11}\eta_p$	$B_{27}\eta_r + B_{28}\eta_f$
II	$u_e \leq 0, F \leq 0$		$B_3\eta_e + B_4\eta_r$	$B_{12}\eta_e + B_{13}\eta_r + B_{14}\eta_p +$ $B_{15}\eta_e\eta_r + B_{16}\eta_e\eta_p + B_{17}\eta_e^2$	$B_{29}\eta_r + B_{30}\eta_f +$ $B_{31}\eta_e\eta_p$
III	$u_e > 0, F > 0$	$k_e\eta_e$	$B_5\eta_e + B_6\eta_r$	$B_{18}\eta_e + B_{19}\eta_r + B_{20}\eta_p$	$B_{32}\eta_e + B_{33}\eta_r + B_{34}\eta_p +$ $B_{35}\eta_f + B_{36}\eta_e\eta_r +$ $B_{37}\eta_e\eta_p + B_{38}\eta_r\eta_p +$ $B_{39}\eta_e^2 + B_{40}\eta_r^2$
IV	$u_e \leq 0, F > 0$		$B_7\eta_e + B_8\eta_r$	$B_{21}\eta_e + B_{22}\eta_r + B_{23}\eta_p +$ $B_{24}\eta_e\eta_r + B_{25}\eta_e\eta_p +$ $B_{26}\eta_e^2$	$B_{41}\eta_e + B_{42}\eta_r + B_{43}\eta_p +$ $B_{44}\eta_f + B_{45}\eta_e\eta_r +$ $B_{46}\eta_e\eta_p + B_{47}\eta_r\eta_p +$ $B_{48}\eta_e^2 + B_{49}\eta_r^2$

Table 3.1 The control laws $u_e(t)$, $u_r(t)$, $u_p(t)$, and $u_f(t)$ for the hydraulic control

Stability Analysis

A Lyapunov stability analysis guarantees that the advanced thermal management system will be stable when applying the control laws introduced in Table 3.1.

Theorem 3.1: *The controller given in Table 1 ensures that: (i) all closed–loop signals stay bounded for all time; and (ii) tracking is uniformly ultimately bounded (UUB) in the sense that* $|\eta_e(t)| \leq \varepsilon_e$, $|\eta_r(t)| \leq \varepsilon_r$, $|\eta_p(t)| \leq \varepsilon_p$ *and* $|\eta_f(t)| \leq \varepsilon_f$ *as* $t \to \infty$ *where* ε_e, ε_r, ε_p, $\varepsilon_f \in \mathbb{R}^+$ *are small constants.*

Proof: *See Appendix D for the complete Lyapunov stability analysis.*

Experimental Test Bench

An experimental test bench (refer to Figure 3.3) has been assembled to demonstrate the advanced thermal management system controller design. The assembled system offers a flexible, rapid, repeatable, and safe testing environment. The test bench features a hydraulic–driven radiator fan and coolant pump, two hydraulic servo control valves and six immersion heaters. In Addition, numerous sensors have been integrated to monitor the fluid temperatures, flow rates, pressures, and rotational shaft velocities.

The radiator inlet (engine) and radiator outlet temperatures are measured using two K–type thermocouples, while the ambient temperature is measured by a single J–type thermocouple. All thermocouple signals are isolated, amplified, and linearized via signal conditioners. In addition, two Monarch Instruments optical sensors are responsible for measuring the actuators' rotational speed, while a turbine flow meter records the coolant flow rate. Finally, Honeywell (Sensotec) A–5 pressure transducers are employed to measure the hydraulic supply and return pressures.

Data acquisition and control is accomplished using a dSPACE model 1104 controller board. Analog to Digital Conversion (ADC) is achieved through either a single 16–bit channel which accommodates four multiplexed input signals, or one of four 12–bit channels which accommodate one input signal each. Additionally, there are eight parallel channels available for Digital to Analog Converter (DAC) as well as twenty digital inputs/outputs. The controller board interfaces with Matlab's Simulink allowing for real–time execution of control strategies. The coding in Simulink is flexible allowing for implementation of C code, Matlab M–files, and Simulink block diagrams. In addition,

dSPACE's "Control Desk" software is used to set up and monitor experiments while also capturing experimental results.
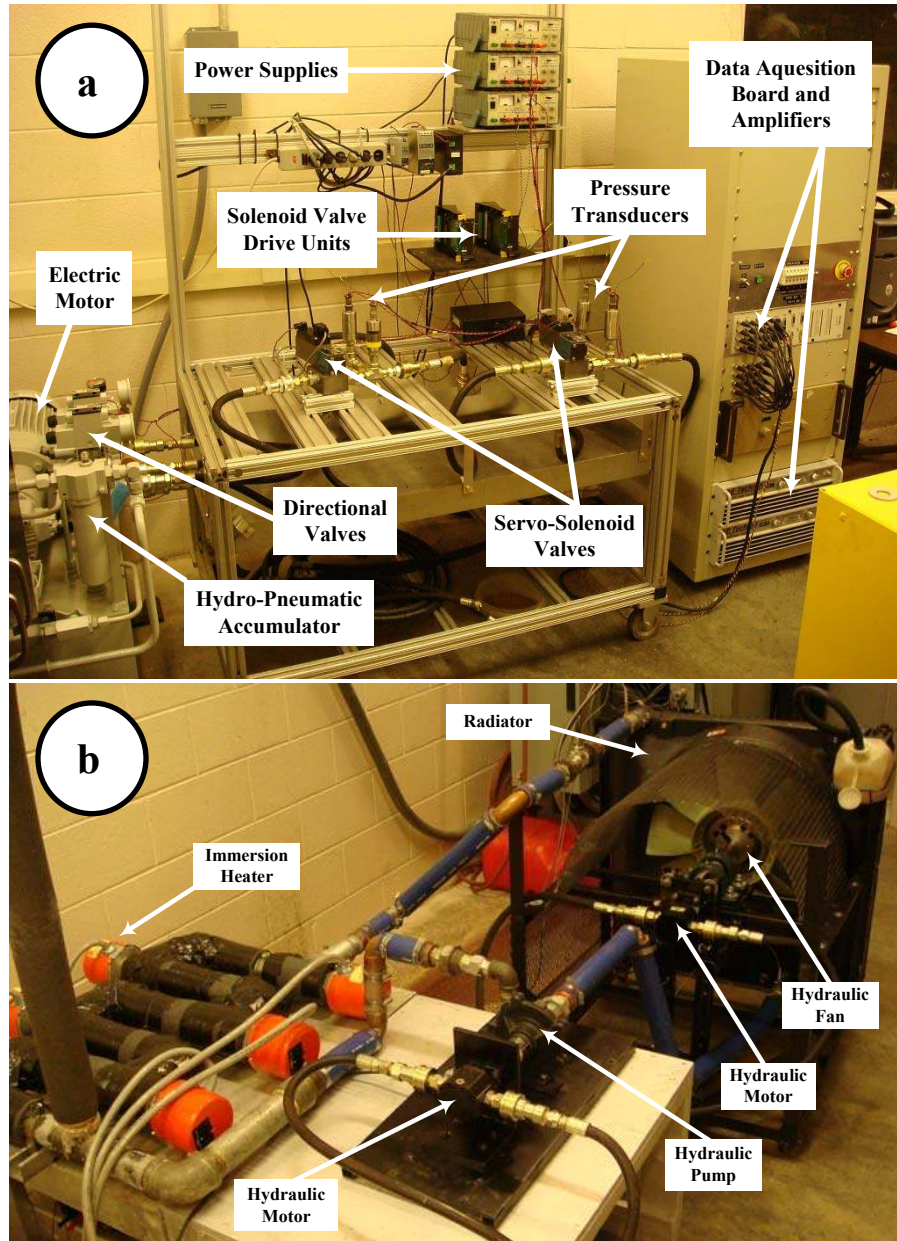
Figure 3.3 Experimental hydraulic–based thermal test bench; (a) Hydraulic system that features an electric motor, hydro–pneumatic accumulator, two directional valves, two servo–solenoid proportional control valves, solenoid valve drive units, and pressure transducers; and (b) Thermal system that features six immersion heating coils, hydraulic–driven coolant pump, radiator with a hydraulic–driven fan, and various (*e.g.*, temperature, flow rate, and motor speed) sensors

The experimental setup utilizes a series of six Temco 110VAC immersion heater coils to heat water circulating within the system. This heat transfer process simulates the internal combustion engine and its associated coolant. This configuration can provide up to 12kW of energy (2kW/heater) and is setup such that individual heaters may be switched on/off to provide fluctuations in the input heat. Once heated, the water is circulated via a hydraulically driven coolant pump through a radiator (6.8L capacity) where forced convection is provided by a hydraulically driven fan. Both the coolant pump and radiator fan are driven by hydraulic gear type motors. The centrifugal pedestal mount coolant pump is capable of delivering up to 58GPM of coolant. It is driven by a Haldex hydraulic motor with a displacement of 6.36cm^3/rev, while the radiator fan utilizes a Haldex motor with a displacement of 11.65cm^3/rev. Hydraulic flow to the motors is controlled using either two servo–solenoid proportional control valves (BOSCH NG 6) or four solenoid operated cartridge/poppet valves (Parker B09–2–6P). The servo solenoid valves are driven by Bosch PL 6 amplifier cards which feature built in PID position control. This allows for spool displacements which are proportional to a 0–10VDC input signal. Supply pressure for the hydraulic components is provided through a hydraulic power unit. The unit consists of a 7.5hp Baldor industrial electric motor spinning a Bosch Hydraulic pump with a displacement of 16.39cm^3/rev. A Bosch hydro–pneumatic accumulator is used for energy storage and two Bosch directional control valves allow separate pressure supplies to the two actuators.

Numerical and Experimental Results

In this section, numerical and experimental results are presented to verify and validate the mathematical models and control design. First, a Matlab/Simulink™ simulation has been created and executed to evaluate the robustness of the proposed backstepping nonlinear control algorithm. Second, two scenarios (*e.g.*, steady heat and variable heat with ram air disturbance) of experimental tests have been conducted on the hydraulic–based thermal test bench to investigate and evaluate the control design performance. The proposed thermal model parameter values and control gains and constants used in the simulation and experimental testing are presented in Table 3.2.

Symbol	Value	Unit	Symbol	Value	Unit	Symbol	Value	Unit
B_{mp}	0.95	N.s/cm	J_f	1.13	kg.cm^2	w_p	3.62	cm^2/cm
B_{mf}	5.31	N.s/cm	k_e	1500	–	w_f	3.62	cm^2/cm
c_{pa}	1.005	kJ/kg.°K	k_f	2500	–	x_{mp}	3	mm
c_{pc}	4.18	kJ/kg.°K	k_p	2000	–	x_{mf}	3	mm
C_{dp}	0.63	–	k_r	1500	–	β_p	689.48	MPa
C_{df}	0.63	–	P_{Sp}	3447	kPa	β_f	689.48	MPa
C_e	0.33	kJ/°K	P_{Sf}	6895	kPa	ε	0.63	–
C_{imp}	0.0025	cm^5/N.sec	T_{Lp}	0	N.cm	ρ_a	1.184	Kg/m^3
C_{imf}	0.0025	cm^5/N.sec	T_{Lf}	0	N.cm	ρ_c	997.05	Kg/m^3
C_r	0.25	kJ/°K	T_{vro}	316.5	°K	ρ_p	900	Kg/m^3
D_{mp}	1.01	cm^3/rad	T_∞	300	°K	ρ_f	900	Kg/m^3
D_{mf}	1.85	cm^3/rad	V_{tp}	119626	cm^3	ω_{po-SIM}	35	rad/s
J_p	0.904	kg.cm^2	V_{tf}	36871	cm^3	ω_{po-EXP}	40	rad/s

Table 3.2 Numerical simulation parameter values. Some of these parameter values are used to implement the experimental backstepping robust control strategy

Numerical Simulation

A numerical simulation of the backstepping robust control strategy, introduced in Section 3.3, has been performed on the system dynamics equations (3.12–3.14) to demonstrate the performance of the proposed controller in Table 3.1. For added reality, band–limited white noise was added to the sensors' measurement (*e.g.*, noise power =0.00001 and sampling time =0.005sec). A "load" cycle and external ram air disturbance were applied as shown in Figure 3.4a and 3.4b. The desired engine temperature was T_{ed}=322ºK. The initial simulation conditions were $T_e(0)$=313.7ºK and $T_r(0)$=310.9ºK.

Figures 3.4c and 3.4d show the engine and radiator temperatures response and the engine temperature tracking error, respectively, for the variable input heat and ram air disturbance introduced in Figures 3.4a and 3.4b. Figure 3.4d clearly shows that the steady state absolute tracking error is always below 0.5ºK during the test period T=2000sec. In Figures 3.4e and 3.4f, the hydraulic coolant pump and radiator fan are presented. It was observed that when the input heat changes critically from a high to a lower magnitude at T=1000sec and 1700sec, the hydraulic fan speed goes maximum instantaneously per Figure 3.4f to cool down the radiator temperature that increases per heat change as shown in Figure 3.4a. In addition, whenever the pump effort increases, the fan effort decreases which is ideal for power minimization. Actually, the coolant pump behaves to assist the engine temperature tracking while the radiator pump behaves to assist the radiator temperature tracking for the virtual reference, T_{vr}. Table 3.3 summarizes the results obtained in the simulation.
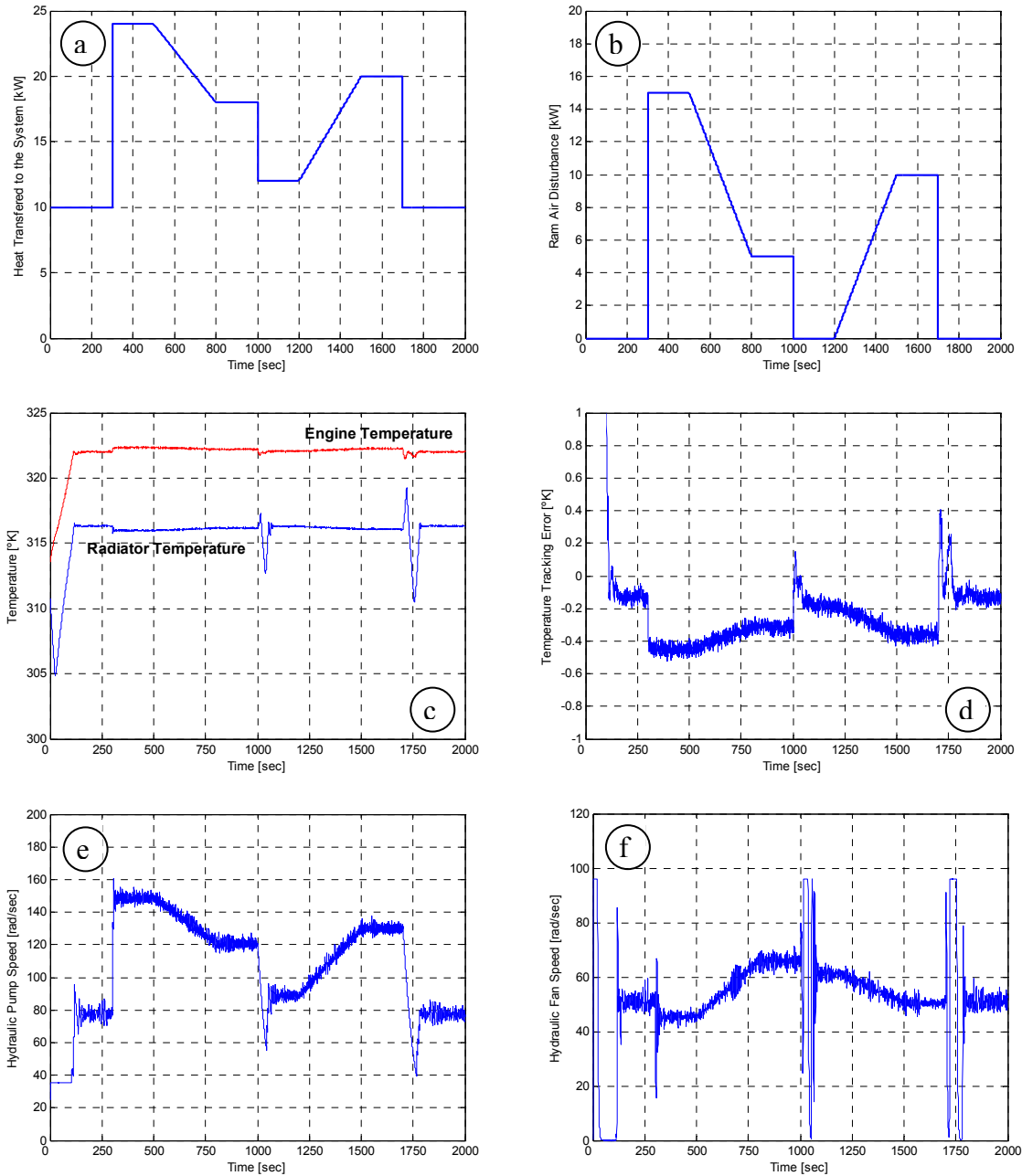
Figure 3.4 Numerical response for variable engine thermal loads and ram air disturbance; (a) input heat profile, $Q_{in}(t)$; (b) ram air disturbance, $Q_o(t)$, to emulate different vehicle speeds; (c) Simulated engine and radiator temperatures response for a desired engine temperature of T_{ed}=322ºK; (d) Simulated engine commanded temperature tracking error; (e) Simulated coolant mass flow rate through the pump; and (f) Simulated air mass flow rate through the radiator fan

68

Time [sec]	Q_{in} [kW]	Q_o [kW]	ω_{pss} [rad/sec]	ω_{fss} [rad/sec]	$|\eta_{ess}|$ [°K]
1–300	10	0	77	51	0.15
300–500	24	15	149	46	0.46
500–800	–t/50 + 34	–t/30 + 31.67	–7t/75 + 195.67	t/15 + 12.67	–7t/15000 + 0.69
800–1000	18	5	121	66	0.32
1000–1200	12	0	89	61	0.18
1200–1500	2t/75 – 20	t/30 – 40	41t/300 + 75	–t/30 + 101	19t/30000 – 0.58
1500–1700	20	10	130	51	0.37
1700–2000	10	0	77	51	0.15

Table 3.3 Numerical simulation response summary for the applied heat and disturbance per Figures 3.4a and 3.4b

Experimental Testing

Two experimental tests have been conducted on the hydraulic–based thermal test bench to investigate the robust control design performance. The first case applies a fixed input heat of Q_{in} =12kW (*i.e.*, six heaters are used) and no ram air disturbance (*i.e.,* to emulate the vehicle is idle). In Figure 3.5a, the engine and radiator temperatures response is presented. From Figure 3.5b, the controller can achieve a steady state absolute value temperature tracking error of 0.7°K. In Figures 3.5c and 3.5d, the hydraulic coolant pump and radiator fan response is presented. Based on the response per Figures 3.5c and 3.5d, the power consumption were P_{sys} =165.23kW.

Table 3.4 presents an experimental summary to compare different control strategies for the first experimental test. The controller gains, initial conditions, and temperature set points were maintained for all experimental tests. In Table 3.3, the backstepping robust controller achieved the least absolute steady state engine temperature tracking error when compared to the Proportional–Integral–Derivative (PID) and Pulse–Width–Modulation (PWM) control methods. Note that the PWM control method applied to only poppet valves. Although the hydraulic–driven system components consume more

power (*i.e.*, 4.76W) when using the robust controller compared to the PID control method, it achieves 42% improvement in the engine temperature tracking error. Overall, the backstepping robust control shows better results in terms of engine temperature tracking error and power consumption when compared to the other control methods.
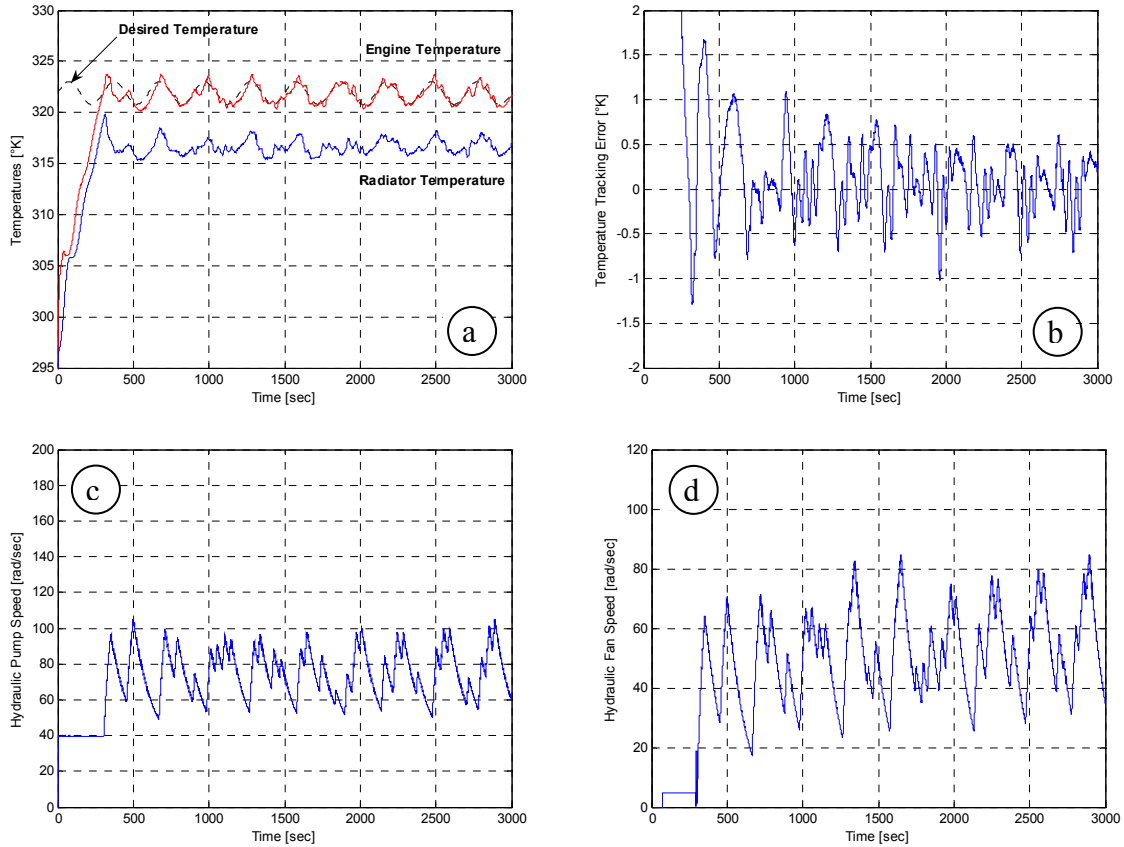
Figure 3.5 First experimental test with an input heat of Q_{in} = 12kW and no ram air disturbance; (a) Experimental engine and radiator temperatures with a desired engine temperature profile $T_{ed} = 322 + 2\sin\left(\frac{\pi t}{150}\right)$°K; (b) Experimental engine temperature tracking error; (c) Experimental coolant mass flow rate through the pump; and (d) Experimental air mass flow rate through the radiator fan

Operation Strategies Description	Valve	$|\eta_{ep}|$ [°K]	$|\eta_{ess}|$ [°K]	P_{sys} [W]	Rank
Backstepping robust controller	Servo–Solenoid	1.25	0.7	165.23	1
PID controller	Servo–Solenoid	4.10	1.2	160.47	2
PWM control method	Poppet	4.12	2.2	127.89	3

Table 3.4 Experimental summary for three cooling system control strategies with steady heat and no ram air disturbance (first test). For the second operation strategy, the PID controller's gains were set as K_P =0.26, K_I =0.01 and K_D =0.44. For the third operation strategy, the coolant pump speed was set as 62.82rad/sec where the radiator fan was controlled by a PWM control method. The PWM frequency was set as 1Hz while the duty cycle was controlled (*i.e.*, [0–100]%) via a PID controller. The PID controller's gain were set as K_P=0.02, K_I=7.6 10^{-4}, and K_D=0.04

Remark 3.3: *The power measure* $P_{sys} = \dfrac{1}{T}\int_{t_o}^{t}\left[P_{Lp}(\tau)Q_{Lp}(\tau)+P_{Lf}(\tau)Q_{Lf}(\tau)\right]d\tau$ *calculates*

the average power consumed by the system actuators for the duration of the experimental test T=50min.

The second scenario varies both the input heat and disturbance. Specifically $Q_{in}(t)$ changes from 8kW to 12kW at t=1500sec while $Q_o(t)$ remains zero at t=1500sec but varies at t=3000sec from zero to emulate a vehicle traveling at 35km/h (refer to Figure 3.6). Due to system heating limitation, excessive input heat and ram air disturbance variations were not tested. In Figure 3.6a, the engine and radiator temperature response is presented. From Figure 3.6b, it is clear that the proposed control strategy can handle the input heat and ram air variations satisfactory since the maximum engine temperature absolute value steady state tracking error is below 0.9°K. Figures 3.6c and 3.6d show the hydraulic coolant pump and radiator fan response.
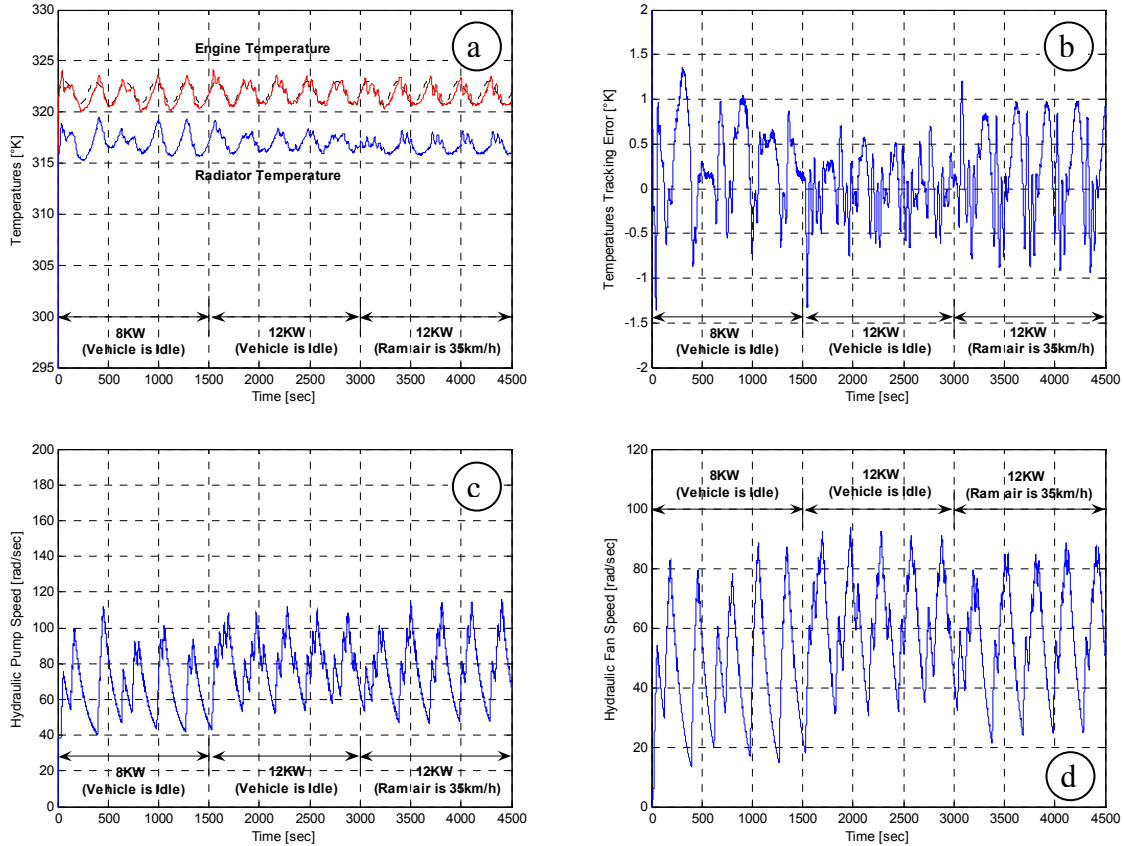
Figure 3.6 Second experimental test with a variable input heat and ram air disturbance; (a) Experimental engine and radiator temperatures with a desired engine temperature profile $T_{ed} = 322 + 2\sin\left(\pi t/150\right)$°K; (b) Experimental engine temperature tracking error; (c) Experimental coolant mass flow rate through the pump; and (d) Experimental air mass flow rate through the radiator fan

<u>Concluded Remarks</u>

Advanced automotive thermal management system can have a positive impact on gasoline and diesel engine cooling systems. In this chapter, a suit of hydraulic motors based–cooling system components have been assembled and controlled using a Lyapunov–based nonlinear control technique. The control algorithm has been investigated using both simulation and experimental tests. A comprehensive detailed and supplemental controller was applied to regulate the coolant temperature. The controller

successfully maintained the coolant temperature to setpoint temperature with a small error percentage. It has also been shown that the power consumed by the system hydraulic actuators can be reduced. Overall, the findings demonstrated that setpoint temperatures can be maintained satisfactory while minimizing power consumption which ultimately impacts fuel economy.

CHAPTER 4
CONCLUSIONS

An advanced automotive thermal management system can positively influence the coolant temperature regulation and associated cooling component power consumption. In this PhD dissertation, a suite of servo–motor based–cooling system components have been experimentally assembled and controlled utilizing Lyapunov–based nonlinear control techniques. These control algorithms have been extensively investigated using both simulation and laboratory experimental tests.

For the first experimental test bench, introduced in Chapter 1, two detailed controllers were applied to regulate the engine coolant temperature. Both controllers successfully maintained the engine block to setpoint temperatures with small error percentages. It has also been shown that the temperature tracking error and power consumed by the system actuators can be reduced by 35% and 14%, respectively, when compared to other control methods. In the second multi–loop experimental test bench, introduced in Chapter 2, the proposed control strategy successfully maintained the engine coolant and transmission fluid temperatures to user–defined setpoint values with $0.13°K$ and $0.65°K$ temperature tracking error. Further, the power consumed by the cooling system actuators was reduced by 92%, when compared to the traditional factory control method, through the synchronous control of the coolant pumps and radiator fan motors. The occurrence of elevated ambient temperatures required the cooling components to operate at maximum speeds for heat dissipation which increased power consumption. Finally, in the hydraulic actuators–based experimental test bench, introduced in Chapter 3, a comprehensive controller was applied to regulate the coolant temperature. The

controller successfully maintained the coolant temperature to its setpoint with a 42% improvement in the tracking error. It has also been shown that the power consumed by the system hydraulic actuators can be reduced satisfactory.

Overall, the findings demonstrated that setpoint temperatures can be maintained satisfactory while minimizing power consumption which should assist in the quest for less tailpipe emissions and parasitic losses as well as greater vehicle fuel economy.

APPENDICES

Let $V(z,t) \in \mathbb{R}$ denote the non–negative function

$$V \triangleq \frac{1}{2} C_e e^2 + \frac{1}{2} C_r \eta^2 \qquad (A.1)$$

where $z(t) \in \mathbb{R}^2$ is defined as

$$z \triangleq \begin{bmatrix} e & \eta \end{bmatrix}^T . \qquad (A.2)$$

Note that (A.1) is bounded as (refer to Theorem 2.14 of Qu (1998))

$$\lambda_1 \|z(t)\|^2 \leq V(z,t) \leq \lambda_2 \|z(t)\|^2 \qquad (A.3)$$

where λ_1, and λ_2 are positive constants. After taking the time derivative of (A.1), then

$$\dot{V} = e N_{ed} + e \tilde{N}_e - e u_e - e M \eta + \eta N_{rd} + \eta \tilde{N}_r + \eta u_r - \eta C_r \dot{T}_{vr} \qquad (A.4)$$

where (1.16) was utilized. From Appendix B, an expression for $\eta(t) C_r \dot{T}_{vr}(t)$ becomes

$$\eta C_r \dot{T}_{vr} = \frac{1}{2}[1 + \mathrm{sgn}(u_e)] x, \qquad x = \eta C_r \left(\beta_1 N_e - \beta_2 e - \beta_3 \eta \right) \qquad (A.5)$$

where β_1, β_2, and β_3 are defined in (B.3). From (A.5), it is clear that $\eta(t) C_r \dot{T}_{vr}(t)$, introduced in (A.4), changes with respect to the sign of the control input $u_e(t)$. Consequently, two cases are realized.

Case I: $\eta C_r \dot{T}_{vr} = 0$ **when** $u_e \in (-\infty, 0)$

The expression of $\dot{V}(t)$, introduced in (A.4), can be rewritten as

$$\dot{V} = e N_{ed} + e \tilde{N}_e - K_e e^2 + \eta N_{rd} + \eta \tilde{N}_r - K_r \eta^2 + e M \eta \qquad (A.6)$$

where (1.20) and (1.21) were utilized. To facilitate the subsequent analysis, the auxiliary signals $\tilde{N}_e(T_e, t)$ and $\tilde{N}_r(T_e, T_r, t)$, introduced in (1.17) can be computed as

$$\tilde{N}_e = -Me \tag{A.7}$$

$$\tilde{N}_r = -Me - M\eta \tag{A.8}$$

where (1.18) and (1.19) were used as well as M introduced in (1.11). Application of (A.7), (A.8), and the triangle inequality allows $\dot{V}(t)$ to be upper bounded as

$$\dot{V} \le -K_e |e|^2 - K_r |\eta|^2 + |e||N_{ed}| - M|e|^2 + |\eta||N_{rd}| - M|\eta|^2. \tag{A.9}$$

By using (A.2) and completing the squares for the last four terms on the right–hand side of (A.9), the following inequality can be obtained (Qu, 1998) as

$$\dot{V} \le -\lambda_3 \|z\|^2 + \varepsilon_o \tag{A.10}$$

where $\lambda_3 = \min\{K_e, K_r\}$ and $\varepsilon_o \triangleq \dfrac{|N_{ed}|^2}{4M} + \dfrac{|N_{rd}|^2}{4M}$. From (A.1), (A.3), and (A.10), then

$V(z, t) \in L_\infty$; hence, $e(t), \eta(t), z(t) \in L_\infty$. From (1.10) and Assumption 4, $T_e(t) \in L_\infty$ since $e(t), \eta(t) \in L_\infty$ and $u_e(t), u_r(t) \in L_\infty$ based on (1.20) and (1.21). Thus, $T_{vr}(t) \in L_\infty$ can be realized using (1.15) in Remark 1.2 and the relation $T_{vr} = T_{vro} + \bar{T}_{vr}$. From the previous bounding statements, $T_r(t), \dot{m}_r(t), H(t), \dot{m}_c(t), \dot{m}_f(t) \in L_\infty$ since $\dot{m}_r = m_o + \bar{m} = H_o \dot{m}_c + \bar{H}\dot{m}_c$ and the information in (1.10), (1.15), and (1.16).

Case II: $\eta C_r \dot{T}_{vr} \ne 0$ **when** $u_e \in [0, \infty)$

The expression of $\dot{V}(t)$, introduced in (A.4), can be rewritten as

$$\dot{V} = eN_{ed} + e\tilde{N}_e - K_e e^2 + \eta N_r - K_r \eta^2 - \eta C_r \beta_1 N_e + eM\eta - K_e \frac{C_r}{C_e} e\eta \qquad \text{(A.11)}$$

where (1.17), (1.20), (1.21), and (A.5) were applied. For convenience, the expression in (A.11) may be rewritten as

$$\dot{V} = -K_e e^2 - K_r \eta^2 + e\tilde{N}_e + eN_{ed} + \eta \tilde{N} + \eta N_d + eM\eta - K_e \frac{C_r}{C_e} e\eta \qquad \text{(A.12)}$$

where the auxiliary signal $\tilde{N}(T_e, T_r, t)$ becomes

$$\tilde{N} \triangleq N - N_d. \qquad \text{(A.13)}$$

The variables $N(T_e, T_r, t)$ and $N_d(t)$ are defined as

$$N \triangleq N_r - C_r \beta_1 N_e, \quad N_d \triangleq N \big|_{T_e = T_{ed}, T_r = T_{vr}} = N_{rd} - C_r \beta_1 N_{ed} \qquad \text{(A.14)}$$

where $N_e(t), N_r(t), N_{ed}(t)$ and $N_{rd}(t)$ were introduced in (1.18), (1.19), and β_1 was introduced in (B.3). The auxiliary signal $\tilde{N}(T_e, T_r, t)$, introduced in (A.13), can be computed as

$$\tilde{N} = -\left(M - K_e \frac{C_r}{C_e}\right) e - M\eta \qquad \text{(A.15)}$$

based on (1.17), (1.18), (1.19), and (B.3). By utilizing (A.7), (A.16), and the triangle inequality, $\dot{V}(t)$ in (A.12) can be upper bounded as

$$\dot{V} \le -K_e |e|^2 - K_r |\eta|^2 + |e||N_{ed}| - M|e|^2 + |\eta||N_d| - M|\eta|^2. \qquad \text{(A.16)}$$

The final step of the proof follows the same argument presented in Case I to demonstrate that $\dot{V} \le -\lambda_3 \|z\|^2 + \varepsilon_o$ and all signals are bounded where $\varepsilon_o \triangleq \frac{|N_{ed}|^2}{4M} + \frac{|N_d|^2}{4M}$.

The expression for $C_r T_{vr}(t)$ can be written as

$$C_r T_{vr} = \begin{cases} C_r T_{vro} & , \quad \forall u_e \in (-\infty, 0) \\ C_r T_{vro} + \dfrac{C_r u_e}{M}, & \forall u_e \in [0, \infty) \end{cases} \tag{B.1}$$

where (1.15) and the relation $T_{vr} = T_{vro} + \overline{T}_{vr}$ were utilized. The parameter M was introduced in (1.11). After taking the first time derivative of (B.1), the following expression can be obtained

$$C_r \dot{T}_{vr} = \begin{cases} 0 & , \quad \forall u_e \in (-\infty, 0) \\ C_r \left(\beta_1 N_e - \beta_2 e - \beta_3 \eta \right), & \forall u_e \in [0, \infty) \end{cases} \tag{B.2}$$

where (1.16), (1.17), and (1.20) were applied. The coefficients β_1, β_2 and β_3 are defined as

$$\beta_1 \triangleq \frac{K_e}{MC_e}, \quad \beta_2 \triangleq \frac{K_e^2}{MC_e}, \quad \beta_3 \triangleq \frac{K_e}{C_e}. \tag{B.3}$$

<u>Appendix C</u>
<u>Parameter Definitions for the Controller in Table 3.1</u>

The control parameters in Table 3.1 are bounded from Assumptions 3.2, 3.3, and

3.6. $B_1 \triangleq M - \dfrac{k_e^2 C_r}{MC_e}$, $\quad B_2 \triangleq -\dfrac{k_e C_r}{C_e} - k_r$, $\quad B_3 \triangleq M$, $\quad B_4 \triangleq -k_r$, $B_5 \triangleq M - \dfrac{k_e^2 C_r}{MC_e}$,

$B_6 \triangleq -\dfrac{k_e C_r}{C_e} - k_r$, $\; B_7 \triangleq M$, $\; B_8 \triangleq -k_r$, $\; B_9 \triangleq M_1(T_e - T_r)$, $\; B_{10} \triangleq M_1(T_e - T_r)\left[1 - \dfrac{k_e C_r}{MC_e}\right]$,

$B_{11} \triangleq -k_p$, $\quad\quad\quad B_{12} \triangleq M_1(T_e - T_r) + \dfrac{J_p k_e M}{M_1 C_r x_{mp}(T_e - T_r)} \quad\quad + \dfrac{J_p k_e^2 (T_r - T_{ed})}{M_1 C_e x_{mp}(T_e - T_r)^2}$,

$B_{13} \triangleq M_1(T_e - T_r) \quad\quad\quad + \dfrac{J_p k_e M(T_r - T_{ed})}{M_1 C_e x_{mp}(T_e - T_r)^2}$, $\quad B_{14} \triangleq \dfrac{J_p k_e(T_r - T_{ed})}{C_e x_{mp}(T_e - T_r)} - k_p$,

$B_{15} \triangleq -\dfrac{J_p k_e k_r}{M_1 C_r x_{mp}(T_e - T_r)^2}$, $\quad B_{16} \triangleq -\dfrac{J_p k_e}{C_r x_{mp}(T_e - T_r)}$, $\quad B_{17} \triangleq \dfrac{J_p k_e M}{M_1 C_r x_{mp}(T_e - T_r)^2}$,

$B_{18} \triangleq M_1(T_e - T_r)$, $\quad\quad B_{19} \triangleq M_1(T_e - T_r)\left[1 - \dfrac{k_e C_r}{MC_e}\right]$, $\quad\quad B_{20} \triangleq -k_p$,

$B_{21} \triangleq M_1(T_e - T_r) + \dfrac{J_p k_e M}{M_1 C_r x_{mp}(T_e - T_r)} + \dfrac{J_p k_e^2(T_r - T_{ed})}{M_1 C_e x_{mp}(T_e - T_r)^2}$, $\quad B_{22} \triangleq M_1(T_e - T_r) +$

$\dfrac{J_p k_e M(T_r - T_{ed})}{M_1 C_e x_{mp}(T_e - T_r)^2}$, $\quad B_{23} \triangleq -k_p + \dfrac{J_p k_e(T_r - T_{ed})}{C_e x_{mp}(T_e - T_r)}$, $\quad B_{24} \triangleq -\dfrac{J_p k_e k_r}{M_1 C_r x_{mp}(T_e - T_r)^2}$,

$B_{25} \triangleq -\dfrac{J_p k_e}{C_r x_{mp}(T_e - T_r)}$, $\quad B_{26} \triangleq \dfrac{J_p k_e M}{M_1 C_r x_{mp}(T_e - T_r)^2}$, $\quad B_{27} \triangleq -M_2(T_e - T_\infty)$, $\quad B_{28} \triangleq -k_f$,

$B_{29} \triangleq -M_2(T_e - T_\infty)$, $B_{30} \triangleq -k_f$, $B_{31} \triangleq \dfrac{J_p k_e M_2(T_e - T_\infty)}{M_1 C_r x_{mp}(T_e - T_r)^2}$, $B_{32} \triangleq \dfrac{-2J_f k_e M}{M_2 C_e x_{mf}(T_e - T_\infty)} +$

$$\frac{J_f k_e^3 C_r}{M_2 M C_e^2 x_{mf}\left(T_e - T_\infty\right)} - \frac{J_f k_r M}{M_2 C_r x_{mf}\left(T_e - T_\infty\right)} + \frac{J_f M^2\left(T_e - T_{vro}\right)}{M_2 C_e x_{mf}\left(T_e - T_\infty\right)^2} - \frac{J_f k_e^2 C_r\left(T_e - T_{vro}\right)}{M_2 C_e^2 x_{mf}\left(T_e - T_\infty\right)^2},$$

$$B_{33} \triangleq \frac{J_f k_e^2 C_r}{M_2 C_e^2 x_{mf}\left(T_e - T_\infty\right)} + \frac{J_f k_e k_r}{M_2 C_e x_{mf}\left(T_e - T_\infty\right)} + \frac{J_f k_r^2}{M_2 C_r x_{mf}\left(T_e - T_\infty\right)} - \frac{J_f k_e M C_r\left(T_e - T_{vro}\right)}{M_2 C_e^2 x_{mf}\left(T_e - T_\infty\right)^2}$$

$$-\frac{J_f k_r M\left(T_e - T_{vro}\right)}{M_2 C_e x_{mf}\left(T_e - T_\infty\right)^2} - \frac{J_f M^2}{M_2 C_e x_{mf}\left(T_e - T_\infty\right)} - M_2\left(T_e - T_\infty\right), \qquad B_{34} \triangleq \frac{J_f k_e M_1\left(T_e - T_r\right)}{M_2 C_e x_{mf}\left(T_e - T_\infty\right)} +$$

$$\frac{J_f k_r M_1\left(T_e - T_r\right)}{M_2 C_r x_{mf}\left(T_e - T_\infty\right)} - \frac{J_f M_1 M\left(T_e - T_r\right)}{M_2 C_e x_{mf}\left(T_e - T_\infty\right)} - \frac{J_f k_e k_r M_1\left(T_e - T_r\right)}{M_2 M C_e x_{mf}\left(T_e - T_\infty\right)}, \quad B_{35} \triangleq -\frac{J_f k_e}{C_e x_{mf}} - \frac{J_f k_r}{C_r x_{mf}}$$

$$-k_f, \qquad B_{36} \triangleq -\frac{J_f M^2}{M_2 C_e x_{mf}\left(T_e - T_\infty\right)^2} + \frac{2 J_f k_e^2 C_r}{M_2 C_e^2 x_{mf}\left(T_e - T_\infty\right)^2} + \frac{J_f k_e k_r}{M_2 C_e x_{mf}\left(T_e - T_\infty\right)^2},$$

$$B_{37} \triangleq -\frac{J_f M_1 M\left(T_e - T_r\right)}{M_2 C_e x_{mf}\left(T_e - T_\infty\right)^2} + \frac{J_f k_e^2 M_1 C_r\left(T_e - T_r\right)}{M_2 M C_e^2 x_{mf}\left(T_e - T_\infty\right)^2}, \qquad B_{38} \triangleq \frac{J_f k_e M_1 C_r\left(T_e - T_r\right)}{M_2 C_e^2 x_{mf}\left(T_e - T_\infty\right)^2}$$

$$+\frac{J_f k_r M_1\left(T_e - T_r\right)}{M_2 C_e x_{mf}\left(T_e - T_\infty\right)^2}, \qquad B_{39} \triangleq -\frac{J_f k_e M}{M_2 C_e x_{mf}\left(T_e - T_\infty\right)^2} + \frac{J_f k_e^3 C_r}{M_2 M C_e^2 x_{mf}\left(T_e - T_\infty\right)^2},$$

$$B_{40} \triangleq \frac{J_f C_r k_e M}{M_2 C_e^2 x_{mf}\left(T_e - T_\infty\right)^2} + \frac{J_f k_r M}{M_2 C_e x_{mf}\left(T_e - T_\infty\right)^2}, \qquad B_{41} \triangleq -\frac{J_f k_e M\left(T_e - T_{vro}\right)\left(T_r - T_\infty\right)}{M_2 C_e x_{mf}\left(T_e - T_r\right)\left(T_e - T_\infty\right)^2}$$

$$+\frac{J_f M^2\left(T_e - T_{vro}\right)}{M_2 C_e x_{mf}\left(T_e - T_\infty\right)^2} + \frac{J_f k_e^2\left(T_r - T_{ed}\right)}{M_2 C_e x_{mf}\left(T_e - T_r\right)\left(T_e - T_\infty\right)} - \frac{J_f M}{M_2 x_{mf}\left(T_e - T_\infty\right)}\left(\frac{k_e}{C_e} + \frac{k_r}{C_r}\right),$$

$$B_{42} \triangleq -\frac{J_f k_r M\left(T_e - T_{vro}\right)}{M_2 C_e x_{mf}\left(T_e - T_\infty\right)^2} + \frac{J_f k_e M\left(T_r - T_{ed}\right)}{M_2 C_e x_{mf}\left(T_e - T_r\right)\left(T_e - T_\infty\right)} - \frac{J_f}{M_2 x_{mf}\left(T_e - T_\infty\right)}\left(\frac{M^2}{C_e} - \frac{K_r^2}{C_r}\right)$$

$$-M_2\left(T_e - T_\infty\right), \qquad B_{43} \triangleq \frac{J_f k_e M_1\left(T_r - T_{ed}\right)}{M_2 C_e x_{mf}\left(T_e - T_\infty\right)} - \frac{J_f M_1 M\left(T_e - T_r\right)}{M_2 C_e x_{mf}\left(T_e - T_\infty\right)} + \frac{J_f k_r M_1\left(T_e - T_r\right)}{M_2 C_r x_{mf}\left(T_e - T_\infty\right)},$$

$$B_{44} \triangleq -\frac{J_f k_r}{C_r x_{mf}} - k_f, \qquad\qquad B_{45} \triangleq \frac{J_f k_e k_r}{M_2 C_e x_{mf} \left(T_e - T_\infty\right)^2} + \frac{J_f k_e M \left(T_r - T_\infty\right)}{M_2 C_e x_{mf} \left(T_e - T_r\right)\left(T_e - T_\infty\right)^2}$$

$$-\frac{J_f M^2}{M_2 C_e x_{mf} \left(T_e - T_\infty\right)^2}, \qquad\qquad B_{46} \triangleq \frac{J_f M_1}{M_2 C_e x_{mf} \left(T_e - T_\infty\right)^2} \left(k_e \left(T_r - T_\infty\right) - M \left(T_e - T_r\right)\right)$$

$$+\frac{J_p k_e M_2 \left(T_e - T_\infty\right)}{M_1 C_r x_{mp} \left(T_e - T_r\right)^2}, \quad B_{47} \triangleq \frac{J_f k_r M_1 \left(T_e - T_r\right)}{M_2 C_e x_{mf} \left(T_e - T_\infty\right)^2}, \quad B_{48} \triangleq \frac{J_f k_e^2 \left(T_r - T_\infty\right)}{M_2 C_e x_{mf} \left(T_e - T_r\right)\left(T_e - T_\infty\right)^2}$$

$$-\frac{J_f k_e M}{M_2 C_e x_{mf} \left(T_e - T_\infty\right)^2}, \text{ and } B_{49} \triangleq \frac{J_f k_r M}{M_2 C_e x_{mf} \left(T_e - T_\infty\right)^2}.$$

Appendix D
Proof of Theorem 3.1

Let $V(z,t) \in \mathbb{R}$ denote the non–negative function

$$V \triangleq \frac{1}{2}C_e\eta_e^2 + \frac{1}{2}C_r\eta_r^2 + \frac{J_p}{2x_{mp}}\eta_p^2 + \frac{J_f}{2x_{mf}}\eta_f^2 \tag{D.1}$$

where $z \triangleq \begin{bmatrix} \eta_e & \eta_r & \eta_p & \eta_f \end{bmatrix}^T$. The parameters $\eta_e(t)$, $\eta_r(t)$, $\eta_p(t)$, and $\eta_f(t)$ are

defined in equation (3.10). Note that equation (D.1) is bounded as (refer to Theorem 2.14

of Qu (1998)) $\lambda_1 \|z(t)\|^2 \leq V(z,t) \leq \lambda_2 \|z(t)\|^2$ where λ_1, and λ_2 are positive constants.

After taking the time derivative of equation (D.1), then

$$\dot{V} = \eta_e N_e + \eta_r N_r + \eta_p N_p + \eta_f N_f - \eta_e u_e + \eta_r u_r + \eta_p u_p + \eta_f u_f - M\eta_e\eta_r$$
$$- M_1(T_e - T_r)\eta_e\eta_p - M_1(T_e - T_r)\eta_r\eta_p + M_2(T_e - T_\infty)\eta_r\eta_f - C_r\dot{T}_{vr}\eta_r \tag{D.2}$$
$$+ \frac{J_p}{x_{mp}}\dot{\omega}_{pd}\eta_p + \frac{J_f}{x_{mf}}\dot{\omega}_{fd}\eta_f$$

where equations (3.20–3.22) were utilized. The expressions for $C_r\dot{T}_{vr}(t)\eta_r(t)$,

$\frac{J_p}{x_{mp}}\dot{\omega}_{pd}(t)\eta_p(t)$, and $\frac{J_f}{x_{mf}}\dot{\omega}_{fd}(t)\eta_f(t)$ can be obtained as

$$C_r\dot{T}_{vr}\eta_r \triangleq \frac{[1 + \text{sgn}(u_e)]}{2}F_r, \quad \frac{J_p}{x_{mp}}\dot{\omega}_{pd}\eta_p \triangleq \frac{[\text{sgn}(u_e) - 1]}{2}F_p,$$

$$\frac{J_f}{x_{mf}}\dot{\omega}_{fd}\eta_f \triangleq \frac{[1 + \text{sgn}(F)]}{2}F_f \tag{D.3}$$

where $F(t)$ and $u_e(t)$ were introduced in equation (3.18) and Table 3.1, respectively.

The parameters $F_r(t)$, $F_p(t)$, and $F_f(t)$ are defined as

$$F_r \triangleq \frac{C_r k_e}{M} \left[\dot{T}_{ed} + \frac{M(T_e - T_{vro}) - Q_{in}}{C_e} \right] \eta_r - \frac{C_r k_e^2}{MC_e} \eta_e \eta_r - \frac{C_r k_e M_1 (T_e - T_r)}{MC_e} \eta_r \eta_p$$

$$- \frac{C_r k_e}{C_e} \eta_r^2 \tag{D.4}$$

$$F_p \triangleq - \frac{J_p k_e}{M_1 x_{mp} (T_e - T_r)^2} \left[\dot{T}_{ed}(T_e - T_r) + \frac{(T_r - T_{ed})Q_{in}}{C_e} - \frac{M(T_e - T_{vro})(T_r - T_{ed})}{C_e} - \frac{Q_o}{C_r} \eta_e \right] \eta_p$$

$$- \frac{J_p k_e}{M_1 x_{mp}} \left[\frac{k_e(T_r - T_{ed})}{C_e(T_e - T_r)^2} + \frac{M}{C_r(T_e - T_r)} \right] \eta_e \eta_p - \frac{J_p k_e M(T_r - T_{ed})}{M_1 C_e x_{mp}(T_e - T_r)^2} \eta_r \eta_p$$

$$- \frac{J_p k_e(T_r - T_{ed})}{C_e x_{mp}(T_e - T_r)} \eta_p^2 - \frac{J_p k_e M_2(T_e - T_\infty)}{M_1 C_r x_{mp}(T_e - T_r)^2} \eta_e \eta_p \eta_f + \frac{J_p k_e}{C_r x_{mp}(T_e - T_r)} \eta_e \eta_p^2$$

$$- \frac{J_p k_e}{M_1 C_r x_{mp}(T_e - T_r)^2} u_r \eta_e \eta_p \tag{D.5}$$

$$F_f \triangleq \frac{J_f M_1 \overline{\omega}_{pd}}{M_2 C_r x_{mf}(T_e - T_\infty)} \left[Q_o - M(T_e - T_r) + M_1(T_e - T_r)\eta_p - M_2(T_e - T_\infty)\eta_f - u_r \right] \eta_f$$

$$+ \frac{J_f \left[M_1 \overline{\omega}_{pd}(T_r - T_\infty) + u_r \right]}{M_2 C_e x_{mf}(T_e - T_\infty)^2} \left[Q_{in} - M(T_e - T_{vro}) + M\eta_r + M_1(T_e - T_r)\eta_p + k_e \eta_e \right] \eta_f$$

$$+ \frac{J_f \left[M_1 \dot{\overline{\omega}}_{pd}(T_e - T_r) - \dot{u}_r \right]}{M_2 x_{mf}(T_e - T_\infty)} \eta_f \tag{D.6}$$

where the first time derivative of the expressions in equation (3.18) were utilized. The control input, $\overline{\omega}_{pd}(t)$, and control law, $u_r(t)$, are defined in equation (3.18) and Table 3.1, respectively.

The control input derivative is defined as $\dot{\overline{\omega}}_{pd} \triangleq \frac{x_{mp}}{2 J_p \eta_p} \left[\text{sgn}(u_e) - 1 \right] F_p$. The derivative, $\dot{u}_r(t)$, is computed based on the control conditions in Table 3.1. From

equation (D.3), $C_r \dot{T}_{vr}(t)\eta_r(t)$ and $\dfrac{J_p}{x_{mp}}\dot{\omega}_{pd}(t)\eta_p(t)$ change with respect to the sign of the

control law $u_e(t)$, defined in Table 1. Further $\dfrac{J_f}{x_{mf}}\dot{\omega}_{fd}(t)\eta_f(t)$ changes with respect to

the sign of the signal $F(t)$ introduced in equation (3.18). Consequently, four cases may

be realized as shown in Table D.1.

Case	Condition	Description		
I	$u_e > 0, F \leq 0$	$C_r \dot{T}_{vr}(t)\eta_r(t) \neq 0,$	$\dfrac{J_p}{x_{mp}}\dot{\omega}_{pd}(t)\eta_p(t) = 0,$	$\dfrac{J_f}{x_{mf}}\dot{\omega}_{fd}(t)\eta_f(t) = 0$
II	$u_e \leq 0, F \leq 0$	$C_r \dot{T}_{vr}(t)\eta_r(t) = 0,$	$\dfrac{J_p}{x_{mp}}\dot{\omega}_{pd}(t)\eta_p(t) \neq 0,$	$\dfrac{J_f}{x_{mf}}\dot{\omega}_{fd}(t)\eta_f(t) = 0$
III	$u_e > 0, F > 0$	$C_r \dot{T}_{vr}(t)\eta_r(t) \neq 0,$	$\dfrac{J_p}{x_{mp}}\dot{\omega}_{pd}(t)\eta_p(t) = 0,$	$\dfrac{J_f}{x_{mf}}\dot{\omega}_{fd}(t)\eta_f(t) \neq 0$
IV	$u_e \leq 0, F > 0$	$C_r \dot{T}_{vr}(t)\eta_r(t) = 0,$	$\dfrac{J_p}{x_{mp}}\dot{\omega}_{pd}(t)\eta_p(t) \neq 0,$	$\dfrac{J_f}{x_{mf}}\dot{\omega}_{fd}(t)\eta_f(t) \neq 0$

Table D.1 Four cases realized in the Lyapunov stability analysis

In Case I, the $\dot{V}(t)$ expression, introduced in equation (D.2), can be rewritten as

$$\begin{aligned}
\dot{V} &= \eta_e N_e + \eta_r N_1 + \eta_p N_p + \eta_f N_f - \eta_e u_e + \eta_r u_r + \eta_p u_p + \eta_f u_f - M\eta_e\eta_r \\
&\quad - M_1(T_e - T_r)\eta_e\eta_p - M_1(T_e - T_r)\eta_r\eta_p + M_2(T_e - T_\infty)\eta_r\eta_f - C_r\dot{T}_{vr}\eta_r
\end{aligned} \tag{D.7}$$

where $N_1 \triangleq \dfrac{-k_e C_r}{M}\left[\dot{T}_{ed} - \dfrac{Q_{in}}{C_e} + \dfrac{M}{C_e}(T_e - T_{vro}) \right] + N_r$. The variable $N_r(\bullet)$ is defined in

equation (3.23). Utilizing the boundedness inequality for $N_r(\bullet)$ and Assumptions 3.1,

3.5, and 3.7, $N_1(\bullet)$ can be upper bounded as $N_1 \leq \varepsilon_1$ where ε_1 is a real positive constant.

Application of the previous bounding inequality, bounding inequalities in equation

(3.24), and Table 3.1, allows $\dot{V}(t)$ expression in equation (D.7) to be upper bounded as

$$\dot{V} \leq -\gamma \|z\|^2 + \varepsilon_{ee}|\eta_e| - k_{e2}|\eta_e|^2 + \varepsilon_2|\eta_r| - k_{r2}|\eta_r|^2 + \varepsilon_{pp}|\eta_p| - k_{p2}|\eta_p|^2 + \varepsilon_{ff}|\eta_f|$$
$$- k_{f2}|\eta_f|^2$$
. (D.8)

In this expression, $z(t)$ was utilized, as well as $\gamma \triangleq \min\{k_{e1}, k_{r1}, k_{p1}, k_{f1}\}$, $k_e \triangleq k_{e1} + k_{e2}$,

$k_r \triangleq k_{r1} + k_{r2}$, $k_p \triangleq k_{p1} + k_{p2}$, and $k_f \triangleq k_{f1} + k_{f2}$. By completing the squares for the last

eight terms on the right–hand side of equation (D.8), the following inequality can be

obtained (Qu, 1998)

$$\dot{V} \leq -\gamma \|z\|^2 + \varepsilon_a \qquad (D.9)$$

where $\varepsilon_a \triangleq \dfrac{\varepsilon_{ee}^2}{4k_{e2}} + \dfrac{\varepsilon_1^2}{4k_{r2}} + \dfrac{\varepsilon_{pp}^2}{4k_{p2}} + \dfrac{\varepsilon_{ff}^2}{4k_{f2}}$. From equations (D.1, D.9) and inequality

$\lambda_1 \|z(t)\|^2 \leq V(z,t) \leq \lambda_2 \|z(t)\|^2$, it is clear that $V(z,t) \in L_\infty$; hence, $\eta_e(t)$, $\eta_r(t)$, $\eta_p(t)$,

$\eta_f(t)$, $z(t) \in L_\infty$ and then $u_e(t), u_r(t), u_p(t), u_f(t) \in L_\infty$ from Table 3.1 based on

Assumptions 3.2 and 3.3. Since $u_e(t), u_r(t), u_p(t), u_f(t) \in L_\infty$, thus, $\omega_{pd}(t)$, $T_{vr}(t)$,

$\omega_{fd}(t)$, $X_p(t)$, $X_f(t) \in L_\infty$ can be realized using equations (3.19) and (3.20) in Remark

3.2 and the relations $T_{vr} = T_{vro} + \overline{T}_{vr}$ and $\omega_{pd} \triangleq \overline{\omega}_{pd} + \omega_{po}$. From the previous bounding

statements, it is clear that $T_e(t), T_r(t), \omega_p(t), \omega_f(t), \dot{m}_c(t), \dot{m}_a(t) \in L_\infty$. In cases II, III, and

IV, similar stability analysis can be performed to conclude a similar inequality to the

inequality in equation (D.9). For the second case, the expression of $\dot{V}(t)$, introduced in

equation D.2), can be rewritten as

$$\dot{V} = \eta_e N_e + \eta_r N_r + \eta_p N_2 + \eta_f N_f - \eta_e u_e + \eta_r u_r + \eta_p u_p + \eta_f u_f - M\eta_e\eta_r$$
$$- M_1\left(T_e - T_r\right)\eta_e\eta_p - M_1\left(T_e - T_r\right)\eta_r\eta_p + M_2\left(T_e - T_\infty\right)\eta_r\eta_f + \frac{J_p}{x_{mp}}\dot{\omega}_{pd}\eta_p \quad \text{(D.10)}$$

Where for the third case, it may be written as

$$\dot{V} = \eta_e N_e + \eta_r N_3 + \eta_p N_p + \eta_f N_4 - \eta_e u_e + \eta_r u_r + \eta_p u_p + \eta_f u_f - M\eta_e\eta_r$$
$$- M_1\left(T_e - T_r\right)\eta_e\eta_p - M_1\left(T_e - T_r\right)\eta_r\eta_p + M_2\left(T_e - T_\infty\right)\eta_r\eta_f - C_r\dot{T}_{vr}\eta_r \quad \text{(D.11)}$$
$$+ \frac{J_f}{x_{mf}}\dot{\omega}_{fd}\eta_f .$$

The $\dot{V}(t)$ expression, introduced in equation (D.2), can be rewritten for the fourth case as

$$\dot{V} = \eta_e N_e + \eta_r N_r + \eta_p N_5 + \eta_f N_6 - \eta_e u_e + \eta_r u_r + \eta_p u_p + \eta_f u_f - M\eta_e\eta_r$$
$$- M_1\left(T_e - T_r\right)\eta_e\eta_p - M_1\left(T_e - T_r\right)\eta_r\eta_p + M_2\left(T_e - T_\infty\right)\eta_r\eta_f + \frac{J_p}{x_{mp}}\dot{\omega}_{pd}\eta_p \quad \text{(D.12)}$$
$$+ \frac{J_f}{x_{mf}}\dot{\omega}_{fd}\eta_f$$

where $\quad N_2 \triangleq N_{21} + N_{22}, \quad N_{21} \triangleq \left(\dfrac{J_p k_e Q_{in}}{M_1 C_r x_{mp}\left(T_e - T_r\right)^2}\right)\eta_e, \quad N_{22} \triangleq \dfrac{J_p k_e}{M_1 x_{mp}\left(T_e - T_r\right)}\left[-\dot{T}_{ed}\right.$

$$\left. - \frac{Q_{in}\left(T_r - T_{ed}\right)}{C_e\left(T_e - T_r\right)} + \frac{M\left(T_r - T_{ed}\right)\left(T_e - T_{vro}\right)}{C_e\left(T_e - T_r\right)}\right] + N_p, \qquad N_3 \triangleq K_e C_r\left[\frac{Q_{in}}{MC_e} - \frac{\dot{T}_{ed}}{M} - \frac{\left(T_e - T_{vro}\right)}{C_e}\right]$$

$+ N_r, \quad N_4 \triangleq N_{41} + N_{42}, \qquad N_{41} \triangleq \dfrac{J_f k_e C_r\left[M\left(T_e - T_r\right) - Q_o\right]}{C_e C_r x_{mf}} + \dfrac{J_f k_r\left[M\left(T_e - T_r\right) - Q_o\right]}{C_r x_{mf}}$

$$- \frac{J_f k_e k_r \dot{T}_{ed}}{M x_{mf}} + \frac{J_f k_e k_r Q_{in}}{MC_e x_{mf}} - \frac{J_f M_1 \dot{T}_{ed}}{x_{mf}} + \frac{J_f\left[M_1 Q_{in} - \left(MM_1 + k_e k_r\right)\left(T_e - T_{vro}\right)\right]}{C_e x_{mf}} + N_f ,$$

$$N_{42} \triangleq \left(\frac{J_f\left(M^2 C_e - K_e^2 C_r\right)Q_{in}}{M_2 M C_e^2 x_{mf}\left(T_e - T_\infty\right)^2}\right)\eta_e - \left(\frac{J_f\left(k_e C_r + k_r C_e\right)Q_{in}}{M_2 C_e^2 x_{mf}\left(T_e - T_\infty\right)^2}\right)\eta_r , \qquad N_5 \triangleq N_{51} + N_{52},$$

$$N_{51} \triangleq \frac{J_p k_e}{M_1 x_{mp} \left(T_e - T_r\right)} \left[\frac{M\left(T_r - T_{ed}\right)\left(T_e - T_{vro}\right)}{C_e\left(T_e - T_r\right)} - \frac{Q_{in}\left(T_r - T_{ed}\right)}{C_e\left(T_e - T_r\right)} - \dot{T}_{ed} \right] + N_p,$$

$$N_{52} \triangleq \left(\frac{J_p K_e Q_o}{M_1 C_r x_{mp} \left(T_e - T_r\right)^2} \right) \eta_e, \quad N_6 \triangleq N_{61} + N_{62}, \quad N_{61} \triangleq \frac{J_f}{M_2 x_{mf}\left(T_e - T_\infty\right)} \left[\frac{M Q_{in}}{C_e} - \frac{K_r Q_o}{C_r} \right.$$

$$-k_e\left(T_e - T_r\right) \left[M\dot{T}_{ed} + \frac{Q_{in}\left(T_r - T_{ed}\right)}{C_e\left(T_e - T_r\right)} - \frac{M\left(T_r - T_{ed}\right)\left(T_e - T_{vro}\right)}{C_e\left(T_e - T_r\right)} \right] - \frac{M^2\left(T_e - T_{vro}\right)}{C_e} - M\dot{T}_{ed}$$

$$\left. -\frac{k_r M\left(T_e - T_r\right)}{C_r} \right] + N_f, \quad \text{and} \quad N_{62} \triangleq \left(\frac{J_f}{M_2 x_{mf}\left(T_e - T_\infty\right)^2} \left[\frac{M Q_{in}}{C_e} - \frac{K_e Q_{in}\left(T_r - T_\infty\right)}{C_r\left(T_e - T_r\right)} \right] \right) \eta_e$$

$$-\left(\frac{J_f K_r Q_{in}}{M_2 C_e x_{mf}\left(T_e - T_\infty\right)^2} \right) \eta_r .$$ Utilizing the boundedness inequalities for $N_r(\bullet)$, $N_p(\bullet)$, and

$N_f(\bullet)$ in equation (3.23) and Assumptions 3.1–3.3, 3.5, and 3.6, $N_{21}(\bullet)$, $N_{22}(\bullet)$, $N_3(\bullet)$,

$N_{41}(\bullet)$, $N_{42}(\bullet)$, $N_{51}(\bullet)$, $N_{52}(\bullet)$, $N_{61}(\bullet)$, and $N_{62}(\bullet)$ can be upper bounded as

$N_{21} \le \varepsilon_{21}\left|\eta_e\right|$, $\quad N_{22} \le \varepsilon_{22}$, $\quad N_3 \le \varepsilon_3$, $\quad N_{41} \le \varepsilon_{41}$, $\quad N_{42} \le \varepsilon_{42a}\left|\eta_e\right| + \varepsilon_{42b}\left|\eta_r\right|$, $\quad N_{51} \le \varepsilon_{51}$,

$N_{52} \le \varepsilon_{52}\left|\eta_e\right|$, $N_{61} \le \varepsilon_{61}$, and $N_{62} \le \varepsilon_{62a}\left|\eta_e\right| + \varepsilon_{62b}\left|\eta_r\right|$, respectively, where ε_{21}, ε_{22}, ε_3,

ε_{41}, ε_{42a}, ε_{42b}, ε_{51}, ε_{52}, ε_{61}, ε_{62a}, and ε_{62b} are real positive constants. Application of

the previous bounding inequalities, bounding inequalities in equation (3.23), and Table

3.1 allows the expression for $\dot{V}(t)$ to be upper bounded as shown in Table D.2. The

inequalities $\quad \varepsilon_{21}\left|\eta_e\right|\left|\eta_p\right| \le \dfrac{\left|\eta_e\right|^2}{\delta} + \delta\left|\eta_p\right|^2$, $\quad \varepsilon_{42a}\left|\eta_e\right|\left|\eta_f\right| \le \dfrac{\left|\eta_e\right|^2}{\delta_2} + \delta_2\left|\eta_f\right|^2$,

$\varepsilon_{42b}\left|\eta_r\right|\left|\eta_f\right| \le \dfrac{\left|\eta_r\right|^2}{\delta_3} + \delta_3\left|\eta_f\right|^2$, $\quad \varepsilon_{52}\left|\eta_e\right|\left|\eta_p\right| \le \dfrac{\left|\eta_e\right|^2}{\delta_4} + \delta_4\left|\eta_p\right|^2$, $\quad \varepsilon_{62a}\left|\eta_e\right|\left|\eta_f\right| \le \dfrac{\left|\eta_e\right|^2}{\delta_5} + \delta_5\left|\eta_f\right|^2$

and $\varepsilon_{62b}|\eta_r||\eta_f| \leq \dfrac{|\eta_r|^2}{\delta_6} + \delta_6|\eta_f|^2$ were utilized as well as the definitions of k_e, k_r, k_p,

and k_f in Case I to show the results of Table D.2. For Case II, $k_{e1} \geq \dfrac{1}{\delta_1}$ and $k_{p1} \geq \delta_1$. In

Case III, $k_{e1} \geq \dfrac{1}{\delta_2}$, $k_{r1} \geq \dfrac{1}{\delta_3}$, and $k_{f1} \geq \delta_2 + \delta_3$ while in Case IV, $k_{e1} \geq \dfrac{1}{\delta_4} + \dfrac{1}{\delta_5}$, $k_{r1} \geq \dfrac{1}{\delta_6}$,

$K_{p1} \geq \delta_4$, and $k_{f1} \geq \delta_5 + \delta_6$. For all cases, δ_1, δ_2, δ_3, δ_4, δ_5, and δ_6 are real positive

constants. Finally, similar argument as in Case I can be made to show that all signals are

bounded.

Case	Lyapunov Function $V(z,t)$	Definition of γ and ε_a
I	$\dot{V} \leq -\gamma\|z\|^2 + \varepsilon_a,$	$\gamma \triangleq \min\{k_{e1}, k_{r1}, k_{p1}, k_{f1}\},$ $\varepsilon_a \triangleq \dfrac{\varepsilon_{ee}^2}{4k_{e2}} + \dfrac{\varepsilon_1^2}{4k_{r2}} + \dfrac{\varepsilon_{pp}^2}{4k_{p2}} + \dfrac{\varepsilon_{ff}^2}{4k_{f2}}$
II	$\dot{V} \leq -\gamma\|z\|^2 + \varepsilon_b,$	$\gamma \triangleq \min\left\{\left(k_{e1} - \tfrac{1}{\delta_1}\right), k_{r1}, \left(k_{p1} - \delta_1\right), k_{f1}\right\},$ $\varepsilon_b \triangleq \dfrac{\varepsilon_{ee}^2}{4k_{e2}} + \dfrac{\varepsilon_{rr}^2}{4k_{r2}} + \dfrac{\varepsilon_{22}^2}{4k_{p2}} + \dfrac{\varepsilon_{ff}^2}{4k_{f2}}$
III	$\dot{V} \leq -\gamma\|z\|^2 + \varepsilon_c,$	$\gamma \triangleq \min\left\{\left(k_{e1} - \tfrac{1}{\delta_2}\right), \left(k_{r1} - \tfrac{1}{\delta_3}\right), k_{p1}, \left(k_{f1} - \delta_2 - \delta_3\right)\right\},$ $\varepsilon_c \triangleq \dfrac{\varepsilon_{ee}^2}{4k_{e2}} + \dfrac{\varepsilon_3^2}{4k_{r2}} + \dfrac{\varepsilon_{pp}^2}{4k_{p2}} + \dfrac{\varepsilon_{41}^2}{4K_{f2}}$
IV	$\dot{V} \leq -\gamma\|z\|^2 + \varepsilon_d,$	$\gamma \triangleq \min\left\{\left(k_{e1} - \tfrac{1}{\delta_4} - \tfrac{1}{\delta_5}\right), \left(k_{r1} - \tfrac{1}{\delta_6}\right), \left(k_{p1} - \delta_4\right), \left(k_{f1} - \delta_5 - \delta_6\right)\right\},$ $\varepsilon_d \triangleq \dfrac{\varepsilon_{ee}^2}{4k_{e2}} + \dfrac{\varepsilon_{rr}^2}{4k_{r2}} + \dfrac{\varepsilon_{51}^2}{4k_{p2}} + \dfrac{\varepsilon_{61}^2}{4k_{f2}}$

Table D.2 Four cases for final Lyapunov inequalities

REFERENCES

Allen, D., and Lasecki, M., "Thermal Management Evolution and Controlled Coolant Flow," SAE technical paper No. 2001–01–1732, 2001.

Ap, N., and Tarquis, M., "Innovative Engine Cooling Systems Comparison," SAE technical paper No. 2005–01–1378, 2005.

Brace, C., Burnham–Slipper, H., Wijetunge, R., Vaughan, N., Wright, K., and Blight, D., "Integrated Cooling Systems for Passenger Vehicles," SAE technical paper No. 2001–01–1248, 2001.

Chalgren, Jr, R., and Allen, D., "Light Duty Diesel Advanced Thermal Management," SAE technical paper No. 2005–01–2020, 2005.

Chalgren, Jr, R., and Barron, Jr, L., "Development and Verification of a Heavy Duty 42/14V Electric Powertrain Cooling System," SAE technical paper No. 2003–01–3416, 2003.

Chalgren, Jr, R., and Traczyk, T., "Advanced Secondary Cooling Systems for Light Trucks," SAE technical paper No. 2005–01–1380, 2005.

Chanfreau, M., Joseph, A., Butler, D., and Swiatek, R., "Advanced Engine Cooling Thermal Management System on a Dual Voltage 42V–14V Minivan," SAE technical paper No. 2001–01–1742, 2001.

Chen, J., Dixon, W., Wagner, J., and Dawson, D., "Exponential Tracking Control of a Hydraulic Proportional Directional Valve and Cylinder via Integrator Backstepping," *Proceedings of the ASME International Mechanical Engineering Congress and Exposition*, IMECE2002–32076, New Orleans, Louisiana, November 2002.

Chiang, M., Lee, L., Huang, K., "Development of a Hydraulic–Piezoelectric–Actuator for Hybrid Positioning Control with Large Stroke, High Loading and Sub–Micrometer Accuracy," *Proceedings of the IEEE International Conference on Mechatronics*, pp. 45–49, Taipei, Taiwan, July 2005.

Cho, H., Jung, D., Filipi, Z., and Assanis, D., "Application of Controllable Electric Coolant Pump for Fuel Economy and Cooling Performance Improvement," proceedings of the ASME IMECE, Advanced Energy Systems Division, vol. 44, pp. 43–50, Anaheim, CA, November 2004.

Choukroun, A., and Chanfreau, M., "Automatic Control of Electric Actuators for an Optimized Engine Cooling Thermal Management," SAE technical paper No. 2001–01–1758, 2001.

Cipollone, R., and Villante, C., "Vehicle Thermal Management: A Model–Based Approach," proceedings of the ASME Internal Combustion Engine Division, pp. 85–95, Long Beach, CA, October 2004.

Dawson, D., Hu, J., and Burg, T., "Nonlinear Control of Electric Machinery," Marcel Dekker: New York, 1998.

Dostal, G., "Hydraulic Power and Cooling Capacity Available from Agricultural Tractors for Operating Hydraulic Motors," *MS Thesis*, Department of Mechanical Engineering, Iowa State University, 1994.

Eberth, J., Wagner, J., Afshar, B., and Foster, R., "Modeling and Validation of Automotive "Smart" Thermal Management System Architecture," SAE technical paper No. 2004–01–0048, 2004.

Frick, P., Bassily, H., Watson, H., Wagner, J., "A Hydraulic Fan Driven Heat Exchanger for Automotive Cooling Systems," *Proceedings of ASME International Mechanical Engineering Congress and Exposition*, IMECE2006–13464, Chicago, Illinois, November 2006.

Geels, P., Gessier, B., Chanfreau, M., and Tarquis, M., "Advance Control Strategy for Modern Engine Cooling Thermal Systems, and Effect on CO_2 and Pollutant Reduction," proceedings of Vehicle Thermal Management Systems, VTMS 6, pp. 631–641, Brighton, United Kingdom, May 2003.

Hamamoto, T., Omura, S., Ishikawa, N., and Sugiyama, T., "Development of the Electronically Controlled Hydraulic Cooling Fan System," SAE technical paper No. 901710, 1990.

Henry, R., Koo, J., and Richter, C., "Model Development, Simulation and Validation, of Power Train Cooling System for a Truck Application," SAE paper No. 2001–01–1731, 2001.

Incropera, F., DeWitt, D., and Bergman, T., "Fundamentals of Heat and Mass Transfer," John Wiley & Sons Inc: New York, 2002.

Kaddissi, C., Kenné, J.–P., and Saad, M., "Identification and Real–Time Control of an Electrohydraulic Servo System Based on Nonlinear Backstepping," *IEEE/ASME Transactions on Mechatronics*, vol. 12, no. 1, pp. 12–22, February 2007.

Melzer, F., Hesse, U., Rocklage, G., and Schmitt, M., "Thermomanagement," SAE technical paper No. 1999–01–0238, 1999.

Merritt, H., "Hydraulic Control Systems," Wiley & Sons: New York, 1967.

Mitchell, T., Salah, M., Wagner, J., and Dawson, D., "Automotive Thermostat Valve Configurations for Enhanced Performance – Control and Testing," Clemson University Control and Robotics Technical Report, CU/CRB/2/15/07/#1, http://www.ces.clemson.edu/ece/crb/publictn/tr.htm, February 2007.

Page, R., Hnatczuk, W., and Kozierowski, J., "Thermal Management for the 21st Century – Improved Thermal Control & Fuel Economy in an Army Medium Tactical Vehicle," SAE paper No. 2005–01–2068, 2005.

Qu, Z., "Robust Control of Nonlinear Uncertain Systems," John Wiley & Sons: New York, 1998.

Redfield, J., Surampudi, B., Ray, G., Montemayor, A., Mckee, H., Edwards, T., and Lasecki, M., "Accessory Electrification in Class 8 Tractors," SAE paper No. 2006–01–0215, 2006.

Salah, M., Wagner, J., and Dawson, D., "Adaptive and Robust Tracking Control for Thermal Management Systems," Clemson University CRB Technical Report, CU/CRB/10/2/06/#1, http://www.ces.clemson.edu/ece/crb/publictn/tr.htm, October 2006.

Salah, M., Mitchell, T., Wagner, J., and Dawson, D., "Nonlinear Control Strategy for Advanced Vehicle Thermal Management Systems," *IEEE Transactions on Vehicular Technology*, to appear, March 2008.

Setlur, P., Wagner, J., Dawson, D., and Marotta, E., "An Advanced Engine Thermal Management System: Nonlinear Control and Test", *IEEE/ASME Transactions on Mechatronics*, vol. 10, no. 2, pp. 210–220, April 2005.

Taitt, D., Garner, C., Swain, E., Blundell, D., Pearson, R., and Turner, J., "An Automotive Engine Charge–Air Intake Conditioner System: Analysis of Fuel Economy Benefits in a Gasoline Engine Application," *Proceedings of the Institution of Mechanical Engineers, Part D, Journal of Automobile Engineering,* vol. 220, no. 9, pp. 1293–1307, September 2006.

Vaughan, N., and Gamble, J., "The Modeling and Simulation of a Proportional Solenoid Valve," *ASME Journal of Dynamic Systems, Measurement, and Control*, vol. 118, pp. 120–125, March 1996.

Wagner, J., Marotta, E., and Paradis, I., "Thermal Modeling of Engine Components for Temperature Prediction and Fluid Flow Regulation", SAE technical paper No. 2001–01–1014, 2001.

Wagner, J., Ghone, M., Dawson, D., and Marotta, E., "Coolant Flow Control Strategies for Automotive Thermal Management Systems," SAE technical paper No. 2002–01–0713, 2002.

Wagner, J., Srinivasan, V., and Dawson, D., "Smart Thermostat and Coolant Pump Control for Engine Thermal Management Systems," SAE technical paper No. 2003–01–0272, 2003.

Wambsganss, M., "Thermal Management Concepts for Higher–Efficiency Heavy Vehicle," SAE technical paper No. 1999–01–2240, 1999.